MAX-PLANCK-INSTITUT
FÜR POLYMERFORSCHUNG

Nanoparticles for Lubrication

Dissertation

Zur Erlangung des Grades

Doktor rerum naturalium (Dr. rer. nat.)

am Fachbereich Chemie, Pharmazie und Geowissenschaften

der Johannes Gutenberg-Universität Mainz

Fabian Uebel

Geboren in Ludwigshafen am Rhein

Mainz 2021

JOHANNES GUTENBERG
UNIVERSITÄT MAINZ

This thesis was carried out from May 2018 until July 2021 at the Max-Planck-Institute for Polymer Research in Mainz.

Dekan:

Prodekan:

Gutachter 1:

Gutachter 2:

Date of oral examination: 01.09.2021

Declaration

I hereby declare, that I wrote the submitted dissertation without any unauthorized external assistance and used only sources acknowledged in this work. All textual passages which are appropriate verbatim or paraphrased from published and unpublished texts, as well as all information obtained from oral sources, are duly indicated and listed in accordance with bibliographical rules. In carrying out this research, I complied with the rules of standard scientific practice as formulated in the statues of Johannes-Gutenberg-University Mainz to insure standard scientific practice

.....

(Fabian Uebel)

Abstract

Modern lubricant systems are composed of a base oil and various additives. To improve the lubricant performance with regard to friction and wear reduction and also to extend the lubricants lifetime the development of new and more performant additive is needed. Friction is an ubiquitous phenomenon, observed in every machine or between moving surfaces, and is one of the most energy-consuming processes. Almost a quarter of the total worldwide energy produced is wasted trough friction and wear. To reduce energy consumption, the development of new lubrication strategies is essential. In addition to traditional lubricant additives, nanoparticles are now starting to find application in lubricant systems, as they can reduce friction and wear by rolling, sliding or exfoliation mechanisms. Furthermore, hollow nanoparticles enable the encapsulation of lubricant additive molecules inside the nanoparticle. The controlled release of the encapsulated molecules can induce an additional friction modifying effect.

To address these challenges this thesis explores different strategies to improve the design of nanoparticles-based lubricant additives. First, a silica nanocapsule system, able to encapsulate hydrophobic molecules, represents an innovative nanoparticle additive for lubrication. The strategy used here, showed a great synthetic control and allowed to synthesize silica nanocapsules with defined shell thickness and capsule diameter, a detailed study of the mechanical properties was performed by AFM nanoindentation. The breaking force of the shell with respect to its thickness and the nanocapsule diameter was studied. Furthermore, the breaking force was correlated to the mechanoresponsive release of a model molecule under defined external loads. Such nanocapsule-based systems are a perfect solution for the addition of hydrophobic and amphiphilic molecules to the traditional hydrophobic commercial oil base used in the design of lubricant systems.

Alternatively, the delivery of hydrophilic molecules, like glycerol, can be an attractive solution to reduce friction in certain lubricant formulation. To circumvent the poor miscibility of such molecules in the base oil, encapsulation of glycerol into a nanocarrier system which can be dispersed in the lubricant presents a great potential. The nanocarrier system was synthesized from glycerol itself, by performing a crosslinking reaction of nanometer-sized glycerol droplets with isocyanates, forming a polyurethane network around unreacted and therewith encapsulated glycerol. The glycerol nanocarriers could be transferred to a lubricant oil and were tested on their tribological performance

when added to a metal-metal contact. Compared to pure oil, a reduction in friction and wear was observed when the glycerol nanocarriers were added to the lubricant oil.

Finally, sulfur-rich compounds find application in lubricants, as they can minimize wear through welding in extreme pressure contacts, due to the formation of bonds between the sulfur atoms and the metal surface to be lubricated. Polysulfur nanoparticles were synthesized from elemental sulfur by inverse vulcanization polymerization. The obtained sulfur-rich nanoparticles provided high molecular weights and easy processability in form of an aqueous suspension. Thin films of polysulfur nanoparticles were formed and studied on their electrochemical properties as well as their behavior under UV light.

Overall, different strategies were developed to produce lubricant additives based on different nanoparticle systems, ranging from the encapsulation of hydrophobic oils in silica nanocapsules or hydrophilic glycerol in polyurethane nanocarriers to solid polysulfur nanoparticles. These new responsive materials are aiming to reduce friction in tribological contacts and thereby increase the life span of lubricant oils.

Zusammenfassung

Moderne Schmierstoffsysteme setzen sich aus einem Grundöl und verschiedenen Additiven zusammen. Um die Leistung des Schmierstoffs in Bezug auf Reibung- und Verschleißminderung zu verbessern sowie die Lebensdauer des Schmierstoffs zu verlängern, ist die Entwicklung neuer und leistungsfähigerer Additive erforderlich. Reibung ist ein allgegenwärtiges Phänomen, das in jeder Maschine oder jeder bewegten Oberflächen zu beobachten ist und damit zu den energieaufwändigsten Prozessen gehört. Fast ein Viertel der gesamten weltweit produzierten Energie wird durch Reibung und Verschleiß verbraucht. Um den Energieverbrauch zu reduzieren, ist die Entwicklung neuer Schmiermittelstrategien unerlässlich. Neben den traditionellen Schmierstoffadditiven finden nun auch Nanopartikel Anwendung in Schmierstoffsystemen, da sie Reibung und Verschleiß durch Roll-, Gleit- oder Abblätterungsmechanismen reduzieren können. Darüber hinaus ermöglichen hohle Nanopartikel die Verkapselung von Schmierstoffadditivmolekülen im Inneren des Nanopartikels. Die kontrollierte Freisetzung der eingekapselten Moleküle kann einen zusätzlichen reibungsverringernden Effekt erzeugen.

Um diese Herausforderungen zu adressieren, werden in dieser Arbeit verschiedene Strategien zur Verbesserung des Designs von Schmierstoffadditiven auf Nanopartikelbasis untersucht. Zunächst stellt ein Siliziumdioxid-Nanokapselsystem, das in der Lage ist, hydrophobe Moleküle zu verkapseln, ein innovatives Nanopartikel-Additiv für die Schmierung dar. Die hier verwendete Strategie zeigte eine große synthetische Kontrolle und erlaubte die Synthese von Silika-Nanokapseln mit definierter Schalendicke und Kapseldurchmesser. Eine detaillierte Studie der mechanischen Eigenschaften wurde mittels AFM-Nanoindentation durchgeführt. Untersucht wurde die Bruchkraft der Schale in Abhängigkeit von ihrer Dicke und dem Nanokapseldurchmesser. Darüber hinaus wurde die Bruchkraft mit der mechanoresponsiven Freisetzung eines Modellmoleküls unter definierten äußeren Belastungen korreliert. Solche, auf Nanokapseln basierenden Systeme sind eine perfekte Lösung für die Zugabe von hydrophoben und amphiphilen Molekülen zu traditionellen Ölen, die als Basis für das Design von Schmierstoffsystemen verwendet werden.

Alternativ kann die Zugabe von hydrophilen Molekülen, wie z. B. Glycerin, eine attraktive Lösung sein, um die Reibung in bestimmten Schmierstoffformulierungen zu reduzieren. Um die schlechte Mischbarkeit solcher Moleküle im hydrophoben Basisöl zu umgehen, stellt die Verkapselung von

Glycerin in ein Nanocarrier-System, das im Schmierstoff dispergiert werden kann, eine vielversprechende Lösung dar. Das Nanoträgersystem wurde aus Glycerin selbst synthetisiert, indem eine Vernetzungsreaktion von nanometergroßen Glycerintröpfchen mit Isocyanaten durchgeführt wurde. Dadurch wurde ein Polyurethannetzwerk um das nicht umgesetzte und damit eingekapselte Glycerin gebildet. Die Glycerin-Nanocarrier konnten in ein Schmieröl überführt werden und wurden auf ihre tribologische Leistungsfähigkeit bei Zugabe zu einem Metall-Metall-Kontakt getestet. Im Vergleich zu reinem Öl wurde eine Verringerung der Reibung und des Verschleißes beobachtet, wenn die Glycerin-Nanocarrier dem Schmieröl zugesetzt wurden.

Zudem finden auch schwefelreiche Verbindungen Anwendung in Schmierstoffen, da sie aufgrund der Bildung von Bindungen zwischen den Schwefelatomen und der zu schmierenden Metalloberfläche den Verschleiß durch Verschweißen in Kontakten von extrem hohem Druck minimieren können. Polyschwefel-Nanopartikel wurden aus elementarem Schwefel durch inverse Vulkanisations-polymerisation synthetisiert. Die erhaltenen schwefelreichen Nanopartikel wiesen hohe Molekulargewichte auf und erlaubten eine einfache Verarbeitbarkeit in Form einer wässrigen Suspension. Dünne Filme aus Polyschwefel-Nanopartikeln wurden gebildet und auf ihre elektrochemischen Eigenschaften sowie ihr Verhalten unter UV-Licht untersucht.

Insgesamt wurden verschiedene Strategien zur Herstellung von Schmierstoffadditiven auf Basis unterschiedlicher Nanopartikelsysteme entwickelt, die von der Verkapselung hydrophober Öle in Siliziumdioxid-Nanokapseln oder hydrophilen Glycerins in Polyurethan-Nanocarriern bis hin zu festen Poly(schwefel)-Nanopartikeln reichen. Diese neuen responsiven Materialien sollen die Reibung in tribologischen Kontakten reduzieren und damit die Lebensdauer von Schmierölen erhöhen.

Table of contents

1 Introduction

In a highly industrial and globalized world, the worldwide numbers of imported and exported goods increased dramatically over the last decades. These supply chains, but also the transportation of people around the globe involves machines and mechanical systems which all have moving parts and therefore interacting surfaces. Tribology is the study of the interaction between surfaces in movement, and data shows that 23% of the world`s energy consumption originates from those tribological contacts. This is not too surprising when taking into account the number of machines and devices operating every day to keep the globalized world running.[1] One of the main energy consumers is transportation, that is trucks, buses, marine, aviation but also light duty vehicles as passenger cars or vans.[2] All those means of transportation together are consuming vast amounts of energy, which is mainly due to friction in tribological contacts.

Consequently, a straight-forward way to reduce global energy consumption would be to reduce the amount of energy wasted in the tribological contact as friction and wear. The addition of a lubricant oil to surfaces in direct contact is a common strategy to lower friction, as lubricants can minimize direct contact between surface asperities by forming a thin lubricating film. Modern lubricant systems are not only composed of a base oil, but also of additives, all with the purpose to improve the overall performance of the lubricant. Additives like antioxidant, antiwear or anticorrosion agents extend the general lifetime of the lubricant, while the addition of friction modifiers can lower the friction in the contact.[3] To address the energy consumption problem, researchers all over the world have been investigating new materials and strategies to improve the performance of lubricant systems in order to save energy.

Over the last years, nanoparticles and nanomaterials have started to play more important roles in the field of tribology, as they show great potential as friction reducing lubricant additives.[4] Their characteristic nanoscale size allows nanoparticles to enter the tribological contact while at the same time being often considered thermally stable at elevated temperature. Typical nanoparticle additives are composed of metals and metal oxides,[5] but also silica,[6] graphene[7] and sulfides.[8] The friction reducing properties of nanoparticles can be divided in rolling, sliding and exfoliation mechanisms depending on the particle morphology and the contact pressure. Therefore, understanding the mechanical properties of nanoparticle additives is of central importance, to ensure the most

beneficial application of the additive. Detailed investigations of the mechanical properties can be performed by various techniques and approaches. One powerful tool to study the mechanical properties nanoparticles, is atomic force microscopy (AFM) which can be used to perform nanoindentation experiments on individual nanoparticles to determine mechanical parameters as Young's modulus or hardness.[9] [10]

Another advantage of nanoparticle additives is the ability to introduce new chemistries to the lubricant oil, which would not be possible otherwise by direct mixing. This can be achieved through the material of the nanoparticle itself, as for example with inorganic nanoparticles like WS_2 dispersed in a lubricant oil.[11] However, solid nanoparticles only influence the lubrication because of their intrinsic properties or the functionalities of molecules present on the particle surface, whereas nanocapsules have the possibility to encapsulate additional molecules as a core material protected by a solid shell. Therefore, innovative nanocapsule systems allow for the combination of all beneficial effects of nanoparticle additives with the additional possibility to encapsulate and deliver a cargo inside the lubricant oil. As a result, nanocapsule additives enable the delivery of an even wider range of chemistries to lubricants, as for example liquids which are not miscible with the oil can be encapsulated in nanocapsules to eventually be released.

The development of nanocarrier additive systems able to deliver new chemistries to lubricant oils is presented in this thesis. With that goal in mind, three different nanoparticle additives were developed, all based on different chemical compositions and architecture and expected behavior.

The encapsulation of hydrophobic molecules like friction modifying lubricant additives can be realized by silica nanocapsules. The robust properties of silica-based nanocapsules allows mimicking the friction reducing properties of solid nanoparticles, which, together with the ability of carrying a cargo, outlines the great potential of silica nanocapsules as lubricant additive. The controlled release of the encapsulated molecules can occur under external forces which induce breaking of the shell, resulting in a so-called mechanoresponsive release. The forces present in a tribological contact can trigger the mechanoresponsive release. When friction in the contact region increases due to e.g. lubricant depletion, the present forces increase, too. This can be used in a self-regulatory system where the increasing forces in the contact, cause by the degradation of the oil, triggers the release of a friction-reducing molecules from the silica nanocapsules, which could lead to restoring the low-friction

properties of the original oil. Great synthetic control over the shell thickness and diameter of silica nanocapsules, allows one to design tailor-made nanocapsules which break under defined external loads.

Most lubricants are made of hydrophobic and viscous oils, making the addition of hydrophilic molecules extremely challenging due to the limited miscibility. To overcome this problem, the encapsulation of hydrophilic molecules in a nanocarrier which can be dispersed in the oil while carrying the hydrophilic component presents a promising approach. Glycerol, which is known to reduce friction significantly when applied as sole lubricant between metal surfaces,[12] [13] cannot simply be added to lubricant oil due to poor miscibility. The development of a nanocarrier system, able to not only encapsulate glycerol but also be colloidally stable in hydrophobic oils, enables delivery of hydrophilic glycerol to a hydrophobic lubricant oil. The release of the encapsulated cargo can again be triggered by external forces in the tribological contact, resulting in a mechanoresponsive nanocarrier system.

Another approach to control and to reduce friction and wear in tribological contacts is the addition of sulfur and sulfur components. Such components are added in form of oil-soluble sulfur-carriers, which are limited in sulfur content as they are composed sulfurized hydrocarbons. To enable the delivery of higher sulfur concentrations to the tribological contact, the development of sulfur nanoparticles with a high sulfur content represents a promising strategy. Again, the beneficial properties of nanoparticles in reducing friction by rolling, sliding and exfoliation mechanisms, can be combined with the ability of delivering new chemistries to tribological contacts. Furthermore, sulfur is an abundant material and the byproduct of industrial processes,[14] millions of tons of excess are being produced every year, piling up in impressive above-ground sulfur depots.[15] Therefore, finding suitable applications for sulfur as for example in a nanoparticle additive for lubricant oils is crucial.

2 Theoretical background

2.1 Nanocapsules

Nanoparticles with a solid polymer shell and a liquid core material are called nanocapsules. The design and development of functional nanocapsules with controlled chemical compositions and physical properties has been the focus of academic and industrial research in recent years.[16] Already, various fields of applications such as coatings, paints, adhesives, pharmaceutics, biomedicine, or cosmetics take advantage of the exciting properties that nanocapsules bring along. One of the main purposes of nanocapsules is to encapsulate a cargo of interest in order to release it at a later point in time and under controlled conditions. Many different triggers can be used to initiate release, making the nanocarriers thermo-,[17] [18] light-,[19] pH-,[20]enzyme-,[21] or redox-responsive.[22] Most of those existing strategies used for the release of payloads from nanocarriers have been developed for biomedical applications, but they are now used in other fields.

One trigger for the release that has a broad appeal in a variety of fields is the release following the mechanical deformation by the application of controlled mechanical stress on the nanocarriers. Such mechanoresponsive systems are used to influence drug delivery inside the human body, as mechanical forces in the body can either occur physiologically (cellular forces, cardiovascular, musculoskeletal) or by external devices.[23] The mechanical properties of the carrier can further influence the circulation time within the bloodstream, as for example softer hydrogel microparticles show longer circulation times due to their ability to deform through narrow vessels and evade immune system phagocytosis more effectively than stiffer microparticles.[24] More interestingly, those smart mechanoresponsive materials are now gaining interest in a broader range of fields, i.e., damage sensors,[25] self-healing materials,[26] stretchable electronics,[27] or lubrication.

The fabrication of responsive nanocapsules can be achieved by the versatile approach of miniemulsion polymerization. The miniemulsion process allows for the encapsulation of solid or liquid, inorganic or organic, and hydrophobic or hydrophilic payloads into structured polymer nanocarriers.[28] It enables the facile introduction of functionalities to obtain responsive nanocarriers, which release the encapsulated cargo upon a defined external stimulus.

2.1.1 Polymerization in dispersed system

Polymerizations, and especially radical polymerizations, can be carried out in a variety of reaction media. The simplest approach is bulk polymerization, where most often the monomer is liquid and the polymer is solid; the polymerization is conducted in the absence of any solvent which makes removal of heat generated during the reaction challenging. Also the purification of the product (polymer) from the reactants is difficult in bulk polymerizations.[29] Solution polymerizations, in comparison, provide reduced viscosity by introducing a solvent to the reaction. Because of the utilization of organic solvents, potential health and environmental issues have to be taken into account. However, solution polymerization can be found in a number of industrial processes like the polymerization of vinylic monomers.

In polymerizations in dispersed media, the liquid monomer is dispersed in a second liquid, usually water, which is acting as a continuous phase. The removal of heat generated during polymerization is generally not a problem due to low viscosities of the continuous phase, as low viscosities allow better mixing and therefore enhance heat exchange. Additionally, polymerization carried out in this type of heterogeneous media is a perfect way to produce polymer nano- and micro- particles. There are different types of polymerization in dispersed systems such as suspension, dispersion, emulsion, microemulsion and miniemulsion polymerization that are distinguished by the initial state of the system, the mechanism of particle formation or the method used to disperse the two phases, the mechanisms and kinetics of polymerization, the presence of additives, and the size of the resulting particles.[30]

2.1.2 Miniemulsion

Miniemulsion polymerization was first documented by Ugelstad *et al.* in the 1970s,[31] and has since became a versatile method for nanoparticle synthesis. Miniemulsions are prepared by using high shear to break up micrometer-sized droplets of a heterophase system into nanodroplets ranging from 50-500 nm. By the addition of a surfactant and a costabilizer (osmotic pressure agent), a stable miniemulsion of monomer nanodroplets dispersed in a continuous phase can be obtained Figure 2.1.1). Subsequent polymerization leads to the formation of nanoparticles. In an ideal miniemulsion polymerization, every monomer droplet becomes a polymer particle.

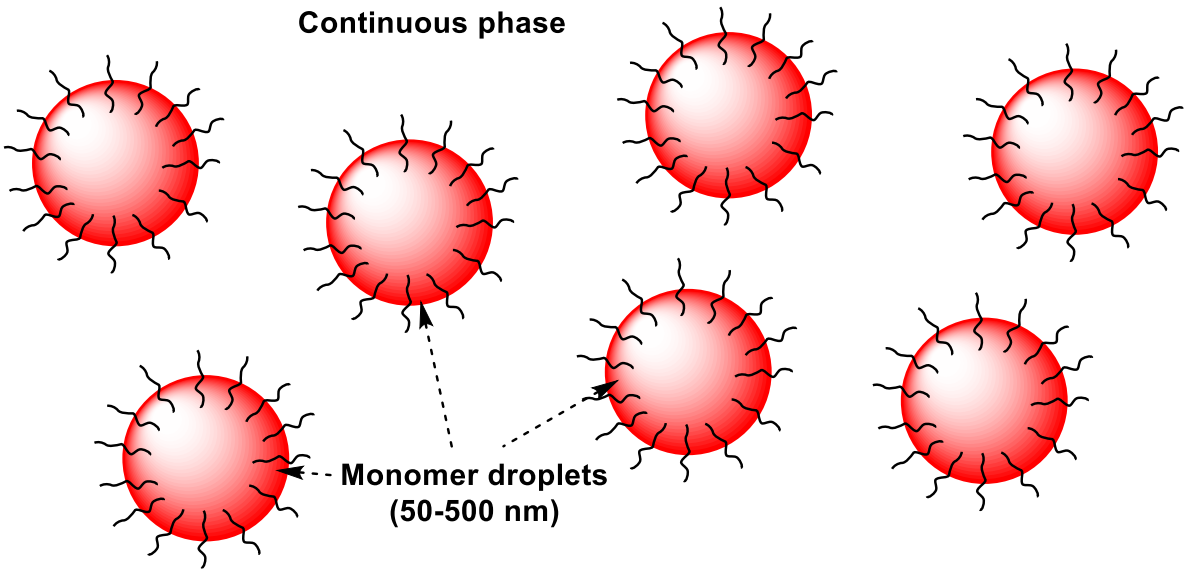

Figure 2.1.1: Scheme of monomer nanodroplets stabilized by a surfactant in a miniemulsion system.

2.1.2.1 Miniemulsion preparation

Typically, miniemulsions are prepared in a two-step process, where first a macroemulsion is prepared by intense stirring, which is then converted to a miniemulsion by further reducing the droplet size. The disruption of macroscopic droplets can be achieved by high shear devices, making these devices essential to obtain a miniemulsion system. [32]

The most commonly used high shear device for laboratory applications is ultrasonication, allowing the preparation of droplets down to 50 nm, depending on the applied surfactant and the surfactant concentration. This device is based on the principle of cavitation caused by high energy shock waves propagating through the heterophase system. Cavitation, where minute bubbles implode to grind the surrounding medium, generates not only high shear forces to disrupt larger droplets but also leads to the formation of local hotspots which can reach temperatures up to 5000 K. Ultrasonication can be performed continuously or in a pulse/pause program and is typically performed until the average droplet size distribution reaches a plateau.

Another common high shear device is the class of high-pressure homogenizers. These devices are converting high fluid pressure into shear forces and cavitation to generate nanodroplets. As a development of high-pressure homogenizers, microfluidization was designed to avoid cavitation. During microfluidization, the pre-emulsified heterophase mixture is passed through small channels inside an interaction chamber at high pressure.[33] For the example of microfluidization, the chambers have commonly a Y- or Z-shape geometries, providing a well-defined microchannel arrangement. This arrangement allows for the collision of fluid streams inside the geometry chamber in order to generate high shear forces and thus the formation of nanodroplets.[34] [35] In a Y-type interaction chamber, the entering fluid stream is divided into two streams which are then recombined in the impact zone by colliding into each other. The high energy impact results in high shear forces disrupting large droplets and consequently a significant decrease in droplet size. Z-type interaction chambers work based on a convoluted microchannel design with several changes in the direction of the flow, leading to droplet disruption through increased shear forces when changing the direction of flow.[34]

2.1.2.2 Stability of miniemulsions

When the continuous phase is made of water while the dispersed phase is made of oil, a direct oil-in-water miniemulsion is obtained. For the dispersion of water in a continuous oil phase, the miniemulsion is described as an inverse water-in-oil miniemulsion. The stabilization of nanodroplets prepared by direct or inverse miniemulsions, is crucial to preserve the miniemulsion system (Figure 2.1.2). Since miniemulsions are only kinetically stable, while thermodynamically metastable, surfactants are added to the continuous phase to prevent coalescence of the droplets caused by the attractive Van der Waals forces (vdW) between adjacent droplets or by the collisions between droplets through Brownian motion. The surfactant lowers the surface tension and therefore reduces the interfacial Gibbs free energy of the droplet to reach a thermodynamically metastable state.

Surfactants stabilize miniemulsions by steric or electrostatic repulsion. In either way, the surfactant forms an adsorbed layer at the interface of the continuous and dispersed phase. Steric repulsion, which can be achieved by the adsorption of, e.g., polymer chains on the nanodroplet surface, is the result of two effects. For one, the saturation of polymers in the region where chains overlap results in an increased local osmotic pressure and thus creating repulsion. The second effect results from the confinement when the polymer chains of two different particles are in close contact, reducing the conformational entropy of the polymer chains as the droplets get closer. This reduced degrees of freedom of the chains, which is thermodynamically not favored, causing the droplets to separate.

Surfactants stabilizing a miniemulsion by electrostatic repulsion possess a charge, which causes the formation of an oppositely charged ion layer surrounding the surfactant stabilized nanodroplets in the solution. This electrical double layer (EDL) causes electrostatic repulsion, when EDL surrounded nanodroplets approach each other. The combined effects of electrostatic repulsion and attractive vdW forces are described by the DLVO (Derjaguin-Landau-Verwey-Overbeek) theory, which is a great tool to describe and predict the colloidal stability of dispersions.

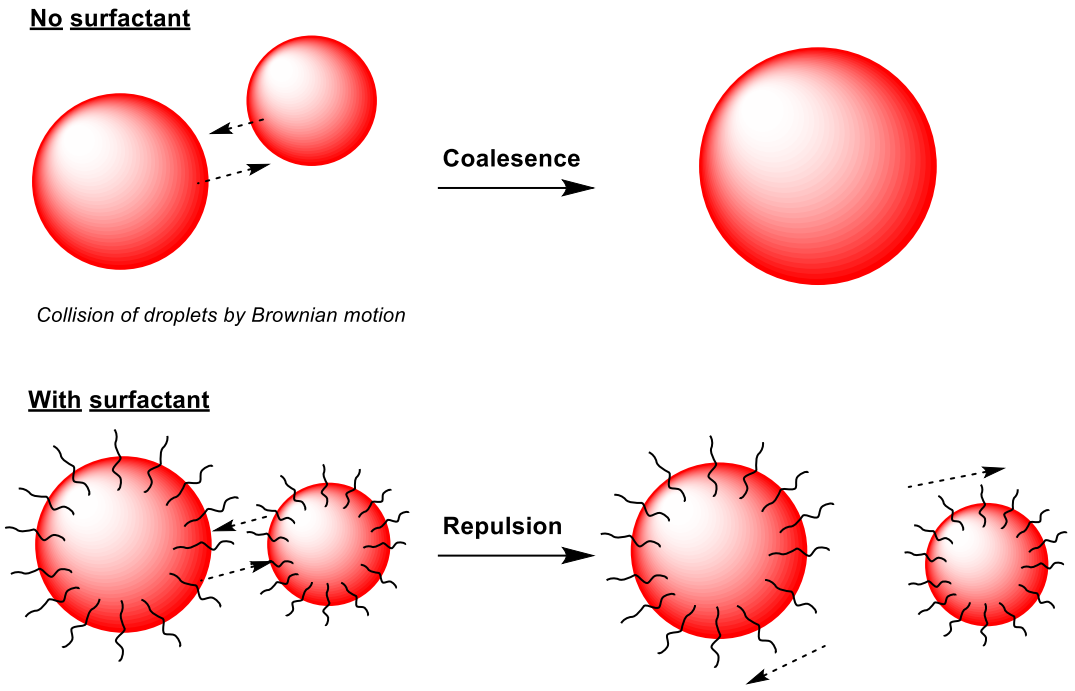

Figure 2.1.2: Schematic display of coalescence processes of droplets without and with surfactant (here for steric stabilization).

Besides coalescence, the effect of Ostwald ripening challenges the stability of miniemulsions. Ostwald ripening is affected by multiple parameters, as droplet size, Laplace pressure, polydispersity and the solubility of the dispersed phase in the continuous phase. Ostwald ripening causes the diffusion of monomer from small droplets of the dispersed phase through the continuous phase to larger dispersed droplets, whereby the volume of larger droplets increases at the cost of smaller droplets (Figure 2.1.3). Ostwald ripening occurs, because small droplets have a higher Laplace pressure than large droplets, which makes the molecular diffusion of monomer from small droplets to large droplets thermodynamically favored. This irrevocably leads to the growth of large droplets and the shrinking of small droplets until the small droplets finally disappear. Ostwald ripening can be limited by the addition of an osmotic pressure agent. If an osmotic pressure agent, which is highly insoluble in the continuous phase but fully soluble in the dispersed phase, is used, it counteracts the Laplace pressure and limits monomer diffusion out of the droplets. The diffusion of monomer from the small droplets to the large ones would increase the concentration of osmotic pressure agent in the small droplets. Therefore, the energy gain due to the reduced Laplace pressure would be counteracted by the increased osmotic pressure. At the equilibrium state, the difference between the Laplace pressure and osmotic pressure reaches a plateau although not being null, which slows down Ostwald ripening

remarkably.[36] A typical osmotic pressure agent for direct (oil-in-water) miniemulsions is hexadecane (HD), while inverse (water-in-oil) miniemulsions are stabilized by water-soluble salts as NaCl, NaOH, Na_2SO_4 or $MgSO_4$.

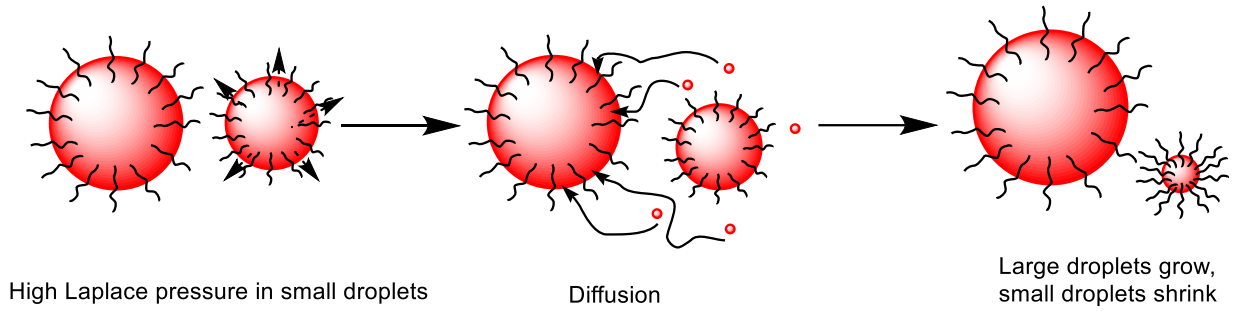

Figure 2.1.3: Schematic display of Ostwald ripening.

2.1.3 Synthesis of nanocapsules via miniemulsion

In comparison to solid nanoparticles, nanocapsules enable the encapsulation of molecules, liquid or solid, and the eventual release of the trapped molecules under controlled conditions. Nanocapsules can be produced from a large variety of natural or synthetic monomers and polymers by utilizing different methods to match the required criteria for various applications.[28] The versatile technique of miniemulsion polymerization, allows for the encapsulation of a wide range of polymers and structured materials into confined geometries.[16]

2.1.3.1 Interfacial polymerization

A versatile method for the formation of nanocapsules is based on interfacial polymerization reactions.[37] The shell formation occurs by the encounter of monomers at the interface of dispersed droplets and continuous phase in a miniemulsion setup. The interfacial polymerization technique has been reported for different polymerization mechanisms as for example polyaddition and polycondensation reactions.

Interfacial polymerization reactions following polyaddition mechanisms can be used to form an array of different polymer shell materials around an solvent core in a miniemulsion,[38] including polyurea, polythiourea or polyurethane. In those later cases, hydrophilic monomers, providing amine, diol or multi-ol functionalities are dissolved in aqueous droplets and undergo polymerization with

diisocyanate monomers present in the continuous organic phase. A typical diisocyanate used for interfacial polymerizations is 2,4-toluene diisocyanate (TDI), which can be used as crosslinker in the formation of polyurethane nanocapsules as well as biocompatible enzyme nanocapsules.[39] The formation of polyurethane nanocapsules by the interfacial polyaddition reaction of a monomer providing hydroxyl groups and the crosslinker TDI is shown in Figure 2.1.4.

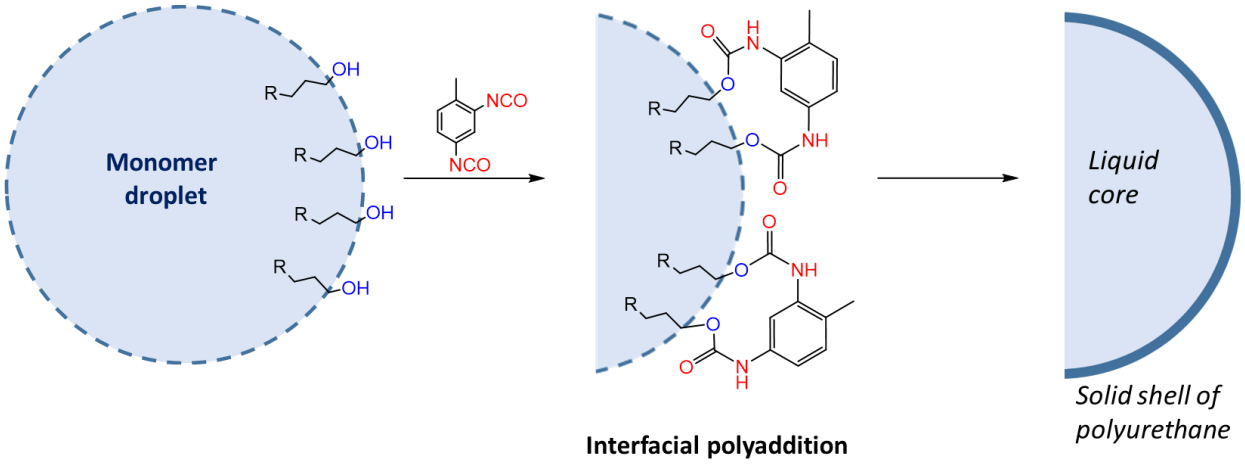

Figure 2.1.4: Nanocarrier formation by interfacial polyaddition of glycerol droplets and 2,4-toluene diisocyanate in a water-in-oil miniemulsion setup.

Polycondensation reactions occurring at interfaces in miniemulsion can be used to form silica nanocapsules, with a solid silica shell surrounding an oil core.[26] [40] [41] To encapsulate molecules in the core, the payload can first be dissolved or dispersed in template liquid droplets, followed by the formation of a surrounding silica shell.[41] The shell is formed by the hydrolysis and subsequent polycondensation of silica precursors, dissolved in the dispersed organic phase in an oil-in-water miniemulsion. Exemplary reaction equations of the sol-gel process are shown in Figure 2.1.5.

$$Si(OR)_4 + x(H_2O) \rightleftharpoons Si(OR)_{4-x}(OH)_x + x(ROH)$$

and the subsequent condensation

$$(RO)_3\text{-}SiOH + HO\text{-}Si\text{-}(OR)_3 \rightleftharpoons (RO)_3\text{-}Si\text{-}O\text{-}Si\text{-}(OR)_3 + H_2O$$

Figure 2.1.5: Reaction equations of the sol-gel process during the formation of silica nanocapsules.

To obtain silica nanocapsules, the silica precursor, commonly a tetraalkoxysilane like tetraethylorthosilicate (TEOS), is dissolved in the dispersed phase together with a hydrophobic liquid

which will form the core of the silica nanocapsule. The continuous aqueous phase consists of water and an ionic surfactant to stabilize the miniemulsion and further to catalyze the interfacial condensation reaction. After emulsification, TEOS moves to the oil-water interface through the interaction with the cationic surfactant to form partially or fully hydrolyzed alkoxysilanes by the reaction with water (sol-process). The following condensation reaction between the formed silanol groups leads to the formation of a solid silica network by eliminating water (gel-process). This interfacial polymerization is schematically shown in Figure 2.1.6.

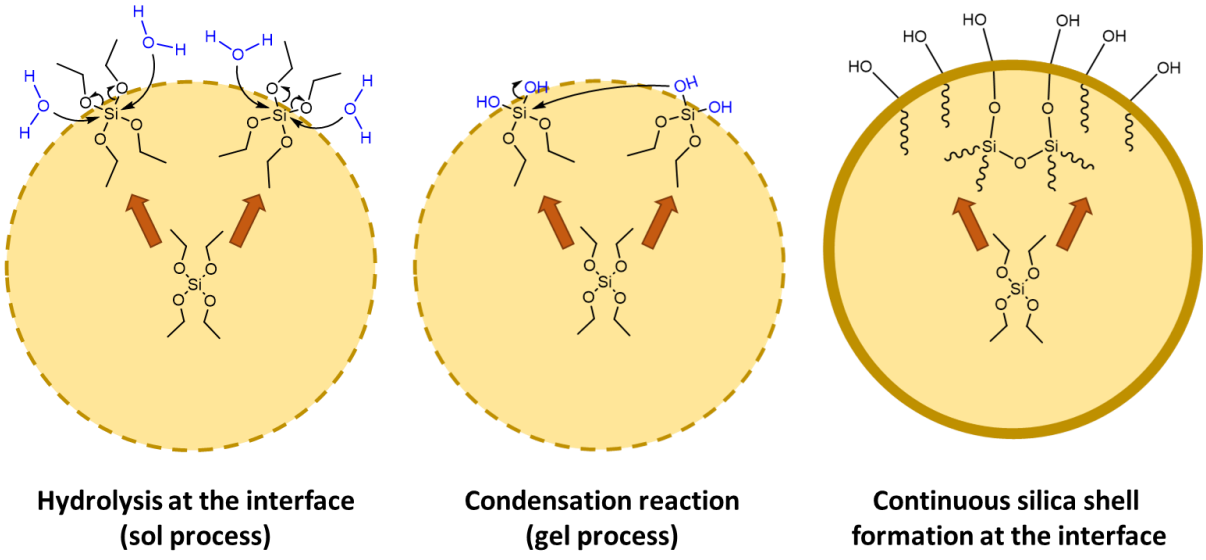

Figure 2.1.6: Formation of silica nanocapsules by sol-gel process of the silica precursor TEOS reacting with water at the oil-water interface.

2.1.3.2 Layer-by-layer technique

The layer-by-layer technique is used for the formation of nanocolloids consisting of polyelectrolytes with well-defined chemical and structural properties.[42] This technique is based on the consecutive adsorption of polyanions and polycations onto a sacrificial core material like polystyrene or silica.[43] [44] The self-assembly based on the irreversible electrostatic attraction of oppositely charged polyelectrolytes results in multiple layers, forming the desired core-shell morphology. Typical polycations used for the formation of nanocapsules by the layer-by-layer technique are polylysine,[45] poly(allylamine)[46] [47] or chitosan.[46] [48] Typical polyanions are poly(styrene sulfonate)[47], poly(acrylic acid)[49] or hyaluronic acid.[50]

2.1.3.3 Phase separation during polymerization

A facile, one-step method to obtain nanocapsules by miniemulsion is based on phase separation of polymer and hydrophobic oil in an oil-in-water miniemulsion system. The monomer, which is initially soluble in the hydrophobic oil, becomes immiscible with the oil throughout the polymerization process and therefore induces a phase separation.[28] The driving force for the formation of nanocapsules originated from the phase separation and the difference in hydrophilicity of the formed polymer and the hydrophobic oil. The core-shell morphology can only be obtained when thermodynamically favored, making a precise tuning of the different interfacial tensions at the interfaces of polymer/water, polymer/oil, and oil/water essential.[51]

2.1.3.4 Phase separation by solvent evaporation

The formation of nanocapsules based on phase separation events can also be realized by solvent evaporation. A preformed polymer is dissolved in a mixture of a good solvent with a low boiling point together with a non-solvent of higher boiling point. This polymer solution in the mixture of solvent is emulsified in a non-miscible solvent forming the continuous phase. After emulsification, the good solvent in the dispersed phase was slowly evaporated, resulting in the precipitation of the polymer at the interface of continuous phase and the remaining non-solvent in the dispersed phase, forming a shell around the core of non-solvent. For example, this approach was used to encapsulate a phototriggerable nitric oxide donor complex in polymer nanoparticles by evaporating hexafluoroisopropanol (HFIP) from a HFIP-in-alkane miniemulsion.[52]

2.1.4 Release from nanocapsules

The release of an encapsulated cargo from a nanocarrier can follow two main mechanisms: Diffusion-induced release and degradation-induced release (Figure 2.1.7). Diffusion-induced release occurs by the diffusion of encapsulated molecules through the pores of the shell material. This process, which is mainly driven by the osmotic pressure differences inside and outside the nanocapsules, is often slow and can be controlled by the size of the pores or the size of the trapped molecules.[53] However, release by diffusion through a porous shell can also be a great challenge to overcome when release is not desired. Such passive release is, especially for the encapsulation of small molecules, very difficult to avoid and can, to a certain extent, be observed for almost every nanocapsule system. Degradation-induced release occurs upon rupture of the nanocapsule shell, leading to the instantaneous release of encapsulated molecules. The shell degradation can occur spontaneously or be induced by external stimuli that compel shell degradation.

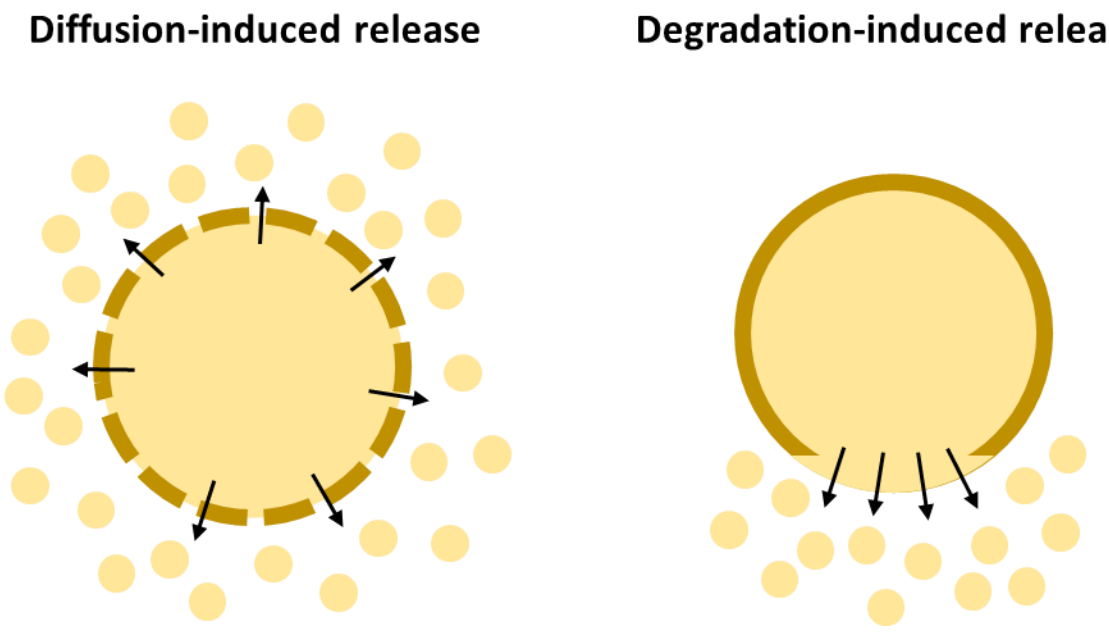

Figure 2.1.7: Release of encapsulated cargo from nanocapsules by diffusion or degradation mechanisms.

2.1.5 Responsive functionalities of nanocapsules

Generally, functionalities can be introduced into nanocapsules by the implementation of monomers with functional groups preservable during the polymerization or by post-modification of polymers existing in the dispersed phase. In any way, miniemulsion represents a versatile method to precisely integrate various functionalities into nanocapsules.[54]

Functionalized nanocarriers allow the introduction of responsiveness to certain external stimuli, which can promote the release of the encapsulated cargo. Such nanocarriers can be thermo-,[17] [18] light- ,[19] pH-,[20] enzyme-[21] or redox-responsive[22], among many other possible stimuli. The compelling advantage of responsive nanocapsules can be found in the great control over release. While non-responsive systems can only release the encapsulated cargo by a passive, diffusion-driven release or the spontaneous degradation of the capsule, stimuli-responsive nanocapsules enable extended control over the point in time when the release occurs.

One of the most studied stimuli is thermoresponsiveness, which is often governed by a sharp nonlinear change in the material properties of at least one of the components forming the nanocapsules. A common polymer for thermoresponsive nanocarriers is poly(N-isopropyl acrylamide) (PNIPAM), which exhibits a temperature-dependent reversible phase transition that changes the polymer conformation in order to promote or limit release. The phase transition results from the reduced solubility of the polymer in an aqueous environment when heated above a lower critical solution temperature (LCST).[55] Another temperature-responsive nanocarrier system based on LCST are micellar nanoparticles based on an amphiphilic poly(γ-2-(2-(2-methoxyethoxy)-ethoxy)ethoxy-ε-caprolactone)-*b*-poly(γ-octyloxy-ε-caprolactone) diblock copolymer, which showed improved biodegradability and low-toxicity compared to PNIPAM nanocarriers.[56]

Other physicochemical cues can be used to trigger the release. While temperature-responsive nanocarriers typically follow a diffusion-induced release, enzyme-responsive nanocarriers made out of the natural polymer lignin undergo degradation-induced release upon contact with lignin-degrading enzymes.[57] The lignin nanocarriers showed a selective enzymatic release when in contact with fungi spores, allowing for the controlled release of encapsulated drugs. Redox-responsive nanocarriers made from polyurea were used to encapsulate hydrophilic materials, followed by the controlled release of the cargo upon reduction. By the implementation of disulfide bonds in the shell

material, the addition of the reducing agent led to S-S cleavage and therefore induced release of the cargo.[58] A dual stimuli-responsive nanocarrier system, made of poly(2-hydroxyethyl methacrylate-*co*-methacrylic acid) and light-cleavable crosslinking points, shows pH-dependent swelling and light-induced degradation.[59] The pH-responsiveness results from the protonation/deprotonation events of the methacrylic acid groups and leads to a measurable change in particle diameter, while the light-responsiveness arises from the implementation of photolabile crosslinking molecules (nitroveratryloxycarbonyl derivatives) into the polymer network, leading to the disintegration of the microgel structure upon light irradiation. The combination of these two stimuli allowed for the efficient loading and subsequent release of model proteins.

One trigger mechanism for the payload release that has a broad appeal in a variety of fields is the release following the mechanical deformation or the application of controlled mechanical stress on the carrier system. The applied external force can promote release by simply breaking the capsule shell, by inducing chemical reactions or by squeezing the material to force release.[60] For example, a mechanochemically sensitive system of hybrid microcapsules made from alternating layers of inorganic colloidal particles and biopolymers by the layer-by-layer technique, is capable of loading drugs and releasing them mechanoresponsively by the application of weak external forces.[61]

2.1.6 Application of responsive nanocapsules

Nanocapsules are able to respond to external influences as light, temperature or pressure, which makes such systems highly interesting for applied fields. Nanoscale drug delivery systems are among the most studied systems for the application of responsive nanocapsules, as studies have revealed the outstanding potential in target-specific delivery of therapeutics and diagnostic agents.[16] [62] Furthermore, nanocapsules can achieve excellent biocompatibility inside the human body, allowing controlled release over an extended duration which is highly beneficial for drugs that are rapidly metabolized.

Also, mechanoresponsive systems are used to influence drug delivery inside the human body. For example, a macroscopic hydrogel composed of β-cyclodextrin loaded with the anti-emetic drug ondansetron, allows mechanoresponsive release when compressing the gel. Due to the applied external force, a variation in the inclusion capability of the β-cyclodextrin is achieved, promoting the release of the encapsulated drug.[63] In another work, stretchable elastomeric microgels with depots

containing drug-loaded nanocapsules showed release under the application of tensile strain.[64] The applicability of these microgels was demonstrated by embedding them in adhesive bandages located on finger joints, showing drug release under the tensile strain generated by bending the finger itself.

Moreover, those smart mechanoresponsive carriers are now gaining interest in a broader range of fields, i.e. self-healing materials,[25] stretchable electronics,[27] or lubrication. Microcapsules are used to sense damaged structures by releasing dye molecules upon mechanical damages, allowing to locate harmed areas. By combining functionalities, nanocarrier systems are even able to release self-healing agents to the damaged area, granting a successful recovery of the original material properties.[25] Additionally, core-shell particles with a liquid metal core and a metal-oxide shell are used in stretchable electronics, which show an increasing volumetric conductivity when strain is applied. [27] The applied strain induces the degradation-induced release of the liquid metal from the core-shell particles resulting in a measurable increase in conductivity.

In the field of tribology, the interest in the possibility of using solid colloidal nanoparticles as friction modifiers and anti-wear agents is growing. So far, nanoparticles made of carbon, silicon, dichalcogenides, polymers and metals were used as additives in order to reduce friction in the lubrication system. [4] [5] [6] Friction modifying additives give the ability to introduce chemistries that are normally insoluble in non-polar base oils to the usually hydrophobic lubricant oils.[65] By encapsulating liquid friction modifiers into nanocapsules with a solid shell, this approach allows for the combination of both advantages, the low friction properties of solid nanoparticles and the opportunity to transport and release a friction modifier additive.

2.2 Mechanical properties of nanoparticles

Nanomaterials, and especially nanoparticles (NPs), are highly interesting materials due to their potential for application in a range of fields such as nanomedicine, nanoelectronics or nanomanufacturing, and to their outstanding versatility in regards to synthesis, functionalization and physico-chemical properties. NPs are, at least in one dimension, smaller than 100 nm, which strongly influences their physico-chemical properties compared to bulk materials of identical composition.[66] In the case of NPs, not only their chemical composition, but also their morphology (size, shape) and surface properties strongly dictate their mechanical behavior. The differences caused by the nanoscale-size are mainly due to the high surface area to volume ratio observed in nanomaterials. [67] The large surface area of NPs magnifies the influence of the interactions between the material and the environment compared to bulk materials. Furthermore, in bulk, the number of surface atoms compared to interior atoms is negligible, while for nanomaterials the surface atom contribution increases with decreasing particle size, outlining the influence of surface atoms on the nanomaterial properties. Additionally, in nanomaterials, like quantum dots, quantum effects influence the final properties. It was found that the effect of size influences structural and electronic properties of silicon quantum dots, as structural distortions are not only influenced by the kind of dopant but also the size of the dots.[68] When the size of a particle approaches the nanoscale, and is close to, or smaller than, the de Broglie wavelength of the charge carrier (electrons and holes) or the wavelength of light, the resultant quantum confinement destroys the periodic boundary conditions of crystalline particles. Furthermore, for amorphous particle the atomic density on the surface is influenced by the size of the NPs. Therefore, a variety of physical properties of nanoparticles like melting point, fluorescence, electrical conductivity, magnetic permeability or chemical reactivity are different from the same material in bulk.

The mechanical properties of nanomaterials also display significant variations in comparison to bulk materials. In macroscopic materials, the deformation is typically controlled by the interaction between the molecules, while for nanoscale objects many other forces, such as van der Waals (vdW), adhesion and electrostatic, also need to be taken into account. Therefore properties like hardness, Young's modulus, yield stress and fracture toughness are affected by the size and can either be reduced or enhanced with the reduction in size.

Understanding and controlling the mechanical properties of materials at the nanoscale is important in the design of new nanomaterials for certain specific applications. For example, solid nanoparticles made of iron, cobalt, copper[5] or WS_2[69] are finding use as additives in lubrication system, helping to reduce the coefficient of friction and improving the overall performance of the lubricant. Additionally, nanoparticles can be used as the abrasive in nanopolishing of ultra-smooth surfaces by chemical mechanical polishing (CMP), demonstrating the outstanding diversity and applicability of NPs.[70] [71] [72] The performance of NPs in lubrication and CMP is closely connected to their mechanical properties, as the Young's modulus or the hardness of NPs directly dictates their behavior as lubricant or abrasive material.

Similarly, hollow nanoparticles, which allow encapsulation of a broad variety of cargo find, application in drug delivery. [16] [62] These nanocarriers enable the delivery of a functional cargo inside the human body, giving the opportunity to locally deliver a drug instead of the distributing it to the entire body as conventional systemic distribution would do. The mechanical properties of the nanocarriers play an important role in their behavior as drug delivery system, as they influence the circulation time of the NPs in the bloodstream. Consequently, the successful application of nanocarriers in drug delivery requires detailed understanding of the material mechanical properties.[24]

Hollow NPs are also used in damage sensing applications, systems able to sense and report when a structure is getting damaged are often based on nanocapsules, which can release dye molecules upon mechanical damages.[25] Such damage sensing capsules help to locate the harmed area very effectively, allowing a quick repairing or replacement of damaged pieces. By controlling the mechanical properties of the nanocapsules, the threshold of force needed to induce the damage sensing can be finely tuned.

The mechanical properties of bulk materials are usually measured by a combination of standardized hardness-, tensile-, fatigue-, fracture toughness- and shear- tests. However, when dealing with nanomaterials, such characterizations become more challenging, requiring new approaches or the adjustment of existing techniques. One of the technique used the most frequently to study the mechanical properties of nanomaterials is atomic force microscopy (AFM).[73] The tip of the AFM can be used as an indentor to compress a sample with a known force and measure the resulting deformation.[74] Furthermore, *in situ* TEM can be performed to observe the deformation of

nanomaterial located between two moving plates in the microscope, allowing a detailed study of deformation nucleation or buckling behavior.[75] Additionally, computer-based approaches like molecular dynamics simulations (MD) or finite element (FE) modeling can be used to predict displacement events within objects under a defined external load.

The mechanical response of macroscopic objects to an applied stress will be a deformation either elastic or plastic, which will be influenced by the mechanisms of stress dissipation present in that material. When the response of the material is elastic, the relationship between the applied force (compression, extension, shear) and the deformation is defined by the Young's modulus *E*:

$$E = \frac{\sigma}{\varepsilon} \tag{2.2.1}$$

where σ is the uniaxial stress and ε the strain or proportional deformation. The deformation is the configurational change of an object caused by the application of a load.

In addition to the elasticity characterized by the Young's modulus, the hardness of materials is also frequently studied. The hardness is defined as the ability of a material to resist deformation, such as localized plastic deformation induced by indentation. For nanoindentation experiments, the hardness *H* is often expressed as:

$$H = \frac{P_{max}}{A(h_c)} \tag{2.2.2}$$

where P_{max} is the maximal indentation load and $A(h_c)$ the contact area at the contact depth h_c.

2.2.1 Forces at nanoscale

At the nanoscale, diverse interaction forces within the nanoparticles, between multiple nanoparticles and between surface and nanoparticles are present. In bulk, these forces usually play a minor role in influencing the mechanical properties of the material, but at the nanoscale the van der Waals forces, capillary forces, electrostatic forces or adhesion become very relevant to explain the behavior of the material.

2.2.1.1 Van der Waals forces

Van der Waals (vdW) forces describe the weak interactions between molecules and can be divided in three different contributions: Keesom, Debye and London forces. Keesom forces arise from the interactions between two molecules each possessing a permanent dipole. Debye forces occur between a permanent dipole and an induced dipole. Finally, London dispersion forces occur between two induced dipoles.

The influence of VdW forces is range-dependent. It decreases with the sixth power of the distance for the interactions between atoms and molecules:

$$U_{vdW} = U_{Keesom} + U_{Debye} + U_{London} = \frac{C_{orient}}{d^6} + \frac{C_{induced}}{d^6} + \frac{C_{disp}}{d^6} = \frac{C_{AB}}{d^6} \quad (2.2.3)$$

where C_{AB} is a constant including all distance-independent term of the individual contributions of two molecules A and B, while d is the distance between the molecules.

When looking at spherical particles much larger than molecules, this range dependence changes as first described by Hamaker.[76] The interaction energy W between two half-spaces of media 1 and 2 separated by the distance d is defined as:

$$W = \frac{-A_{12}}{12\pi d^2} \quad (2.2.4)$$

where A_{12} is the Hamaker constant. At distances much larger than the particle radius, the interaction reverts to inverse-sixth-power dependence. The attractive vdW forces are therefore generally understood as long-range forces.

When thinking of a close-packed nanoparticle assembly, the long range vdW forces play an important role in enhancing material parameters like hardness as the attractive forces between the nanoparticles have to be overcome to separate the assembled nanoparticles. Thereby, smaller

nanoparticles experience higher vdW forces due to shorter distances between the inter-particles junctions as more small particles can be found in the same volume compared to larger particles. The theories of Hamaker were expanded by the Derjaguin approximation, which allows the transfer of vdW forces between objects of any shape to the simple interaction between two planes.[77] When applying the model to colloidal systems, the effect of a medium surrounding the particles must be considered. The Dzyaloshinskii-Lifshitz-Pitaevskii (DLP) theory, based on the quantum electrodynamic field theory, describes the forces between two plates across a dielectric medium.[78] The DLP theory combines the Hamaker theory of dispersive force, Debye forces and Keesom forces in one single equation. With regard to nanoparticles, the presence of solvated ions or other components of the solution has to be reconsidered as the small size difference between nanoparticles solvated ions can strongly influence colloidal stability, as studied for Au and ZnO particles.[79] [80]

Further, vdW forces are utilized in the formation of semiconductor p-n junctions which are essential building blocks for electronic and optoelectronic devices.[81] The mechanical properties of such vdW heterostructured materials are fundamentally different and more flexible than conventional covalently bound materials. This results from the lack of dangling bonds on the surface of these materials, which moreover allows the creation of high-quality interfaces. [82] [82] [82] [82] [82] VdW forces find further practical application in low-friction nanoscale linear bearings made from multiwall carbon nanotubes, where the retraction of telescoping nanotube segments is achieved by attractive vdW forces.[83]

2.2.1.2 Electrostatic force

The electrostatic force, which can be described by Coulomb´s law, is one of the basic forces found in nature:

$$F = \frac{1}{4\pi\varepsilon_0}\frac{qQ}{r^2} = k_e\frac{qQ}{r^2} \tag{2.2.5}$$

where *r* is the distance between two charges, ε_0 the vacuum permittivity, *q* and *Q* the two charges, while Coulombs constant is defined as k_e. At the nanoscale, electrostatic forces become very relevant and directly affect the nanomaterial properties. For example, the electric charge on the surface of NPs can prevent the aggregation of the NPs in a suspension through electrostatic repulsion.

Nanoparticles suspended in liquids with a high dielectric constant like water can show a charged surface, preventing possible coalescence due to the repulsive electrostatic force. The surface charges are balanced by a rigid layer of adsorbed ions with opposite charge (Stern layer) and a diffuse layer of non-bound ions in the solution at some distance away from the surface, forming the electrical double layer (EDL).[84] In the Stern layer, the surface potential decreases linearly with the distance, but changes to an exponential decay in the diffuse layer. The Stern layer itself can further be divided into an inner and outer Helmholtz layer, where the inner layer consists of strongly bound ions due to attractive vdW forces or specific interactions with the surface material, while the outer layer hosts hydrated counter ions.

The effects of vdW forces and electrostatic repulsion are combined in the DLVO (Derjaguin-Landau-Verwey-Overbeek) theory, which is often used to describe the colloidal stability of dispersions. Adsorption or aggregation of nanocolloids in suspension or the forces between interacting charged surfaces through a liquid medium can be explained by the DLVO theory. The net potential for such systems is displayed in Figure 2.2.1, showing the interplay of repulsive forces through the EDL at larger range competing against the attractive vdW forces at shorter range.

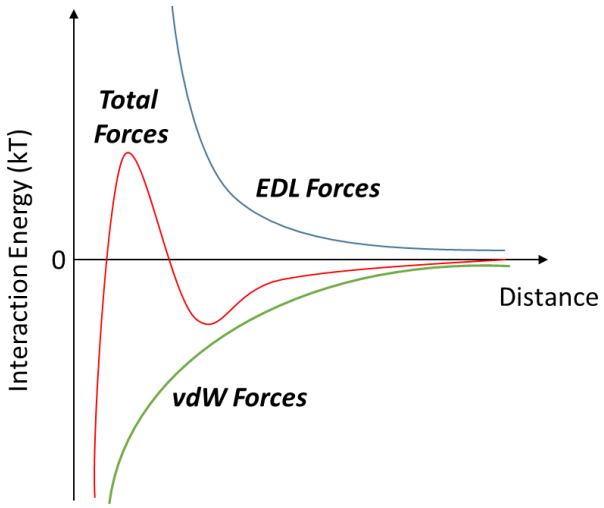

Figure 2.2.1: Combined DLVO interaction energy consisting of vdW and EDL forces.

The presence of charges can also affects the mechanical properties of the material. For example, the addition of ionic groups in polystyrene microspheres increased the Young's modulus of the spheres compared to pure polystyrene microspheres, because the ionic groups form clusters which act as crosslinking points to increase the particle stiffness.[9]

2.2.1.3 Capillary forces

The capillary force refers to the formation of liquid menisci in a gaseous environment. The tendency of liquid droplets to reduce their surface area to a minimum is understood as the result of the surface tension of the liquid occurring at the liquid/gas interface. The capillary force can be classified into two types: normal and lateral capillary force. The normal capillary force is the result of two actions: the pressure difference across the curved interface and the action of the surface tension force exerted around the annulus of the meniscus. The normal capillary force can be attractive or repulsive, depending on the shape of the capillary bridge between the surfaces being convex or concave.[85] The lateral capillary force arises from the overlapping perturbations of the liquid surface due to the presence of particles.[86] The capillary forces increase with larger interfacial deformation caused by the particles.

The presence of liquid menisci around the contact area of neighboring particles can cause strong adhesion which must be taken into account when studying the interactions between particles or particles to surfaces. But more importantly for the mechanical properties of nanomaterials, the surface tension and surface stress induced by the capillary force affect the stability and plasticity of nanomaterials, by enhancing the action of a compressive external load and diminishing that of tensile load, resulting in a substantial tension-compression asymmetry in nanomaterial such as nanowires[87] [88] [89] and nanoporous metals.[90] [91] [92] Capillary forces also influence the mechanical properties of small crystals with characteristic radii at the lower nanoscale. The surface-induced stress affects the shear deformation and plasticity of such crystals. Thus, surface stress is believed to impose a lower limit on the stable size of crystals and further to contribute substantially to nanoscale mechanical behavior.[93]

2.2.1.4 Contact and adhesion theories

The interaction between two bodies in contact with each other and the forces present at the contact has to be differentiated for nanoscale objects and macroscopic objects. The contact of objects is often described by the Hertz theory for contact mechanics. However, this simple theory does not include surface forces as only the displacement and the contact area are described. For larger objects these forces do not necessarily need to be taken into account, but at smaller scales, surface forces play a major role in adhesion, contact and deformation behavior. The model developed by Johnson-Kendall-Roberts (JKR),[94] accounts for adhesion forces and therefore appears more suitable when studying the mechanical properties of contacting nanomaterials. As an example, the Young's modulus determined for polystyrene NPs results in higher values when calculated by the Hertz model compared to the JKR model, because the latter model is taking adhesion and capillary forces into account, outlining the importance of the correct interpretation of present adhesion forces for the precise determination of mechanical properties.[95] Besides, the change in surface energy of deformed nanoparticles has to be considered when studying the mechanical properties of nanomaterials.[96] This can be achieved by the Derjaguin-Muller-Toporov (DMT) theory, which is more suitable for hard bodies with smaller surface energies.[97]

2.2.2 Atomic force microscope to study mechanical properties of nanomaterials

The atomic force microscope (AFM) is a versatile tool typically used to obtain images of nanometer resolution. Figure 2.2.2a shows the general working principle of the AFM. During the AFM experiment, the cantilever equipped with a sharp tip (probe) is scanned across on area of the surface of a sample. The tip of the cantilever is deflected by asperities on the surface and any relief on the surface. The deflection of the cantilever is recorded by pointing a laser on the cantilever reflective backside and collecting the reflected laser light with position-sensitive photodetector. The deflection of the laser is then translated into a topographical image of the sample´s surface area.

The AFM can operate in different modes, with three main modes being contact, tapping or non-contact mode. In the simplest operating mode, the contact mode, the cantilever tip is in direct contact with the sample surface when scanning it. Contact mode is commonly configured by a constant force or a deflection feedback mode, making the cantilever deflection the feedback parameter. Contact mode is easy to operate and allows fast scanning of samples with a high precision. However, fast wear of the tip and damaging of the surface has to be taken into account when performing AFM measurements in contact mode.

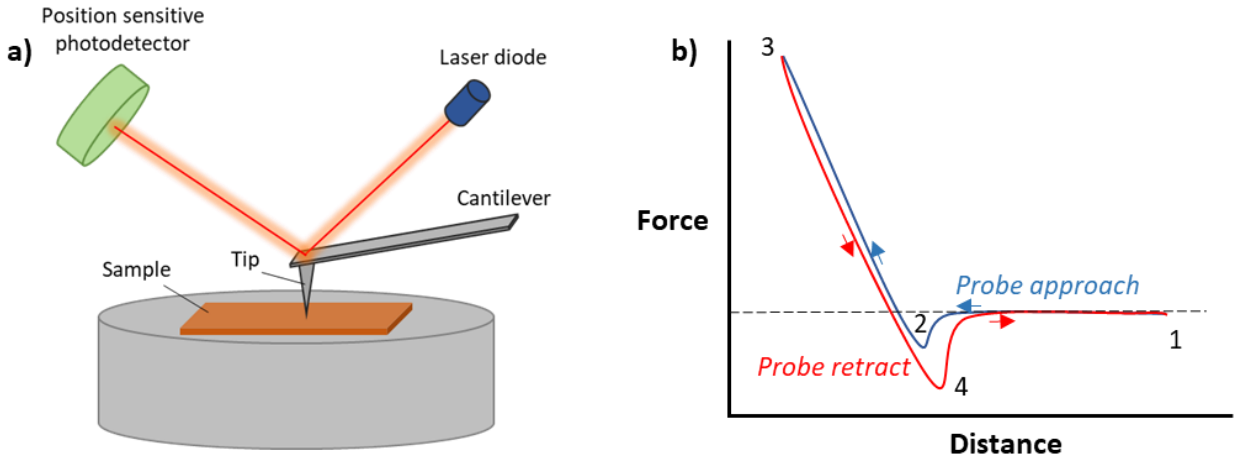

Figure 2.2.2: a) General working principle of an atomic force microscope. b) Exemplary force-distance curve obtained from a nanoindentation experiment.

When operating the AFM in tapping mode, the cantilever oscillates at or close to its resonance frequency at a fixed amplitude. When the tip gets close to or touches the surface, the oscillation of the tip is affected by vdW or electrostatic forces, causing a change in amplitude. To restore the preset amplitude, the cantilever tip is moved away from the surface, resulting in an AFM image produced by the intermittent contacts of the tip with the sample surface. Tapping mode is the most commonly operation mode in ambient conditions or liquids, as it prevents the tip from sticking to the surface, which is one of the main challenges in contact mode.

In the case of the non-contact mode, the cantilever is also oscillating at its resonance frequency while hovering above the sample surface but never touching it. Short-range forces like vdW forces or other long-range forces again decrease the resonance frequency. By instantly resetting the new oscillation amplitude to the resonance frequency through a feedback loop, the distance of tip-to-sample can be measured at any point during the surface scanning procedure allowing the software to generate a topographic image. Compared to the other modes, the non-contact mode does not suffer from tip degradation and also the structure of the sample surface is preserved by this non-invasive mode. Nevertheless, the non-contact mode has slow scanning speeds and is difficult to operate due to the sensitivity needed to create the feedback loop to control the tip-to-surface distance.

The AFM can also be used to perform indentation experiments, a common method to study the mechanical properties of materials at a sub-micron scale. AFM has been used to measure mechanical properties of various objects as thin films,[98] nanoparticles,[99] nanocapsules,[10] nanowires,[100] and cells.[101] During a nanoindentation experiment the AFM cantilever tip acts as indentor, deforming the surface of materials by applying precise and controlled forces as low as several piconewtons while the displacement of the indentor during the indentation process is measured. Mechanical properties such as hardness or Young's modulus can be calculated from force-displacement data. A typical force-displacement curve is displayed in Figure 2.2.2b. The cantilever approaches the sample (1) until contact is made by a "snap-in" effect caused by attractive forces (2). Then the tip is in contact with the sample but continues moving "in" the sample and the applied force increases and the sample is deformed. At that point (3), the cantilever is retracted. As the withdrawal begins the tip starts to unbend until it can disengage from the substrate (4), allowing the cantilever to return to its unperturbed state.

2.2.3 Contact theories of nanoindentation experiments

The correct interpretation of nanoindentation data is crucial to precisely display the real mechanical properties of the objects studied. Several factors such as the geometry and size of the sample, the substrate-effect, the mathematical model used for the calculations and the shape of the indenter used, all strongly influence the final results.

The indentation of thin films using AFM nanoindentation is often described using the Oliver-Pharr method.[102] This method allows the calculation of the Young's modulus from the retraction curve in load-displacement curves. The theory by Oliver-Pharr is based on monolithic materials and identical elastic properties of film and substrate. Then the reduced Young's modulus E_r is defined as:

$$\frac{1}{E_r} = \frac{(1-v_i^2)}{E_i} + \frac{(1-v^2)}{E} \tag{2.2.6}$$

where v_i and E_i are the poisson's ratio and Young's modulus of the indentor and ν and E of the indented material.[102]

When the elasticity of film and substrate are different, eq. 2.2.6 yields incorrect values for E_r, since the deformation of the substrate also contributes to measured apparent elastic modulus and can therefore not be neglected. The approaches of King[103] and Saha-Nix[104] take account for the effect of the substrate on the indentation data and thus yield adjusted values for the modulus by extracting the intrinsic mechanical properties of the film. The Saha-Nix model defines the reduced modulus as:

$$\frac{1}{E_r} = \frac{(1-v_i^2)}{E_i} + \frac{(1-v^2)}{E}\left(1 - e^{-\frac{\alpha(t-h)}{a}}\right) + \frac{(1-v_s{}^2)}{E_S}\left(e^{-\frac{\alpha(t-h)}{a}}\right) \tag{2.2.7}$$

where t is the film thickness, h the indentation depth, α the numerically determined scaling parameter, a the square root of the projected contact area and v_s and E_s the poisson's ratio and Young's modulus of the substrate.

In the case of nanoobjects, the geometry must be carefully considered when calculating material parameters like the Young's modulus. Different theories apply for solid nanoparticles compared to nanocapsules with a core-shell geometry. When studying spherical nanoparticles with a solid core by AFM nanoindentation, the material parameters are commonly calculated by the Hertz theory.[105] The Hertzian elastic contact theory is the most used approach to interpret nanoindentation data of spherical objects, providing a simple expression for modeling the tip-sphere contact. The theory has been experimentally demonstrated to be valid for small deformations by a non-adhesive elastic polystyrene nanosphere against a plane.[95] The normal load *F* was defined by Hertz as:

$$F = \frac{4E\sqrt{R^*}}{3(1-\nu^2)}\delta^{\frac{2}{3}} \qquad (2.2.8)$$

where *E* is the Young's modulus, R^* is the relative radius of curvature for indentor and sphere, ν the Poisson ratio and δ the deformation. However, equation 2.2.8 is only valid, when the modulus of the indenter is much higher than the modulus of the sample. Otherwise the effective Young's modulus needs to be used.

In addition to the Hertz theory, the Johnson-Kendall-Roberts (JKR) model is taking the presence of adhesive forces at the indentor-sphere contact into account.[94] This makes the JKR model suitable for highly adhesive systems of low stiffness. The applied load for adhesive systems, including the Hertz normal load *F*, was defined as F_{JKR}:

$$F_{JKR} = F + 3\pi W R^* + \sqrt{6\pi W R^* + 9\pi^2 W^2 R^{*2}} \qquad (2.2.9)$$

where *W* is the work of adhesion and R^* the relative radius of curvature of the sphere. The JKR model allow a better estimation of the modulus of a material when the adhesion work is important. Otherwise, using the Hertz modulus would result in an overestimation of the modulus as seen for polystyrene NPs of 50-1000 nm in diameter when studied by AFM nanoindentation.[95] The Young's modulus of the same poly(styrene) nanoparticles was calculated using either the Hertz or the JKR theory, and the modules calculated were 3.5 GPa and 1.9 GPa, respectively. Similar effect has also been observed in the study of the micromechanical properties of soft surfaces.[106] In the JKR model, the adhesion work is explicitly taken into account, and this adhesion work can directly be obtained from the jump-off contact of the AFM indentation curve.

The deformation of nanocapsules in nanoindentation experiments is described by the theory of Reissner:[107]

$$F = \frac{4Eh^2\delta}{R\sqrt{3(1-\nu^2)}} \qquad (2.2.10)$$

where *h* is the shell thickness and *R* the capsule radius. Reissner`s theory is limited to small deformations, smaller than the shell thickness of the capsules. Furthermore, the theory is only appropriate for capsules with a shell-to-diameter ratio of $h/R < 1/20$.

Berry et al. compared the models of Hertz and Reissner by numerical simulations.[108] The two models can be seen as solutions of both limits of the *h*/*R* ratio. While the Hertz theory is valid for solid particles with $h/R=1$, the Reissner theory is applied for capsules with $h/R << 1$. For objects with thick shells, a non-dimensional solution for the Hertz and Reissner theories was introduced, allowing a transition between solid particles and thin shell capsules:

$$\frac{F\sqrt{3(1-\nu^2)}}{(h/R)^3 4R^2} = E\beta\left(\frac{C\delta_{afm}}{h}\right)^{\alpha} \qquad (2.2.11)$$

with α as scaling exponent and β as scaling coefficient.

Furthermore, the choice of the nanoindentor itself is crucial as objects can show different deformation behavior depending on the indentor geometry and indentation depth. The geometry of the nanoindentor, more specifically the tip radius of curvature and the tip corner angle, can affect the displacement within the indented objects. Studies on the hardness of a photoresist material by performing nanoindentation experiments using indenters of varying tip radius of curvature and tip corner angle showed, that a rounded tip leads to an overestimation of the measured hardness due to the tip radius of curvature effect.[109] By performing a geometrical deconvolution process the systematic error from the tip radius of curvature effect can be leveled out. Additionally, larger tip radii make the imaging process more difficult as less details of the topography can be obtained.

Nanoindentation experiments can be performed with indenters of various geometries. Some commonly used tips are displayed in Figure 2.2.3. Sharp tips such as the Berkovich-tip or cube-corner tips have the advantage that they can be used for AFM imaging of the objects and for nanoindentation experiments. Colloidal indenters can be used for large and small deformations simultaneously and facilitate nanoindentation of soft materials. The Vickers-tip is made of a square pyramid with four identical faces, giving the advantage of geometrically similar indents regardless of size or indentation depth.

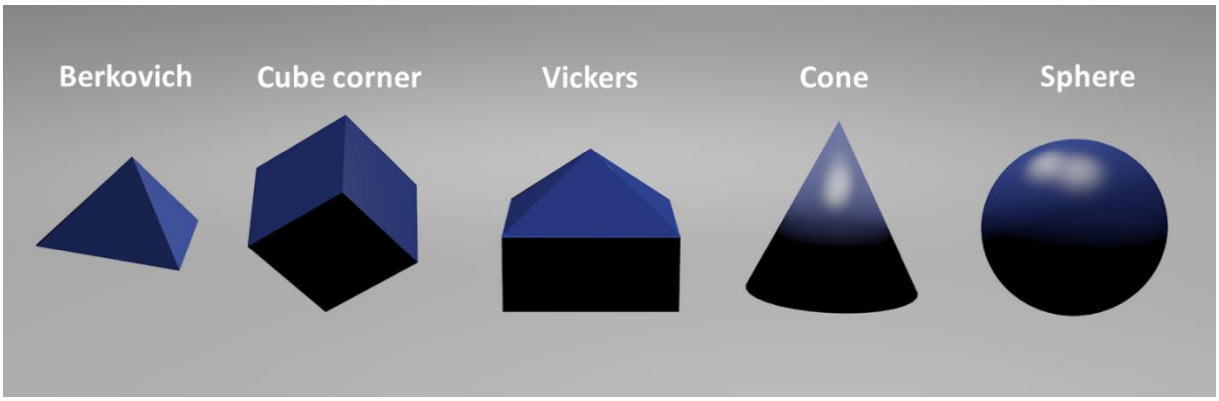

Figure 2.2.3: Nanoindenters of different shape.

In addition to the indentor shape, the indentation depth is also important. Oliver and Pharr showed, that smaller indentation depths lead to a higher hardness compared to large indentation depth when studying single-crystalline silver nanoparticles.[110] Similar results were observed for thin gold films.[111] A detailed analysis of this phenomenon showed, that the formation and movement of new dislocations is hindered for shallow indentation depths.[112] This leads to an increased density of dislocations and thus a hardening effect.

Additionally, the effect of a hard substrate on the deformation of objects during indentation is often-neglected in literature but plays an important role in the correct estimation of hardness or Young's modulus.[108] For example with the indentation of a nanoparticle, during the indentation, the object is compressed by the tip at the upper surface, the indentor deforms the NPs at the top, but simultaneously, the NP is also deformed at the bottom by the substrate (Figure 2.2.4). The tip displacement measured by AFM accounts for both deformations. Therefore, neglecting the substrate effects can lead to an underestimation of Young's modulus by up to 100%.[108] [95]

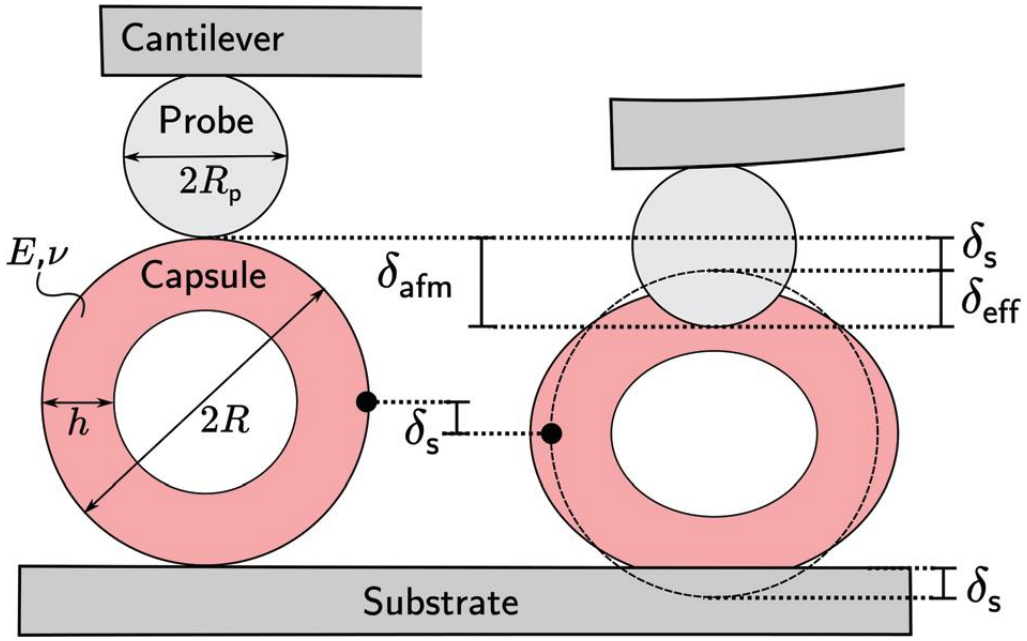

Figure 2.2.4: Schematic deformation of a capsule at top and bottom using AFM. A capsule of radius *R*, shell thickness *h*, Young's modulus *E* and Poisson's ratio ν is indented by a distance δ_{afm} with a probe of radius R_p attached to a cantilever. Reproduced from Ref. [108] with permission from The Royal Society of Chemistry.

2.2.4 Effect of the architecture and assembly of oxide nanomaterials on their mechanical properties

2.2.4.1 SiO_2 nanomaterials

Oxide nanoparticles are composed of oxygen dianions at the oxidation state -2 and at least one other element. Typical oxide nanoparticles are composed of titanium, iron or silicon oxides. Metal oxide nanomaterials are widely used due to their unique properties, as nonlinear optical properties, higher ductility at elevated temperatures, catalytic activity, sensitivity and selective activity.[113] The mechanical properties of oxide nanoparticles are influenced by size and shape, but also the crystallinity of the material. An overview of the existing work is given in Table 2.2.1.

Table 2.2.1: Mechanical properties of SiO_2 nanoparticles with different size and shape, and as assemblies.

Material	Architecture	Size (nm)	Young's modulus (GPa)	Hardness (GPa)	Note	Ref.
SiO_2	Bulk	-	69.3	8.3		**[114]**
SiO_2	Nanoparticle	42	76.5	3.5		[99]
SiO_2	Nanoparticle	75	69.4	2.8		[99]
SiO_2	Hollow NP	110	5.0	-	20 nm shell	[10]
SiO_2	NP assembly	10	12	1.2		[115]
SiO_2	NP assembly	167	2	0.1		[115]
SiO_2	Hollow NP assembly	100	0.7	-	14 nm shell	[10]
SiO_2	Hollow NP assembly	300	0.06	-	14 nm shell	[10]
SiO_2	Hollow NP assembly	300	0.3		44 nm shell	[10]

For example, spherical silica nanoparticles (SiO_2 NPs) were studied by AFM nanoindentation.[99] A conical tip was used to perform indentation experiments on single SiO_2 NPs of 42 to 75 nm of height as measured on the AFM substrate. The Young's modulus was found at 69 GPa while the hardness was determined to be 2.8 GPa. Comparing both values of modulus and hardness to bulk SiO_2

materials, the Young's modulus is very similar (69.3 GPa) while the hardness of bulk SiO_2 (8.3 GPa)[114] is much higher than for SiO_2 NPs. No clear effect of particle size on the modulus or hardness was observed for SiO_2 NPs. However, the deformation behavior of SiO_2 NPs appeared fully reversible as the indent mark of 5 nm depth caused by the conical tip could not be observed during an additional measurement of the surface a few moments later, indicating the fully elastic behavior of SiO_2 NPs for small deformations.

The structure of the SiO_2 nanomaterial can affect the apparent mechanical properties. For example, solid nanoparticles and hollow nanocapsules with a thin SiO_2 shell display different behavior. The mechanical behavior of those two types of NPs can be described by different theoretical models. The Hertz theory is valid for solid spheres, while the Reissner theory can be used with hollow capsules. The later takes into account that the deformation behavior of a hollow nanocapsule is different from solid particles. With regard to individual hollow SiO_2NPs (110 and 268 nm) the Young's modulus was found to be between 3 and 8 GPa much lower than that of solid SiO_2 NPs.[10] This effect can be fully ascribed to the architecture of the nanomaterial as described in the Reissner model, and not to new nanoscale effects.

Besides testing the mechanical properties of single SiO_2 NPs, an assembly of silica NPs was studied by AFM nanoindentation using a conical indentor.[115] Precisely, SiO_2NPs of one diameter (ranging from 10 to 289 nm) were deposited on a glass substrate to form a film of ca. 15 µm thickness. For larger NPs (107 nm and bigger) a face-centered-cubic (fcc) packing was observed, while the assembly of smaller NPs was fully disordered. The performed nanoindentation experiments showed that Young's modulus and hardness both increased dramatically with decreasing particle diameter. The modulus of the smallest tested SiO_2NPs assemblies (10 nm) was 15 times higher than for the largest NPs assemblies (289 nm), while the hardness of the smallest NPs even increased by 39 times compared to the largest NPs tested. This study demonstrates that the hardening effect with decreasing particle size can also be found for the assembly of multiple NPs. Here, the fundamental mechanism is linked to the increasing number of interparticle-junctions at smaller NPs size. More junctions mean more van der Waals interactions and capillary forces, which outruns the decreasing interparticle-junction shear strength for small NPs and therefore leads to the observed increase in hardness with decreasing particle size. Another study on the mechanical properties of assembled nanoparticles was performed via AFM nanoindentation. Here, a monolayer assembly of hollow SiO_2 NPs of varying particle

diameter (100 to 300 nm) and shell thickness (14 to 44 nm) were investigated (Figure 2.2.5).[10] The measured Young's modulus changed with the diameter of the hollow SiO_2 NPs from 0.7 GPa for 100 nm to a significantly lower value of 0.06 GPa for 300 nm diameter. For a constant diameter but increasing shell thickness (14 to 44 nm), the determined Young's modulus increased with increasing shell thickness from 0.06 GPa to 0.3 GPa. Therefore, a strengthening effect for the hollow NPs was observed for smaller particles and for thicker shells. The experimental data was supported by FE simulations, which revealed that contacted individual particles consecutively underwent the same stages of deformation from local bending to a flattened top to a buckled dimpled top. Comparing the results for an assembly of hollow SiO_2 NPs with the mechanical properties of solid SiO_2 NPs assembly, the solid particles show higher stiffness with a modulus of ca. 3 GPa compared to 0.7 GPa for hollow particles of the same diameter. However, the modulus for solid SiO_2 NPs was measured for a 15 µm thick assembly, whereas the hollow particles existed only in a monolayer. Therefore, the monolayer of hollow particles can be affected by the substrate effect described in 2.2.3, leading to a potential underestimation of the real Young's modulus. When juxtaposing the mechanical properties of individual SiO_2 NPs and their assemblies, the individual particles appear stiffer and harder than their assemblies. However, a direct comparison between single NPs and assemblies is difficult, as the force is distribution of assemblies is not the same as for individual SiO_2 NPs. Further, vdW and capillary forces play a larger role in assemblies, as many NPs are in direct contact with each other causing attractive and repulsive interactions.

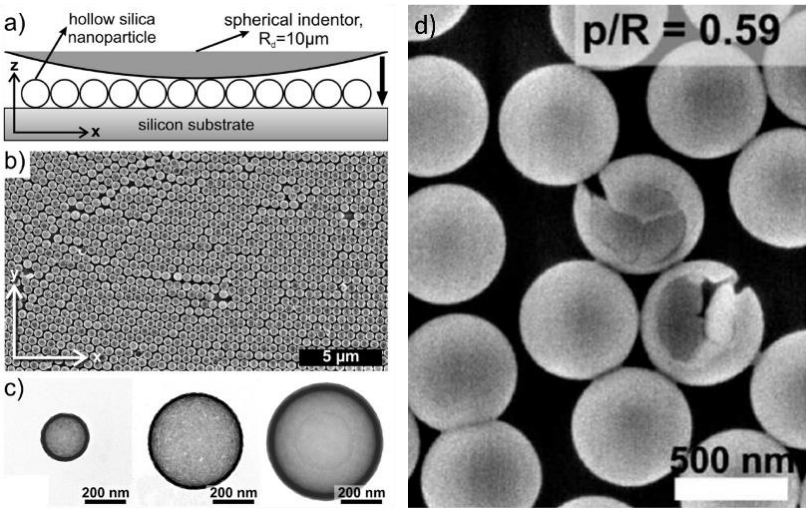

Figure 2.2.5: Hollow SiO_2 NPs (HSNPs) assembly. a) Schematic illustration of indentation of close-packed HSNPs using a spherical indentor. b) SEM image of the particle array. c) TEM images of individual HSNPs of different diameter and shell thickness. d) SEM image of HSNPs after indentation experiment. Reproduced from Ref. [10] with permission from American Chemical Society.

2.2.4.2 TiO_2 nanomaterials

TiO_2-based nanostructures find application as additives to strengthen PS films[116] but also in biomedical applications as for example metallic titanium implants.[117] When investigating the size and temperature dependence of the Young's modulus for TiO_2 nanowires, an increase in Young's modulus with decrease in nanowire diameter was observed. To control the wire diameter, the number of formula units (FU) per unit cell was varied for the respective simulations. The smallest TiO_2 nanowire of 9 FU gave a Young's modulus of 429 GPa, while the largest nanowire of 81 FU showed a modulus of 368 GPa. In relation to absolute size, 9 FU equal a corner to corner distance of 10.07 Å for the oxygen atoms framing that particular unit cell, while 81 FU equal a corner to corner distance of 37.81 Å. Comparing these values for nanowires to the results obtained for nanotubes, the tubes showed a higher Young's modulus for similar size (formula units). The nanotubes were obtained from removing 9 FU from the 81 FU nanowire to obtain a hollow structure. The Young's modulus for such a 72 FU nanotube was found at 383 GPa. Additionally, a lower modulus for distorted nanotubes compared to intact nanotubes was determined, showing the superior properties of defect-free structures. The Young's modulus for TiO_2 nanotubes and nanowires decreases with increasing temperature. The most significant drop in modulus was found for distorted nanotubes and the smallest nanowire, as the modulus decreased by 11–14% when increasing temperature.

2.2.5 Applications

The field of nanotechnology experienced a significant increase in attention due to new exiting materials produced over the last decades. Especially now that NPs of various compositions are finding application in many fields like the remediation of contaminated groundwater with iron NPS.[118] However, there are also numerous applications where not only the chemical properties of the NPs, but their mechanical properties, are playing an important role.

2.2.5.1 Drug delivery

Understanding the mechanical properties of nanomaterials is of fundamental importance in many biological, pharmaceutical and food processing applications. With regard to drug delivery, the accurate measurements of stiffness and hardness help understanding the biodistribution of a given nanocarrier system in the human body. The mechanical properties can influence the cell uptake of nanoparticles,[119] and the circulation time of hydrogel microparticles within the bloodstream.[24] For example, the circulation time of hydrogel microparticles composed of 2-hydroxyethyl acrylate, mimicking red blood cells in size and shape, was correlated to their modulus.[24] A decrease in the Young's modulus altered the biodistribution properties of the microparticles, allowing them to bypass several organs, where their more rigid counterparts were trapped. An 8-fold decrease in hydrogel modulus led to a 30-fold increase in circulation time.

Drug delivery inside the human body by nanomaterials can be triggered through physiological or external forces which is known as mechanoresponsive release. These materials are able to react to three different forces: Compression, tension, and shear (Figure 2.2.6). Compression-responsive systems are typically composed of viscoelastic polymers with a time-dependent strain rate. For example, elastic layer-by-layer microparticles showed release of a model drug under the influence of cyclic compression events.[61] Alternatively, tension-responsive systems use soft and often elastomeric materials. Tension is an ideal stimulus in drug and protein delivery due to its ubiquity in the dynamic nature of the human body. For example, drug-loaded nanocapsules were embedded in an alginate microgel depot on an elastomeric film. Upon the application of tensile strain to the elastomer film, release of the drug from the microgel depots was promoted.[120] Another type of mechanoresponsive systems relies on reversible material deformation or disaggregation upon the application of shear.[121] The main area of application for such materials is the cardiovascular system, as narrowing vessels can increase the local shear stress significantly.[122] Microscale aggregates of

nanoparticles, where the single NPs carry the therapeutic agent by immobilizing drugs or enzymes, remain aggregated when flowing in the bloodstream but disaggregate under the influence of high local shear stress induced by narrow vessels.[121] [123] The single NPs experience much lower drag forces as their aggregates and therefore adhere more efficiently to the surface of the adjacent blood vessel wall. Thereby, high concentrations of NPs and therapeutic agent can be achieved locally.

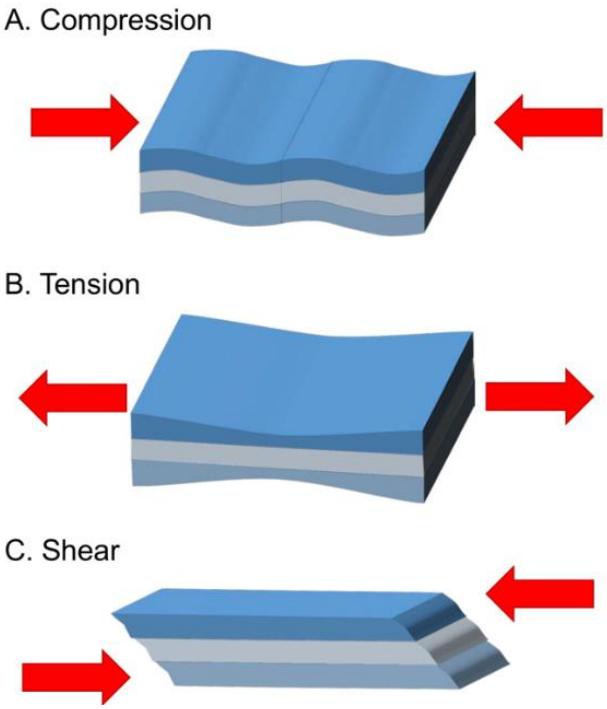

Figure 2.2.6: Schematic representation of a) compressive, b) tensile and c) shear forces to trigger release from mechanoresponsive materials. Reproduced from Ref. [23] with permission from Elsevier.

2.2.5.2 Damage sensing

The exposure of materials to environmental stress causes damage and can eventually lead to failure. Monitoring the integrity of the materials can provide a warning of impeding failure. Such features can be extremely beneficial in coatings for e.g. airplanes or ships where intact surfaces are of central importance. In general, the use of smart materials able to mimic the ability of living systems to protect, report and heal the damages could increase the lifetime, safety and sustainability of many manufactured items. Systems able to sense damaged structures are often based on microcapsules which can release dye molecules upon mechanical damages and are used to locate the harmed area.[124] For example, embedding poly(urea-formaldehyde) microcapsules containing solutions of a solvatochromic dye into a polymer films formed a damage reporting system. When the film was damaged, the capsules released the dye solution in the polymer film and following drying, the change in the polarity of the environment around the released dye molecules led to the apparition of fluorescence.[125] Furthermore, nanocarrier systems can combine multiple functionalities and simultaneously report mechanical damages and induce self-healing to restore the original material properties.[25] This was achieved by the development of a three-component capsule which contains an inactive dye in the liquid core, a protective polymer shell and color-developing silica NPs on its surface (Figure 2.2.7). Breakage of the shell leads to the reaction of the inactive dye with the silanol groups of the SiO_2 and therewith a change in color of the now active dye. The robustness of the capsule determines the level of force needed to cause shell fracture and initiate the color change. The visually highlighted spots can be erased through the interaction of the dye with manually added multivalent alkyne and azide monomers acting as healing agents.

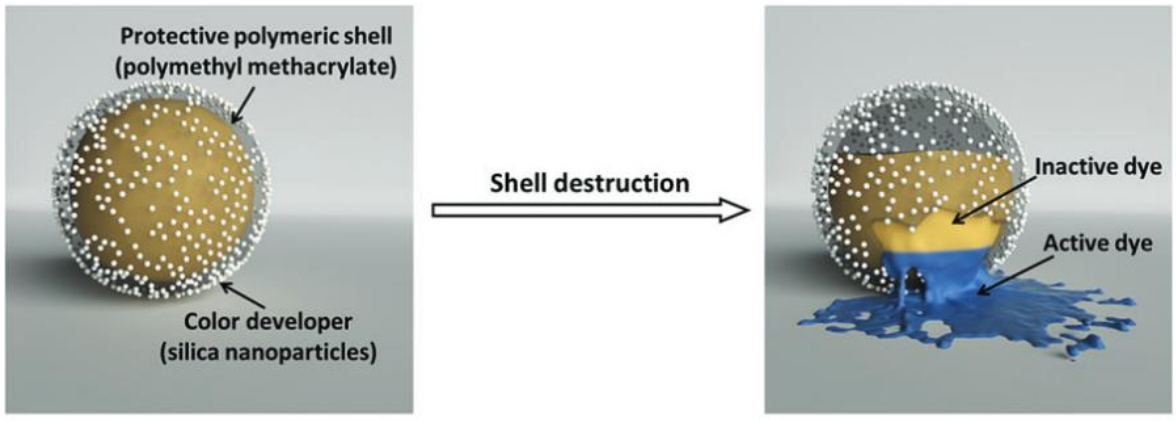

Figure 2.2.7: Scheme of damage self-reporting capsule with the colorless inactive dye becoming active upon damaging of the protective polymer shell. Reproduced from Ref. [25] with permission from Materials Horizon.

2.2.5.3 Chemical mechanical polishing

NPs generate a self-polishing effect when they are located between two moving surfaces, which can potentially lead to the production of atomic smooth surfaces. This effect is used in chemical mechanical polishing (CMP), where NPs have been widely used in polishing slurries. In such applications, the interaction between the nanoparticles and a solid surface leads to a polishing effect of the surface by removing materials from the asperities on the surface to be polished. Typically, the self-polishing effect is predominantly ascribed to molecular adhesion forces of the two contacting bodies at the nanoscale. These interactions in CMP result in friction which can polish surfaces to an atomic level. However, too much friction can also lead to the opposite effect and damage the surfaces, making the modeling of the material removal rate (MRR) crucial.[126] Besides the adhesion of NPs to the surfaces, also collisions of NPs into the surfaces are responsible for the removal of material from the surface. Important parameters for effective polishing are the movement speed of the NPs and the incident angle when colliding with the surface. Furthermore, numerous other parameters are involved in the material removal process, such as the type of abrasive, pressure on the surface, polishing pad or substrate characteristics.[127]

CMP is an important tool in the manufacturing of ultra-smooth surface for computer hard disc drives or as the key step of silicon processing in semiconductor technology. Furthermore, CMP has been widely used in dielectrics (SiO_2,Si_3N_4, polymers, etc.), metals (W, Al, Cu, etc.) and semiconductors (SiC, GaN, Si, etc.) for advanced integrated circuit manufacturing and other emerging technologies. The NPs used in CMP slurries are often made of robust SiO_2,[128] CeO_2[129] and Al_2O_3.[130] For example, SiO_2 NPs are used in CMP of sapphire wafers[131] or steel surfaces,[132] where the polishing effects are mainly based on mechanical abrasion.

2.2.5.4 Lubrication

While some NPs are finding applications in slurries for chemical mechanical polishing, other NPs are used as additives in lubricants to reduce friction at the tribological contact. Roughly 50% of NPs used as lubricant additives are made of metals or metal-oxides.[4] NPs made of iron, copper and cobalt were tested as additives in mineral oil lubricants and showed reduction in friction of up to 1.5 times.[5] However, to stabilize the NPs in suspension, surface functionalization is often required. The addition of silica and titanium NPs to poly(α-olefin) oils requires the functionalization of the NPs with hydrophobic moieties, for them to demonstrate their friction and wear reducing properties.[133] [134] Not only the presence of nanoparticles in a lubricant can reduce the friction observed, but it can also decrease the damage to the surface. Overtime, a self-polishing effect can be observed, which can be understood as desired wear leading to a smoothening of the surface. For example, the addition of spherical TiO_2 NPs in a paraffin oil reduced the depth of the wear scar by 81% compared to the same lubricant without NPs.[135]

2.3 Lubrication

The main task of lubricants is the reduction of friction and the protection against wear to extend machine runtimes and thereby protect raw materials. The scientific field of tribology is facing these complex challenges of reducing friction and wear by the correct application of lubrication. Although the use of lubricants is as old as mankind, the scientific focus on new lubrication technologies is of great contemporary importance. As sustainability becomes more and more important for life- and industrial-oriented applications, saving energy and resources together with reducing emissions should be the central motivation.[3] The energy consumption that can be ascribed to tribology is immense, as an estimated 23% of the world´s total energy consumption originates from tribological contacts.[1] 20 out of 23% is used to overcome friction, while only 3% of the energy are consumed due to wear-related failures. By developing new surfaces, materials or additive strategies, the reduction of friction and wear can be achieved. It is estimated that the largest, short term (8 years), energy saving can be achieved in the field of transportation by cutting down the consumption of energy by 25%. Therefore, advanced tribological technologies can play a massive role in the CO_2 reduction by potentially saving 1,460 $MtCO_2$ and 450,000 million Euros in the short term.[1]

The mechanism of lubrication is based on the physical and chemical interactions between lubricant molecules, material surfaces and the environment. Nowadays, lubricants are complex mixtures of numerous additives together with a base oil.[136] A promising class of additives that gained growing interest in recent years are nanoparticles (NPs). NPs, usually less than 100 nm in diameter, are able to enter the region of tribological contact, allowing to precisely tune the tribological properties of the system. Compared with other organic additives, NPs are often considered as thermally stable at high temperatures, making NPs favorable as lubricant additives.

2.3.1 Friction, wear, and lubrication

The tribological system consists of four elements which are the two interacting surfaces, the interface between surfaces and the environment surrounding the tribological contact. Lubricants are located in the gap between the surfaces, which are in relative motion to each other. Tribological data, as friction, wear and temperature, can be gathered from the contact area. The contact between two friction partners can be physical, physical-chemical or chemical in nature.

2.3.1.1 Friction

Friction can be understood as the mechanical force resisting movement (dynamic or kinetic friction) or hindering movement (static friction) between sliding or rolling surfaces. The reason why friction can be observed in general is the interactions of microscopic asperities of the surfaces in contact. These interactions cause adhesion, material deformation and grooving. Typically the loss of energy due to friction can be measured as heat or mechanical vibrations.[137]

Friction itself is defined as the dimensionless ratio of the friction force *F* and the normal force *N* (Figure 2.3.1a). Further, friction can be differentiated in static and kinetic friction. Static friction is understood as the maximum force that must be overcome to initiate macroscopic motion between two bodies. On the other hand, kinetic friction is ascribed to the coefficient for bodies already in relative motion to each other. Typically, the kinetic coefficient of friction, sometimes also the dynamic coefficient of friction, is smaller than the static coefficient of friction.

Surfaces in relative motion to each other can be described by sliding- or rolling friction, depending on the type of movement itself (Figure 2.3.1b and c).[138] [139] Sliding and rolling friction can both be observed in roller bearings. Rolling friction can be found between the rolling elements and the raceways. At the same time, sliding friction can be observed between the rolling elements and the cage of the roller bearing.

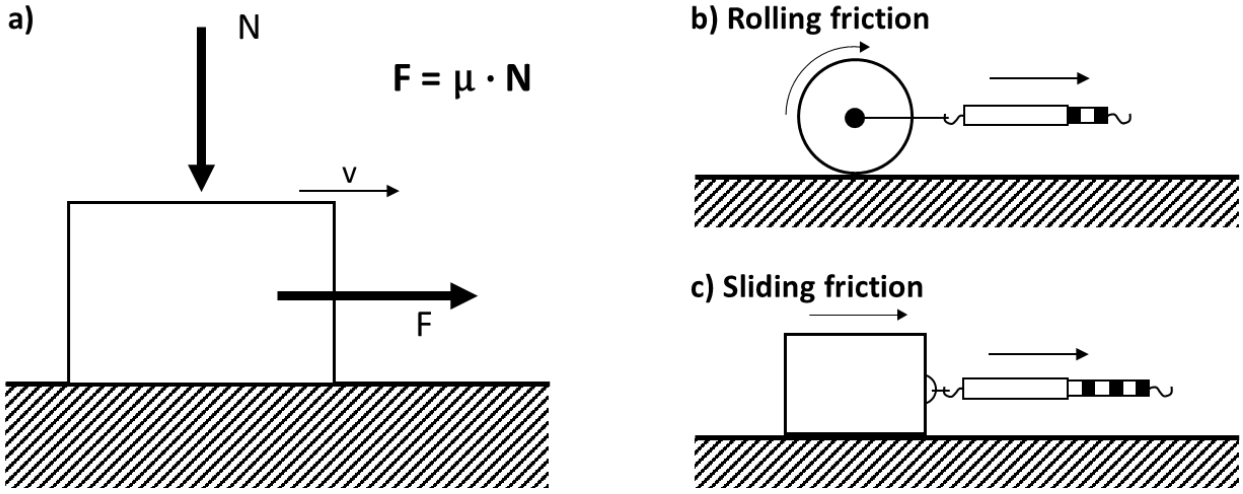

Figure 2.3.1: a) Friction as dimensionless ratio between friction force F and normal force N. b) Rolling friction of a spherical object on a surface and c) sliding friction of a cubic object on a surface.

2.3.1.2 Boundary, mixed and hydrodynamic lubrication

The main task of lubricants is to reduce or avoid the contact of microscopic asperities between surfaces in order to reduce friction and wear. In tribological systems, different types of contact are present, resulting in solid friction, boundary friction and fluid friction. Solid friction occurs when two solid surfaces are in direct contact with each other and no separating layer is present. Such contact leads to extremely high friction and wear, which makes solid friction unwanted in lubrication. By the addition of a substance to form a molecular layer between the contacting surfaces, boundary lubricating films can be achieved. The thin film of lubricant is formed by surface-active molecules, able to significantly influence the friction and wear characteristics of the tribological contact. Although direct contact between the microscopic asperities can still be observed for boundary friction, it is much favored compared to solid lubrication, where no lubrication is present at all. When both interacting surfaces are fully separated by a fluid lubricant film, fluid friction is achieved. The lubricant film, which can be formed hydrostatically or hydrodynamically, reduces friction and wear of the surfaces in interaction. The measurable friction in the fluid friction regime originates from the resistance of the fluid due to its intrinsic rheological properties. The lubrication in fluid friction contacts is often referred to as hydrodynamic lubrication.

The lubrication conditions between boundary and fluid friction were graphically described in a Stribeck diagram introduced by Richard Stribeck (Figure 2.3.2).[140] The coefficient of friction is linked to the rotational speed at the contact by the Hersey number,[141] which is defined by the

$$\text{Hersey number} = \frac{\eta N}{P} \tag{2.3.1}$$

where η is the viscosity, *N* the entrainment speed of the fluid and *P* the normal load.

The Stribeck diagram can be understood by thinking of a bearing that starts moving from a still position in the presence of a lubricant (Figure 2.3.2). In regime 1, boundary friction between the plain bearing shaft and the bearing shells can be observed since only a molecular lubricant layer is present. With the increasing peripheral speed of the shaft, the formation of a thicker hydrodynamic lubricant film begins, leading to the mixed friction regime (2). The coefficient of friction decreases significantly up to a minimum which indicates the full formation of a thin lubricant film covering the entire bearing faces. As the speed increases, the friction starts to increase as a result of growing internal friction due to increasing lubricant film thickness. This regime is defined as the elasto-hydrodynamic lubrication

regime (3). With further increasing speed, hydrodynamic lubrication is reached (4). As the thickness of the lubricant film is further increasing in this regime, the internal friction and, therefore, the overall coefficient of friction increase, too.

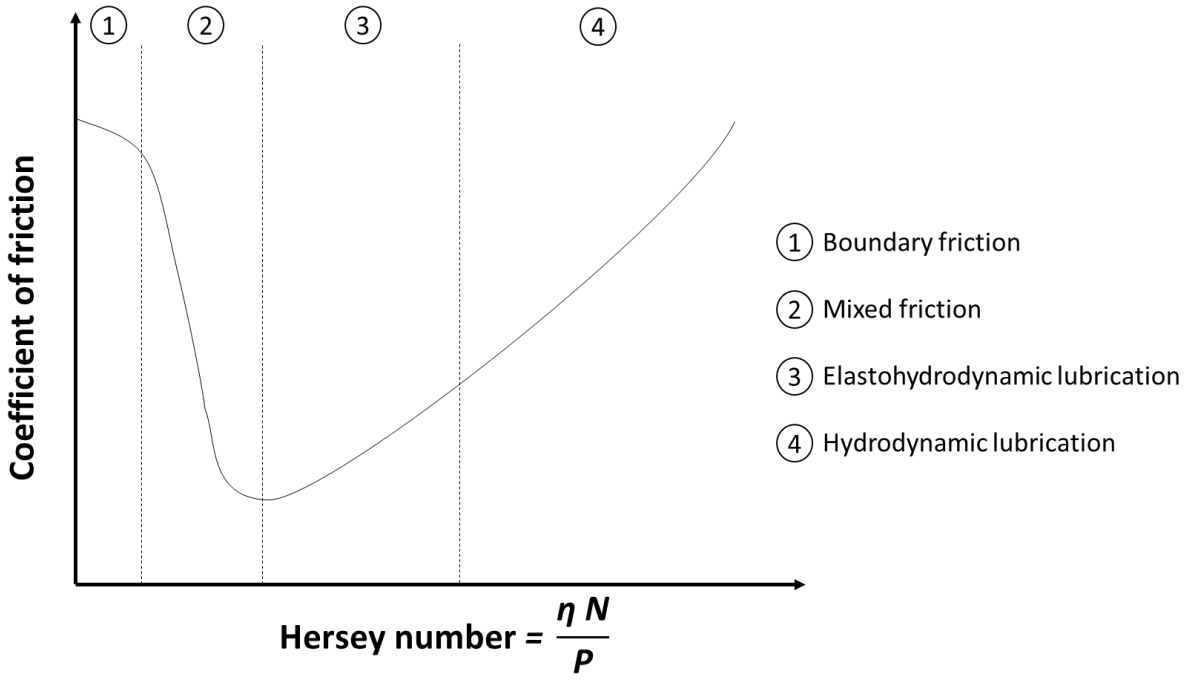

Figure 2.3.2: Stribeck Diagram displaying different lubrication regimes in dependency of the Hersey number.

2.3.1.3 Viscosity

The influence of the internal friction of a fluid on the overall coefficient of friction could be seen in regime 4 of Figure 2.3.2. The internal friction of a fluid is defined as the viscosity. The viscosity can be understood as the force arising between parallel, adjacent layers of the fluid in motion. When the packed fluid layers are subject to shear, individual fluid layers are displaced in the direction of the applied shearing force (Figure 2.3.3). As the upper layers are moving faster than the layers below, molecular forces emerge to resist the movement between layers. This resistance is called dynamic viscosity. The velocity differences between two fluid layers in relation to their linear displacement is defined as shear rate *S*. This velocity gradient shows proportional behavior to the shear stress τ with the dynamic viscosity η being defined as the proportionality constant:

$$S = \frac{dv}{dy} \tag{2.3.2}$$

$$\eta = \frac{\tau}{S} \tag{2.3.3}$$

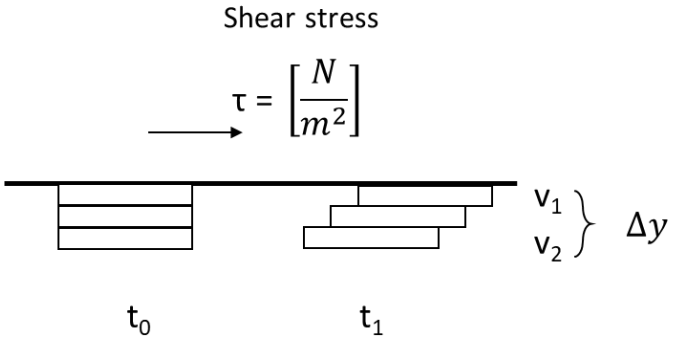

Figure 2.3.3: Illustration of viscosity as sheared fluid layers.

The kinematic viscosity ν defines the relationship between the dynamic viscosity η and the density ρ:

$$\nu = \frac{\eta}{\rho} \tag{2.3.4}$$

The viscosity of a lubricant can be influenced by the environment, as temperature or pressure changes may strongly affect the viscosity.[142] [143] All oils used in lubrication systems show a significant drop in viscosity when the temperature is raised. This drop at higher temperature can be observed, because the molecules forming the sheared layers are having a higher thermal energy of flow, which

allows them to overcome attractive forces between the layers much easier. For linear systems, the viscosity-temperature dependence *V-T* behaves in a hyperbolic manner, making interpretation difficult. By the double logarithmic Ubbelohde-Walther equation:[144]

$$\lg(\lg(v + C) = K - m \cdot \lg T \tag{2.3.5}$$

where *C* and *K* are constants, *m* the slope of the *V-T* line slope and *T* the temperature in Kelvin, a linear slope for the viscosity-temperature dependence could be developed in order to facilitate viscosity calculations. Precisely, the viscosity index (VI) is defined as the gradient between the viscosity at 40 and 100 °C derived from the Ubbelohde-Walther equation.

The viscosity-pressure dependence, which is often underestimated in numerous lubrication applications, plays an important role in the calculations regarding elastohydrodynamic lubrication films. Generally, the viscosity shows an exponential behavior when pressure is increased, which can lead to tremendous viscosity increases in high-pressure systems.[143] The viscosity-pressure dependence results from the chemical structure and especially the steric geometry of the lubricating molecules.

2.3.1.4 Wear mechanisms and types of wear

Wear is defined as the progressive loss of material from the surface of a contacting body as the result of mechanical interactions by the contact and relative movement of an additional contacting solid, liquid or gas with the body. Wear itself is created by processes as abrasion, adhesion, erosion, corrosion, fretting, cavitation, tribochemical reactions, and metal fatigue.[145] Wear is usually not desired in a lubricant system, but at the same time, wear cannot be fully prevented, making low-wear systems desirable.

Abrasive wear, also plowing wear, is caused by the penetration of a body by a harder surface. As a result, surface peaks of the softer body break off or form new abrasive bodies.[146] However, abrasive wear does not necessarily lead to the removal of material from the surface, as plowing effects can push material from the soft body surface to the side to form groves.

Adhesive wear describes the influence of molecular and atomic forces between two friction partners tearing out material particles from the surfaces.[147] When two dry surfaces get in contact, the initial contact is made by surface asperities. Under normal load, the asperity tips of the softer material start

elastic deformation until the plastic contacting surface asperities are cold-welded onto the surface of the harder material. Thereby, strong adhesive bonds are formed, which can be broken by tangential forces causing a shear stress in the junction area. Finally, the shear forces at the contacting bodies interface generate adhesive wear, which is considered proportional to the applied load. Adhesive wear mechanisms are controlled by the size of the asperity contact junction, the work of adhesion of the bulk material and the maximum elastic strain energy which can be stored at the contact.[148]

The removal of chemically reacted surface layers from contacting surfaces is understood as tribochemical wear. These chemical reactions are often heat-induced, as high temperatures can be generated in certain tribological contacts. A study on tribochemical wear observed for a single asperity system showed, that the chemical nature of the substrate determines the level of wear. The applied system based on a silicon nitride AFM tip, which showed significant wear only when interacting with substrates of high metal-oxide density.[149] This may lead to the exposure of chemically reactive surfaces, where the valences of the metal´s structural matrices play an important role.

Surface fatigue is the result of the repetitive application of a load on a specific spot on a surface.[150] By the periodic application of stress, material fatigue can be observed in the form of micro-pits. The effect of surface fatigue can be reduced by thicker lubrication films that sufficiently separate the contacting surfaces.

Erosive wear is induced by the impingement on a surface by a fluid containing solid particles.[151] The particles colliding with the surface remove material from the surface area, causing wear.

Corrosion-induced wear, often observed on steel structures, arises from chemically reacted surfaces due to the presence of air as corrosive medium. By subsequent frictional processes, the chemically reacted surface layers are removed, resulting in corrosive wear.[152]

Fretting, which is combining most of the previously mentioned wear types, can be understood as fatigue wear between two nominally static contacting surfaces.[3] The damage is induced under load and in the presence of cyclic relative tangential motion of very small amplitude, e.g. vibrations. Fretting wear is often referred to as fretting corrosion, as tribochemical reactions may produce oxidized layers which are removed and trapped as wear debris between the contact surfaces.

Cavitation can damage materials by imploding gas and vapor bubbles present in lubricant oils or hydraulic fluids.[153] Common victims of cavitation are the propellers of watercrafts, where usually too high power or running at high speeds for long time induce cavitation and ultimately damage the material.[154] To prevent cavitation in lubrication systems, the elimination of dragged-in air, the use of low boiling point substances or the use of surface-active components are successful strategies.

2.3.1.5 Nanotribology

The comprehensive scientific interest on discovering new trends at smaller scales has also governed the field of tribology. It is believed that deeper knowledge of frictional and wear processes on the micro- and nanoscale can explain different tribological phenomena and further improve economic realization. Nanotribology strives to analyze the movement of single atomic groups in relation to the basic material and measurements of unequally distributed friction forces with nanometer resolution.[3] Further, a deeper understanding of topographical roughness is important to illuminate the relationship between roughness and friction, including the experimental and theoretical analysis of frictional interactions at the atomic level. To enable measurements and visualization on the molecular scale, novel methods or adaption of current measurement procedures is inevitable. Existing strategies include microtribometers that are able to detect forces in the micronewton range, interferometer-based tribometers or atomic force microscopy (AFM) based microanalysis of hardness or elastic modulus. AFM can further be applied to perform friction force measurements at the nanoscale to control the nanoscale friction as studies of multilayered graphene films showed.[155]

2.3.2 Lubricant additives

Modern lubricants consist of 70-90% hydrocarbon molecules forming the base oil and 10-30% of additives governing the tribological behavior, as the base oil cannot satisfy the requirements for high-performance lubricants.[3] [4] Additives, usually synthetic chemical substances, are able to improve existing properties, reduce undesirable properties and introduce new beneficial properties to the lubricant system. Further, additives are able to prolong the lifetime of lubricants as they can reduce degradation processes as oxidation or thermal breakdown. Generally, additives can be classified into two types, depending on how they influence the tribological system: i) Influence physical and chemical properties of the base oil, or ii) influence the metal surfaces by modifying their physicochemical properties. Classic type i) additives, are e.g. additives affecting the viscosity-temperature and viscosity-pressure characteristics, or additives minimizing the oxidation of the lubricant system. Type ii) additives are, for example, wear protection or corrosion inhibition molecules that interact with the metal surfaces.

The concentration of additives in the base oil can vary a lot, depending on the type of additive. While antifoam agents are added to a few ppm, other additives can form up to 30 wt% of the lubricant system. As today's lubricant systems use an array of additives, it cannot always be guaranteed that combined additives show synergistic behavior; in fact, antagonistic effects can be observed as well. This makes a well-matched combination of additives in suitable concentrations a pivotal challenge.

2.3.2.1 Antioxidants

Lubricants have a limited time of use due to the aging processes of the base oil. Aging is the result of oxidation processes and thermal decomposition, although the oxidative aging of the lubricant is the dominant process. Oxidation of hydrocarbons follows a free radical mechanism via alkyl and peroxy radicals and leads to the formation of typical oxidation products as alkylhydroperoxides, dialkyl peroxides, alcohols, aldehydes, ketones, carboxylic acids, and so forth.[156] Further polymerization of these still oil-soluble products can lead to the formation of polymers which may deposit in form of sludge. Additionally, alkylperoxy radicals can attack the metal surface, dissolving parts of it as salts which also deposit in the sludge. Aged lubricants typically show discoloration or a characteristic burnt odor, which is the result of oxidation within the lubricant system.[3] The formed oxidized species may induce corrosion at the tribological contact and thus make the exchange of the lubricant indispensable in order to avoid severe damages at the contact surfaces. By finding the ideal

synergistic antioxidant and metal deactivator combination, the lifespan of the lubricant can be extended significantly.

While refined mineral base oils can contain traces of natural antioxidants as mercaptans, thioethers or disulfides, synthetic lubricants as poly(alpha olefin)s (PAO) require the addition of antioxidants.[157] Generally, antioxidants can work as radical scavengers or peroxide decomposers. While radical scavengers successfully compete with the lubricant for the reaction with radicals, peroxide decomposers convert hydroperoxides into non-radical products. Typical radical scavengers are sterically hindered mono-, di- and polynuclear phenol derivatives or secondary aromatic amines. Typical peroxide decomposers are organosulfur compounds like dialkyl sulfides, diaryl sulfides, polysulfides, thioglycols, and many others.

2.3.2.2 Sulfur carriers

Elemental sulfur has already been added to mineral oils in the early days of lubrication, as sulfur is known to improve the extreme pressure (EP) properties. In EP tribological systems, welding of moving parts and the associated wear are the main challenges to overcome. The addition of sulfur containing components (R-S_x-R) can reduce these undesired effects significantly.[3] [156]

Generally, oil-soluble sulfur compounds, called sulfur carriers, are differentiated by the number of sulfur bonds *x* and the accompanied reactivity. Inactive sulfur carriers provide predominantly disulfide bonds (x = 2), which can be considered as relatively stable as the C-S bond will only react at elevated temperature. Active sulfur carriers (x = 3 to 5) possess much higher reactivity as the labile polysulfide bonds as they can be cleaved at low temperature. The mechanism of sulfur carriers under EP conditions is shown in Figure 2.3.4. The sulfur carriers first adsorb physically to the polar metal surface due to the polar character of the sulfur compound itself. Then, chemisorption occurs by the cleavage of S-S bonds, followed by the cleavage of the C-S bonds, which results in the formation of a sulfur film on the metal surface. The protection against welding is achieved by controlled wear through the removal of slideable sulfur reaction layers under continuously high loads. Active sulfur carriers are also applied as antiwear additives under low-pressure conditions when dispersed in unsaturated esters or fatty oils.

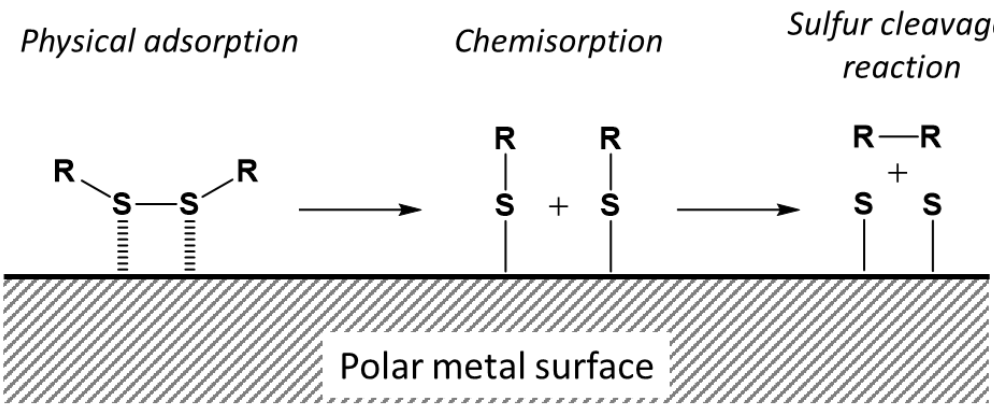

Figure 2.3.4: Sulfur carriers on a polar metal surface showing physical adsorption, chemisorption and finally sulfur cleavage reaction.

Another sulfur-containing additive that is widely applied in the field of tribology is zinc dithiophosphates. These components act mainly as radical scavengers to reduce oxidation but also find application in EP tribo systems.[156]

2.3.2.3 Viscosity modifiers

The viscosity of a lubricant oil is one of the most important characteristics and often needs to match a defined value. The viscosity index (VI), which is precisely defined for lubricants, originates from the molecular structure of the oil. When a certain VI is required for an application, simple mixing of two or more lubricants may allow to reach the desired VI value. To keep the chemical purity of the original lubricant oil and also to meet the specifications of modern lubricants, the VI can be adjusted easily by the addition of viscosity index improvers (VIIs). VIIs are typically polymers whose solubility in the lubricant depends on the chain length, structure and chemical composition. The thickening effect upon the addition of VIIs is linked to the polymer structure, the molecular weight and the concentration of the VII in the oil, but also the coil behavior of the polymer at different temperature regimes.[158] Traditional VII polymers like polyalkyl methacrylates (PAMA) and polyisobutylene (PIB), have molecular weights ranging between 15 and 250 kg/mol and 2 and 5 kg/mol, respectively. The loadings vary between 3 and 30% (w/w).

2.3.2.4 Detergents and dispersants

Detergents and dispersants (DD) are indispensable components of lubricant systems applied in modern engine oils of combustions motors.[136] These lubricants are exposed to high stress and additional blow-by gases originating from the combustion process. The DDs additives are able to keep oil-insoluble combustion products in suspension and further prevent agglomeration of asphalt-like oxidation products. Thereby, oil thickening and sludge formation can be limited. Further, DD additives can reduce corrosive wear as the deposition material on the metal surfaces can be reduced.

DDs are basically surfactants and have the same chemical structure as surfactants with a polar hydrophilic head group and a nonpolar oleophilic tail. Typical DDs that can be found in engine oils are calcium phenates, calcium sulfonates or thiophosphonates.[3]

2.3.2.5 Antiwear additives

When the two interacting surfaces of a tribological contact start moving, the hydrodynamic lubrication film has not formed already. Therefore, boundary or mixed friction are dominant, causing severe wear. To reduce wear, antiwear (AW) additives are added to the lubricant oil.[159] Due to their polar structure, these components form layers on the metal surface by adsorption or chemisorption. The formed layers can smoothen the metal surface asperities and prevent direct contact between the interacting metal surfaces. These layers are forming immediately and thereby reduce the running-in wear significantly. Compared to EP additives, AW additives are usually applied in moderate pressure systems. Typical AW components can be nanoparticles made of MoS_2 or graphite, but also tricresylphosphate or mono- and dialkyl phosphoric acids. However, differentiation between AW and EP additives cannot be precise as certain components can be ascribed to both groups as for example, zinc dithiophosphates.

2.3.2.6 Friction modifiers

Friction modifiers (FM) are added to lubricant oils in order to reduce friction by the formation of thin monomolecular layers.[65] While AW and EP additives work preferably at elevated temperature and pressure, FMs already show a great reduction of friction under mild conditions, making them ideal additives for mixed lubrication systems. Further, FMs are applied in systems with low sliding speeds and low viscosity to prevent stick-slip oscillations and noises by reducing friction at the tribological contact. FMs can be divided in different groups with regard to their functions: Mechanically working FMs (MoS_2, graphite, PTFE), adsorption layers forming FMs (carboxylic acids, fatty acid esters, alcohols, amines), tribochemical reaction layers forming FMs (thiophosphoric acid esters, saturated fatty acids, sulfurized fatty acids), friction polymer forming FMs (methacrylates, dialkyl phtalic acid esters, sulfurized olefins) and organometallic compounds (molybdenum dithiophosphates, molybdenum dithiocarbamates, copper-containing compounds).[3]

2.3.2.7 Nanoparticles

In recent years, a growing interest in using nanoparticles (NPs) as an additive for lubricant systems emerged. Due to their typical size between 5 and 500 nm, NPs can not only pass through filters in oil systems but also remain dispersed in the liquid by Brownian motion. Further, the small size allows the NPs to enter the contact interface nicely. More interestingly, NPs, when applied in the correct way, are able to reduce friction at the tribological contact. The friction-reducing mechanism of NPs in the lubrication process depends on multiple factors like the contact pressure between the surfaces to lubricate or the chemical composition of the NPs. Those factors influence the mechanism through which the NPs may reduce friction (Figure 2.3.5); the NPs can be involved in a rolling, sliding or exfoliation behavior. The appearance of rolling behavior strongly depends on the shape of the nanoparticle but also size and concentration. Spherical nanoparticles without significant agglomeration in the lubricant oil are favorable to follow the rolling mechanism between tribopairs as observed for inorganic fullerene-like WS_2 and MoS_2 nanoparticles.[69] The transition between rolling and sliding behavior is often fluent, as the WS_2 and MoS_2NPs are likely to also follow a sliding mechanisms. Generally, a higher pressure between the two moving surfaces promotes a sliding of the nanoparticles. Also a non-spherical shape of the particles and low adhesion to the tribopairs results in sliding behavior. Finally, when pressure at the tribological contact is very high and the thickness of the lubricating film is less than the particle diameter, exfoliation of the nanomaterial can

occur.[160] This behavior is typically observed for inorganic multilayered NPs and depends on the crystal structure of the particle. Layered NPs may adhere to tribopairs surfaces as a third body upon exfoliation of the particle structure. Thus, friction is reduced by separating the interacting surfaces of the tribological contact.[161] Besides, the exfoliated nanoparticles may fill out valleys between asperities of the surfaces to partly smoothen the contact areas.[162]

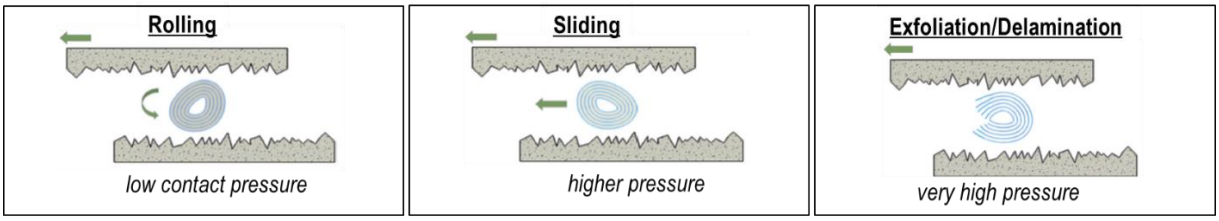

Figure 2.3.5: Rolling, sliding and exfoliation mechanism of nanoparticles between tribopair surfaces. Reproduced from Ref. [4] with permission from Elsevier.

Along with reduced friction, NPs allow the introduction of a chemistry that is usually insoluble in nonpolar hydrophobic lubricant oils. This can be achieved through the nanoparticles themselves or by encapsulating additional molecules inside of hollow nanoparticles. For example, nanoparticles made of metals and metal oxides,[5] silica,[6] graphene[7] and sulfides[8] have been used as additives in order to reduce friction in the lubrication system. At the same time NPs show less antagonistic interactions with other additives, as the NP´s activity is limited to their surface.

3 Methods and experimental

3.1 Materials

Tetraethylorthosilicate (TEOS), 2,4-toluene diisocyanate (TDI) and benzylmethacrylate were purchased from TCI chemicals. Toluene and acetonitrile were obtained from Fisher chemical, and cetyltrimethylammonium bromide (CTAB), sulfur, glycerol, di-tert-butylperoxide and 2-(2-Aminoethoxy)-ethanol from Acros organics. Poly(ethylene glycol) (35 kg/mol), N-methylimidazole, calcium chloride ($CaCl_2$) and rhodamine B isothiocyanate were purchased from Sigma-Aldrich. Hexadecane, hexane, cyclohexane and ethanol were purchased from VWR chemicals, and tin(II) 2-ethylhexanoate from Chem Cruz. Poly(α-olefine) (PAO2) was provided by Fuchs Petrolub. All those chemicals were used as received. α-Methylstyrene and ε-caprolactone were purchased from Alfa Aesar and purified through an aluminium-oxide column to remove inhibitor. Polyglycerol polyricinoleate (PGPR) was obtained from Danisco and purified by centrifugation of a PGPR-cyclohexane solution and subsequent evaporation of cyclohexane.

3.2 Synthesis

3.2.1 Synthesis of silica nanocapsules

Silica nanocapsules (SiNCs) were prepared via oil-in-water miniemulsion. The oil phase was composed of silica precursor TEOS (4 g; 4.255 mL; 19.2 mmol) and hexadecane (3 g; 3.896 mL; 13.3 mmol) and was stirred briefly to ensure mixing of the two components. The aqueous phase was prepared by dissolving 78 mg CTAB (0.2 mmol) in 90 mL deionized water. The two phases were combined and stirred for 10 min at 400 rpm. Then, the mixture was pre-emulsified for 2 min with an Ultra-Turrax at 15 000 rpm. Finally, the pre-emulsified mixture was passed through a microfluidizer (LM10, Microfluidic corp.) equipped with a F20Y interaction chamber with channels of 75 µm at a pressure of 10 000 PSI for two cycles. By varying the pressure of the microfluidizer, SiNCs of different diameters were obtained. After emulsification, the miniemulsion was allowed to react for 24 h by stirring at 600 rpm to obtain final SiNCs. A library of SiNCs was prepared by following the procedure just described and changing the composition of the oil phase.

AFM sample preparation

Freshly prepared SiNCs were dialysed against water for 8 h. Afterwards, 10 µL of purified SiNCs were diluted with 10 mL deionized water and drop-casted on a clean glass slide.

Release study from broken SiNCs

The SiNCs were dialysed against ethanol for 2 d and subsequently dried with glucose (3:1 wt% ratio of SiNCs:glucose). 15 mg of dried capsules were compressed in a hydraulic press from Perkin-Elmer for 30 s at a controlled load of 2, 4, 6, 10 t.

Then, 15 mg of the compressed SiNCs were redispersed in 5 mL EtOH:H_2O (1:1) and then sonicated in an ultrasound bath for 5 min. Finally, the suspension was filtered through a 100,000 MWCO spin filter and the fluorescence intensity of the filtrate was measured at a wavelength of 545-700 nm.

3.2.2 Synthesis of glycerol nanocarriers

Glycerol nanocarriers (GlyNCs) were prepared via inverse miniemulsion. The polar phase composed of glycerol (6.4 g; 5.2 mL; 69.5 mmol), milli Q water (0.32 g; 0.32 mL; 17.8 mmol) and $CaCl_2$ (70 mg; 0.5 mmol), was stirred at 750 rpm for 5 min. The non-polar phase was prepared by dissolving PGPR (0.64 g) in toluene (69.36 g; 80 mL; 0.868 mol). The two phases were combined and stirred for 5 min at 1000 rpm. Then, the mixture was pre-emulsified for 10 min with an Ultra-Turrax at 15 000 rpm. Finally, the pre-emulsified mixture was passed through a microfluidizer (LM10, Microfluidic corp.) equipped with an F20Y interaction chamber with channels of 75 μm at a pressure of 10 000 PSI for two cycles. After emulsification, 40 mL of the obtained miniemulsion was transferred to a round bottom flask and stirred at 750 rpm. Subsequently, a solution of 2,4-toluene diisocyanate (1.579 g; 1.294 mL; 9.066 mmol) in toluene (5.2 g; 6.0 mL; 56.5 mmol) was added dropwise through a dropping funnel. The addition of TDI dissolved in toluene was repeated at 1, 2 and 3 h after the first addition. Finally, the mixture was allowed to react overnight at room temperature.

Purification of GlyNCs and transfer to PAO2

The as-prepared GlyNCs were purified by centrifugation (4 000 rpm; 20 min) to remove PGPR and unreacted TDI. The toluene supernatant was removed and the precipitate was redispersed in fresh toluene. This step was repeated once. After another centrifugation cycle (4 000 rpm; 20 min) the precipitate was redispersed in cyclohexane instead. A known amount of GlyNCs suspended in cyclohexane was added dropwise to 5 g PAO2 in a 20 mL vial while stirring vigorously to give different loading of GlyNCs in PAO2 (5, 10, 15 wt% GlyNCs relative to PAO2). The mixture was stirred in an open vial overnight to evaporate cyclohexane and obtain a suspension of GlyNCs in PAO2.

Tribological measurements

The tribological measurements were performed by using a ball-on-three-plates geometry attached to a rheometer (TA Discovery HR3). The stainless-steel plates were polished manually before the testing. The stainless-steel balls were used as received. A volume of 0.3 mL oil containing different loading of GlyNCs was added to the ball-on-three plates geometry, and coefficient of friction was measured as the sliding speed of the steel-ball was ramped up from 0 to 135 mm/s followed by a ramped down from 135 to 0 mm/s. This cycle was repeated either 5 or 25 times.

Quantification of released glycerol

After the tribological measurement, the ball-on-three-plates geometry was rinsed with 15 mL cyclohexane to collect the suspension of GlyNCs in PAO2 entirely. Subsequently, the mixture was filtered through a 250 nm syringe filter to remove GlyNCs and obtain a clear liquid. By the addition of 15 mL acetonitrile-water mixture (95:5), the glycerol was extracted from PAO2/cyclohexane. After separation of the two phases, the acetonitrile-water mixture was sent through a polar Macherey-Nagel $NH(CH_3)_2$ column (250/4.6/5 µm), allowing to quantify the measured amount of glycerol through a previously recorded internal standard.

3.2.3 Synthesis of polysulfur nanoparticles

Polysulfur nanoparticles (polySNPs) were prepared in miniemulsion. The sulfur-rich dispersed phase was composed of sulfur (1 g; 31.3 mmol), comonomer (4.5 mmol) and initiator or activator (0.25 mmol). The continuous phase composed of glycerol (30 g; 23.8 mL; 0.33 mol) and PGPR (0.42 g; 0.5 mL) was mixed with the oil phase at 130 °C and stirred vigorously for 10 min. Then, the mixture was proceeded to 4 min ultrasonication (15 s pulse/5 s pause) by a Branson SFX 550 sonifier equipped with a ¼" tip oscillating at 70% amplitude. After emulsification, the mixture was stirred at either 130 or 180 °C for 4 h. The suspension in glycerol was dialysed against aqueous solution of sodium dodecyl sulfate (SDS) to yield polySNPs dispersed in water.

3.3 Characterization methods

Atomic force microscopy (AFM)

AFM was realized by using a JPK3 nanowizard with Olympus Micro Cantilevers with a resonant frequency of 70 kHz and a spring constant of 2 N/m. Samples were dropcasted on glass slide from a diluted suspension. For the compression experiments, the force was preset to 500 nN and the cantilever was moved towards the sample on the z-axis. Once in contact with the SiNC, the cantilever continued moving towards the substrate and thereby continuously increased the applied force. When the preset force was reached the cantilever started to retract. Before reaching the preset force, the cantilever usually broke the silica shell, this event was observed as an abrupt step in the force/distance profile.

Cyclic voltammetry (CV)

CV measurements were carried out on a Metrohm Autolab PGSTAT204 potentiostat/galvanostat with a three-electrode-cell system, glassy carbon electrode as the working electrode, $Hg/HgCl_2$ electrode as the reference electrode, platinum wire as the counter electrode, and Bu_4NPF_6 (0.1 M in acetonitrile) as the supporting electrolyte, with a scan rate of 100 mVs^{-1} in the range of -1.5 eV to 3 V. Sulfur films were dropcasted on the glassy carbon electrode and subsequently covered with a film of Nafion perfluorinated resin.

Differential scanning microscopy (DSC)

DSC measurements were performed with a METTLER-TOLEDO DSC 823 at a heating rate of 10 K/min for a temperature range of -140 °C to 150 °C under N_2 atmosphere.

Dynamic light scattering (DLS)

DLS measurements of diluted samples (ca. 1 mg/mL) were performed using a Malvern Zetasizer Nano-S90 measuring at a constant temperature of 20 °C.

Fluorescence spectroscopy

Fluorescence spectroscopy was realized by using a Tecan infinite M1000 platereader measuring from 545 to 700 nm. The measured samples (0.2 mL) were deposited in a Cellstar 96 well plate.

Fourier-Transform Infrared Spectroscopy (FTIR)

FTIR measurements were realized by using a Perkin-Elmer Spectrum BX FT-IR system measuring from 4000 to 400 cm^{-1}.

Gel Permeation Chromatography (GPC)

GPC experiments were performed using an Agilent Technologies 1260 instrument consisting of a pump, auto sampler and column oven. A column set consisting of 3 columns: SDV 10^6 Å, SDV 10^4 Å and SDV 500 Å (PSS Standards Service GmbH, Mainz, Germany), all of 300 x 8 mm and 10 µm average particle size were used at a flow rate of 1.0 mL/min and a column temperature of 30 °C. As eluent THF was used. The injection volume was 100 µL. Detection was accomplished with a RI detector and a UV detector at 254 nm wavelength (Agilent Technologies). Data acquisition and evaluation was performed using PSS WINGPC UniChrom (PSS Polymer Standards Service GmbH, Mainz, Germany). Calibration was carried out by using polystyrene provided by PSS Polymer Standards Service GmbH (Mainz, Germany). Samples to be measured were diluted to a concentration of ca. 2 g/L.

Scanning electron measurements (SEM)

SEM measurements of diluted samples dropcasted on a silicon wafer were performed with a 1530 Gemini LEO (Zeiss) microscope.

Thermogravimetric Analysis

TGA measurements were performed with a TGA3 from METTLER-TOLEDO heating from 25 to 600 °C with a rate of 10 K/min under a N_2 atmosphere.

Transmission electron microscopy (TEM)

TEM was done with a JEOL 1400 electron microscope. Diluted samples were dropcasted on a TEM grid. The shell thickness of SiNCs was determined by measuring 50 NCs via the software ImageJ.

UV-Vis spectroscopy

Absorbance spectra of polysulfur films dropcasted on a glass slide were collected for a spectral range of 300 to 800 nm using Agilent Cary 60 UV/vis spectrometer.

4 Results and discussions

In the field of tribology, the addition of additives to a base lubricant oil is a standard procedure, to increase the overall performance of lubricant systems as well as extending their total lifetime. Modern lubricant systems consist of an array of additives, which need to be well attuned with each other to achieve the maximum performance-improving effect. Also nanoparticles (NPs) are used as additive in lubricant systems, as they are able to enter the contact interface nicely to reduce friction. The friction reducing mechanism of NPs (rolling, sliding or exfoliation behavior) depends on the applied pressure the NP composition. Most NP additives used today in lubricants are made of metals or metal-oxide,[4] [5] but also silica[6] and titanium[133] NPs showed friction and wear reducing properties. Furthermore, NPs enable the introduction of a chemistry that is often insoluble in nonpolar hydrophobic lubricant oils and at the same time show less antagonistic interactions with other additives.[65]

As the world is facing severe energy crisis and one fifth of the world's energy consumption is caused by friction,[1] [2] the urge for innovative materials that are capable of reducing the overall friction are strongly desired. With this thesis, the synthesis of three individual nanoparticle systems, each composed of abundant materials, is demonstrated. The potential of each system as an additive in lubricant system is aiming to encourage the overall development of innovative friction reducing nanoparticle additives. Furthermore, the intrinsic nanoparticle properties of rolling, sliding or exfoliation when exposed at the tribological contact, are combined with the ability to encapsulate molecules inside of hollow nanoparticles to eventually deliver another friction and wear reducing molecule. By applying the extremely versatile technique of miniemulsion, nanocarriers with encapsulated hydrophilic and hydrophobic components can be obtained, allowing the delivery of new chemistry into existing lubricant systems.

The introduction of new chemistry with nanoparticles is typically limited to the materials used to make the particle and in some cases to molecules present on the particle's surface. To introduce a wider range of components, for example friction modifying molecules, the encapsulation of molecules into nanocarriers represents a promising approach. In chapter 4.1, the encapsulation of hydrophobic molecules into silica nanocapsules via direct miniemulsion is demonstrated. The silica nanocapsules showed the ability to release the encapsulated molecules under external forces,

making them mechanoresponsive. Besides the great synthetic control over nanocapsule size and shell thickness, the breaking force of the silica shell is determined by AFM nanoindentation experiments. By varying diameter and shell thickness of the silica nanocapsules, the resistance to external forces can be tuned, allowing for a controlled mechanoresponsive release.

Another important challenge in the formulation of lubricant system is the addition of hydrophilic friction modifiers to hydrophobic oil. The development of nanocarriers containing this type of molecules could be a critical step-forward in the use of such additives. In chapter 4.2, the encapsulation of hydrophilic glycerol into glycerol-based nanocarriers via inverse miniemulsion is presented. The nanocarriers are composed of a polyurethane network and free glycerol, which can be released into the surrounding environment. The amount of free glycerol can be controlled by the added amount of crosslinking agent to form the polyurethane network. Extensive tribological testing of glycerol nanocarriers of different crosslinking ratio, revealed the superior friction and wear reducing properties, when adding the nanocarriers to a base lubricant oil.

Sulfur is added to lubricant systems to mainly reduce wear in the tribological contact under extreme pressure conditions. The addition of sulfur is usually realized by oil-soluble sulfurized hydrocarbons, which however only have limited amounts of sulfur. To enhance the beneficial effect of sulfur in tribological contacts, a sulfur-rich additive is needed. In chapter 4.3, the synthesis of polysulfur nanoparticles of high sulfur content is discussed. This approach allows to combine the friction reducing properties of nanoparticles with the additional opportunity to deliver large quantities of sulfur to the tribological contact. Polysulfur nanoparticles were synthesized via inverse miniemulsion at elevated temperature. The detailed study of the underlying reaction mechanisms leading to the formation of sulfur nanoparticles enabled the synthesis of particles with high molecular weight. Further, they offer a facile processability as they were obtained in an aqueous suspension.

4.1 Tailoring the mechanoresponsive release from silica nanocapsules*

To extend the life span of lubricant systems, a solution would be the responsive release of an additive when the properties of the lubricant system degrade due to lubricant depletion. In order to design an additive which can respond to lubricant depletion and the resulting increased friction, a suitable release trigger is needed. As the increased friction results in higher forces in the tribological contact, mechanoresponsive release is a suitable trigger. The concept of mechanoresponsive nanocapsules can be used to control the release of a cargo under the influence of an external force. The mechanically triggered release of encapsulated molecules can be controlled by tuning the mechanical properties of the nanocapsules, which are strongly linked to the nanocapsule architecture. Silica nanocapsules (SiNCs) with finely tunable diameter and shell thickness represent suitable type of nanocarrier for the described challenges. The mechanical properties of SiNCs were supplemented by AFM nanoindentation experiments to determine the breaking force of single SiNCs. By encapsulating a model payload, which release was triggered by the application of external mechanical force on the SiNCs, the ability of mechanoresponsive SiNCs used as smart nanocarriers could be shown. This innovative nanocarrier system of mechanoresponsive SiNCs is compatible with application in various fields, such as biomedicine, tribology, or chemical polishing, i.e. fields where there is a need to precisely deliver a payload when specific external forces are present. For example, such SiNCs can be used as lubricant additives, where the release of encapsulated lubricant would be triggered once the friction and, therefore, the mechanical stress within a tribological contact increase.

4.1.1 Introduction

As mentioned, triggering the release of encapsulated payloads using mechanical stress acting in a nanocarrier is a strategy with many potential applications. However, the behavior of such mechanoresponsive nanocarriers is dependent on their mechanical properties and their architecture. By tailoring the architecture of the nanocarriers, the breaking force and the amount of released payload was successfully controlled.

Smart nanocarrier systems enable the precise delivery of a payload, and a vast gamut of physicochemical cues are being used to initiate this delivery. Mechanical cues, like load or

*This chapter is based on the article: "Tailoring the mechanoresponsive release from silica nanocapsules" by F. Uebel, H. Thérien-Aubin and K. Landfester, Submitted for publication to Nanoscale. Contributions: F.U., H.T.-A. designed the experiments. F.U.. performed the experiments. F.U. and H.T.-A. analyzed the data. H.T.-A. and K.L. supervised the project.

deformation, are becoming an essential class of triggers for new smart delivery applications, whether in the biomedical field or in more traditional industries. In such cases, the mechanical properties of the nanocarriers are of central importance to control the release. However, there is currently a lack of adequate design guidelines to produce nanocarriers with suitable composition and architecture to predict the release of encapsulated payloads under predetermined mechanical stresses. To address this limitation, we need to establish a relationship between the composition of the nanocarriers and the architecture of the nanocarrier, defined by their size and shell thickness, all of which can influence the mechanical properties of the nanocarriers.

Independently from the encapsulated cargo or the type of nanocarrier, a successful delivery system should ensure the effective encapsulation and release of the payload. The release of an encapsulated cargo from a nanocarrier can occur by two main mechanisms. The cargo can escape the nanocarrier either by a diffusion-induced release or degradation-induced release. Both mechanisms can be triggered by different stimuli, depending on the chemical composition of the nanocarrier system. Such nanocarriers can be thermo-,[17] [18] light-,[19] pH-,[163] enzyme-,[21] or redox-responsive.[22]

One trigger mechanism for the payload release that has a broad appeal in a variety of fields is the release following the mechanical deformation or the application of controlled mechanical stress on the nanocarriers. Such mechanoresponsive systems are used to influence drug delivery inside the human body.[63] [64] Further, these systems are now gaining interest in a broader range of fields, i.e., damage sensors,[25] self-healing materials, [26] stretchable electronics,[27] or lubrication. For example, damage-sensing systems based on microcapsules can release dye molecules upon mechanical damages and are used to locate the affected area.[124] Nanocarrier systems can combine those functionalities and simultaneously report mechanical damages to induce self-healing through the delivery of self-healing agents to the damaged area, and successful recovery of the original material properties can be achieved.[25] In such systems, the application of a force results in the deformation or the breaking of the micro-/nano-carrier leading to the subsequent release of the encapsulated cargo. Therefore, controlling and understanding the physicochemical parameters that dictate the mechanical properties of the delivery system, like shell thickness or the stiffness of the shell, are critical in gaining control over the release from mechanoresponsive delivery systems.

The rational design of mechanoresponsive delivery systems relies on the study of the mechanical properties of the delivery systems at the nanoscale. One method to study the mechanical properties of micro- and nano- capsules is to use the tip of the cantilever employed in atomic force microscopy (AFM) as a nanoindenter to probe single nanocapsules by applying precise forces.[73] AFM is a versatile technique that can not only be used to obtain images with subnanometer resolution but also to apply precise and localized forces as low as several piconewtons.[108] By measuring the displacement of the AFM tip during the indentation process, parameters like Young's modulus, hardness, or breaking forces of nanocapsules can be determined. Previously, AFM nanoindentation has been used to analyze a variety of micro- and nano-carriers[164] [165] [166] or even to initiate reactions of mechanophore molecules.[167]

The design of the mechanoresponsive delivery system requires a tunable platform. Silica nanocapsules (SiNCs) are ideal as a delivery system for various applications [26] [40] [168] because their properties can be tuned by controlling their shape, size, shell thickness or chemical composition [169] [170] [41] and, consequently, are ideal candidates as mechanoresponsive carriers. Here, SiNCs are precisely manufactured with a controlled structure (Figure 4.1.1) to yield a class of tunable and controllable mechanoresponsive nanocarriers. In those SiNCs, a condensed silica shell of a tunable thickness encapsulated a liquid core of tunable size, acting either directly as the cargo or used to dissolve the cargo. These well-defined nanocapsules provide a blueprint to understand how to tune the structural parameters of the mechanoresponsive system to achieve the release required for specific applications and sets of mechanical stresses.

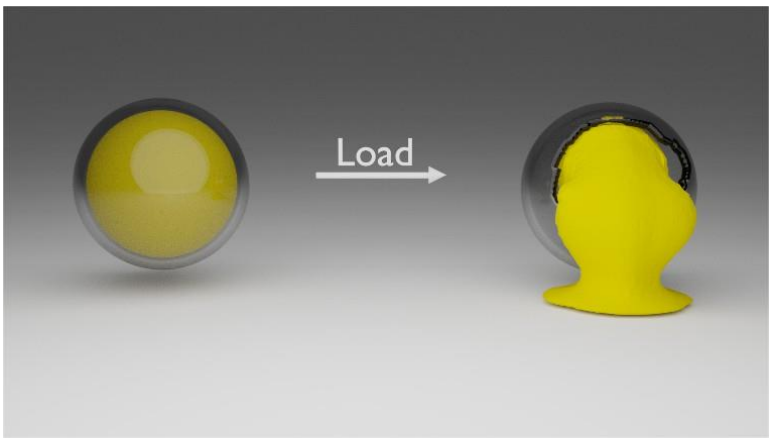

Figure 4.1.1: Mechanoresponsive release of encapsulated cargo by the fracture of the shell by a mechanical load.

4.1.2 Results and discussion

The tailored SiNCs were prepared via oil-in-water miniemulsion by dispersing a mixture of silica precursor and a specific hydrophobic cargo in an aqueous solution of surfactant. Nanodroplets formed by the microfluidization of the biphasic mixture acted as the template for the formation of the final SiNCs. By tuning the composition and size of the nanodroplets, it was possible to control the properties of the resulting SiNCs (Figure 4.1.2).

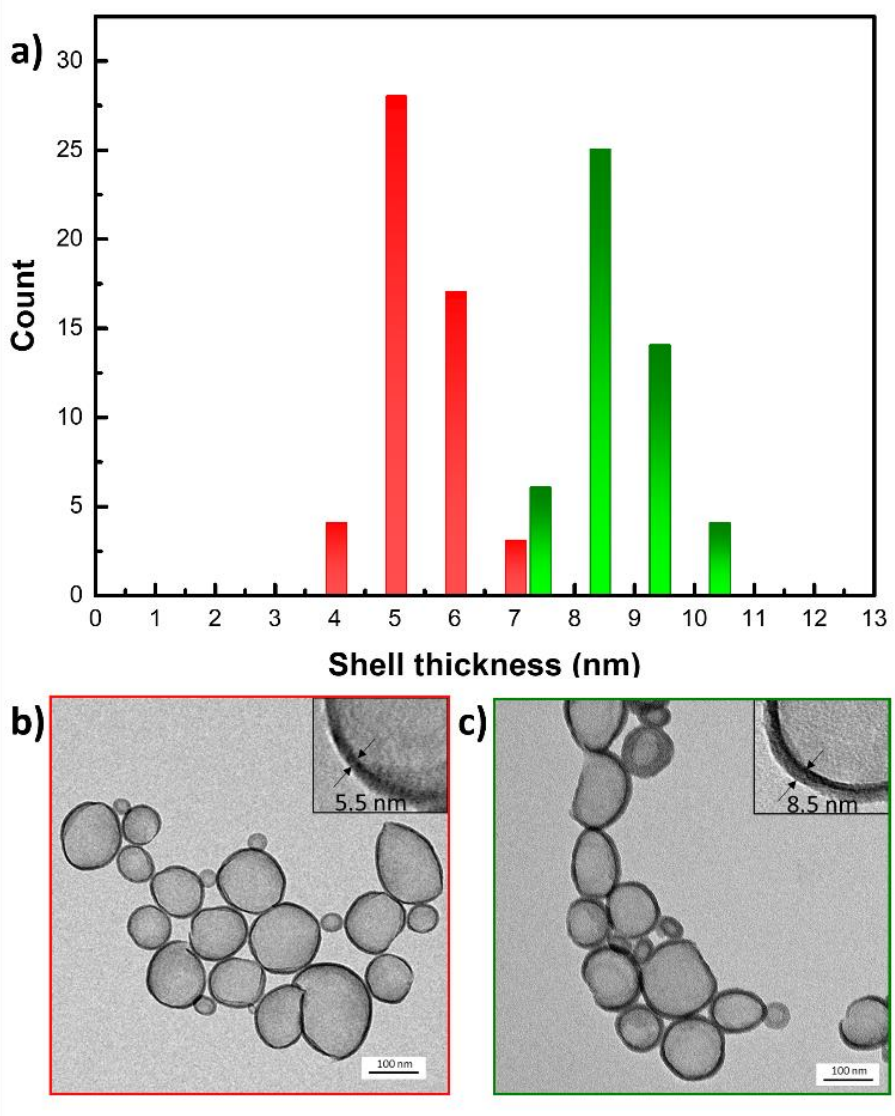

Figure 4.1.2: Synthesis of well-defined silica nanocapsules with an organic liquid core. a) Distribution of shell thickness for different samples with an average shell thickness of 5.5 nm (red) and 8.5 nm (green) (N>50). b, c) Representative TEM images of silica nanocapsules with 8.5 and 5.5 nm shell thickness analyzed in a.

The size of the SiNCs was controlled either by the ratio of dispersed to continuous phase used during microfluidization, the concentration of surfactant used in the continuous phase, or the intensity of the high mechanical stress generated during the microfluidization process (Figure 4.1.3a).[35]

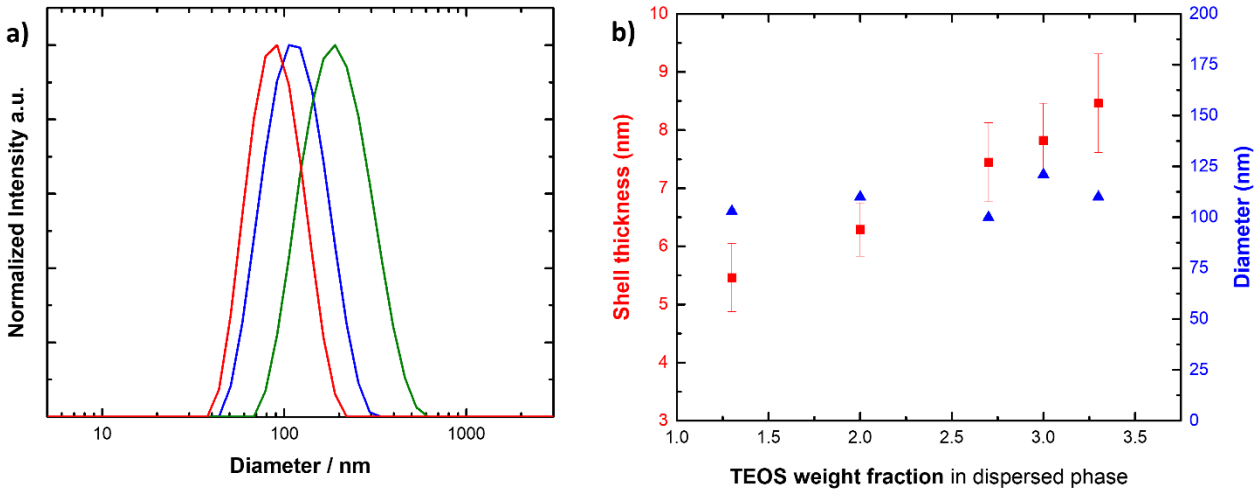

Figure 4.1.3: Control of the shell thickness for SiNCs of similar diameter by tuning the weight fraction of TEOS during miniemulsion.

After emulsification, the interfacial condensation reaction between the silica precursor tetraethylorthosilicate (TEOS) and water led to the formation of a solid silica shell around the core organic solvent and the SiNCs showed homogenous size, shell thickness and morphology (Figure 4.1.2). Furthermore, an increasing the weight fraction of TEOS relative to the organic core material (e.g. hexadecane, hexane, toluene, glycerol trioleate), the shell thickness increased (Figure 4.1.3b). The control of the synthetic condition allowed to generate a library of SiNCs of controlled size and shell thickness (Table 4.1.1).

Table 4.1.1: Overview of prepared samples.

Sample No.	TEOS (g)	HD (g)	Hexane (g)	Toluene (g)	Rhod. PEG (g)	Diameter (nm)	Shell thickness (nm)
1a	2	-	-	3	0.05	85	5.5
1b	3	-	-	3	0.05	110	7.4
1c	4	-	-	3	0.05	126	8.5
1d	4	-	-	3	0.05	177	8.5
2a	3	-	3	-	-	108	6.1
2b	4	-	3	-	-	109	7.0
2c	4	-	3	-	-	104	7.2
2d	5	-	3	-	-	114	8.2
3a	4	3	-	-	-	75	5.7
3b	4	3	-	-	-	103	5.5
3c	4	3	-	-	-	141	5.8
3d	6	3	-	-	-	110	6.3
3e	8	3	-	-	-	100	7.4
3f	9	3	-	-	-	121	7.8
3g	10	3	-	-	-	110	8.5
3h	10	3	-	-	-	164	8.5
3i	10	3	-	-	-	205	8.8

The mechanical properties of the resulting SiNCs were studied by atomic force microscopy (AFM) (Figure 4.1.4). The SiNCs were deposited on a glass substrate and imaged by AFM to identify single SiNCs. Subsequently, the cantilever was placed at the center of the SiNCs and used to compress the SiNCs with increasing force. The resulting force-distance curves were used to characterize the mechanical properties of the SiNCs (Figure 4.1.4e). The breaking of the silica shell resulted in an abrupt drop of the force exerted by the cantilever compressing the shell. This explicit behavior allowed for the determination of the force needed to break the SiNCs and of the maximal deformation of the SiNCs at the breaking point.

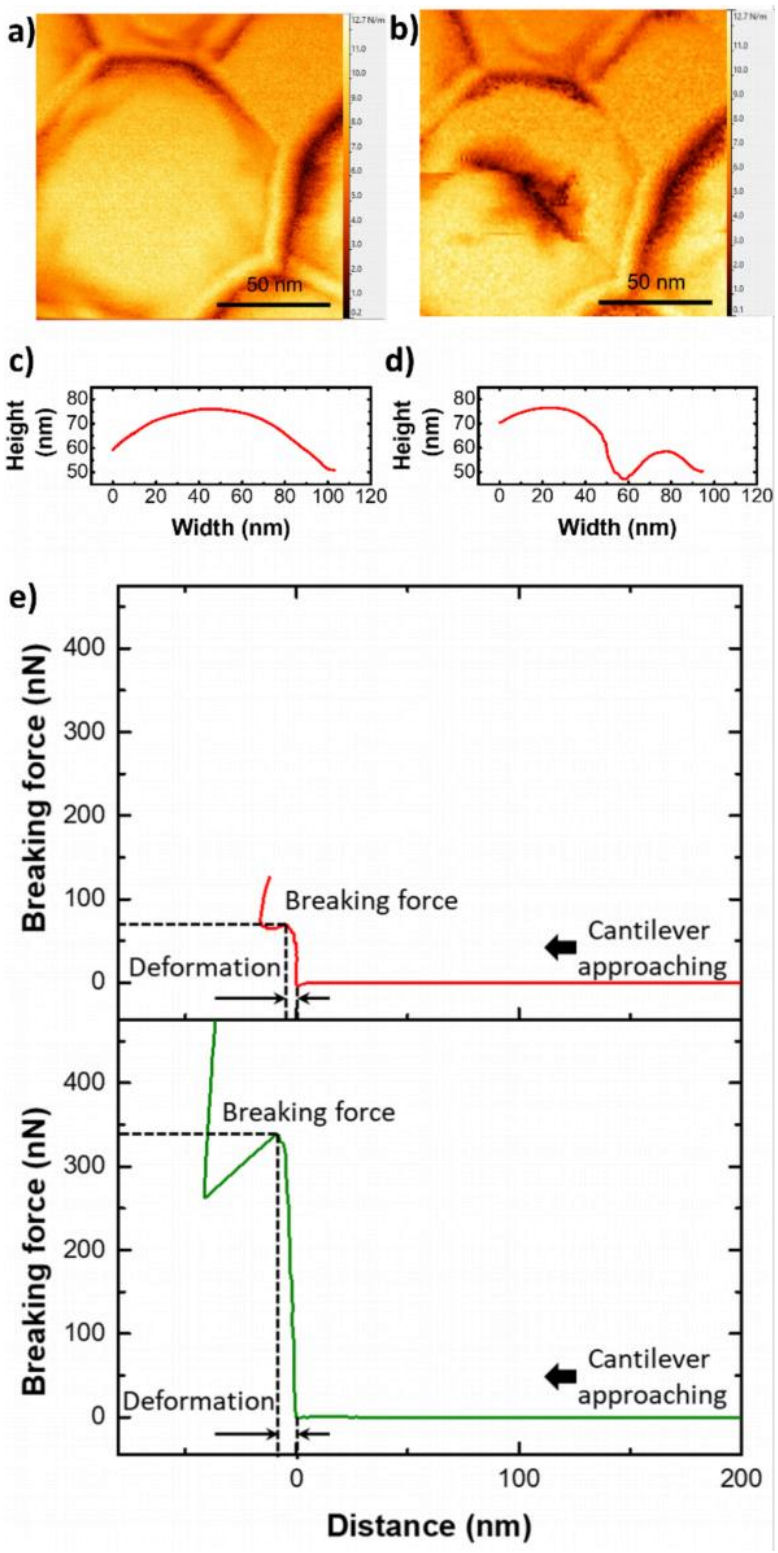

Figure 4.1.4: AFM force measurements of the indentation of single silica nanocapsules. a) AFM image of SiNC with an intact shell. b) AFM image of now visibly damaged silica shell after the application of a point load. c, d) respective height profiles of the intact and broken silica shell. e) Force-distance curve obtained from the compression experiment. Red: 5.5 nm shell SiNCs with low breaking force and green: 8.5 nm shell SiNC with high breaking force.

The deformation of the SiNC until breaking was defined by the distance covered by the cantilever between the jump-in contact when the AFM tip first made contact with the SiNC and the position of the tip when the shell ruptured. After the compression experiment, AFM imaging of the deformed SiNCs showed the resulting damaged silica shell (Figure 4.1.4a-d).

The compression curves (Figure 4.1.4e) can be used to measure the mechanical properties of the SiNCs and their relation to the morphology of the nanocapsules. In the early stage of the deformation generated by the compression of the SiNC by the AFM cantilever, the theory of thin shell elasticity can be used to describe the linear elastic response for the indentation of a homogeneous spherical shell. The force (*F*) applied by the cantilever results in an indentation depth (*Δc*) and this deformation is related to the capsule shell thickness (*h*), the diameter of the capsule (*D*) and the Young's modulus (*E*) of the shell material:

$$F \sim \frac{\frac{Eh^2}{\frac{D}{2}}}{} \Delta c \qquad (4.1.1)$$

This relationship has been used to quantify the mechanical properties of hollow microcapsule using AFM force measurements.[165] However, the thin shell elasticity theory is only valid when Δ*c* is in the range of the shell thickness *h* as larger deformations can result in plastic deformation.[171] In addition to the large deformation sustained by the SiNCs, the understanding of the deformation sustained by the SiNCs was made more complex since the shell was made of a solid material while the core contained a liquid. Assuming that the deformed capsule has an impermeable shell filled with an incompressible liquid, the displacement of the shell during deformation is constrained because the volume of the core must remain constant and results in additional restoring forces arising from the deformation and stretching of the shell needed to keep the volume constant. This force is proportional to the third power of the indentation depth:[172]

$$F \approx \frac{2\pi}{3} \frac{\frac{Eh}{(\frac{D}{2})^2}}{} \mathrm{E}(\Delta c)^3 \qquad (4.1.2)$$

We studied the deformation behavior and rupture of spherical shells under point loads. The deformation experiments were used to measure the mechanical stress, which can induce the large deformation needed to break the shell of the nanocapsules. When spherical shells are deformed exceeding the range of the shell thickness, nonlinear buckling resulting from the coupling of in-plane-stretching and out-of-plane bending occurs.[165] [173] In the SiNCs system, the force needed to generate

a plastic deformation that is large enough to induce the buckling of the shell, can be understood as the force needed to rupture the silica shell. For the compression of a spherical shell, the critical buckling pressure p_c is defined by:[174]

$$p_c = \frac{2E}{\sqrt{3(1-\nu^2)}} \frac{h^2}{(\frac{D}{2})^2} \quad (4.1.3)$$

where ν is the Poisson ratio.

The breaking force of SiNCs of constant diameter and increasing shell thicknesses (Figure 4.1.5) was determined by AFM indentation. For each shell thickness, a total of 10 SiNCs were compressed with the AFM cantilever tip with a force ranging from 0 to 500 nN. The SiNCs with a thin shell (h = 5.5 nm) broke with the application of a breaking force of ca. 95 nN and thicker SiNCs (h = 8.5 nm) broke after applying a force of ca. 213 nN. A general linear increase of the breaking force with increasing shell thickness was observed, in keeping with the increase in bending stiffness and extensional stiffness of the shell expected when the shell thickness increases.[165] [175] [176] [177] [178]

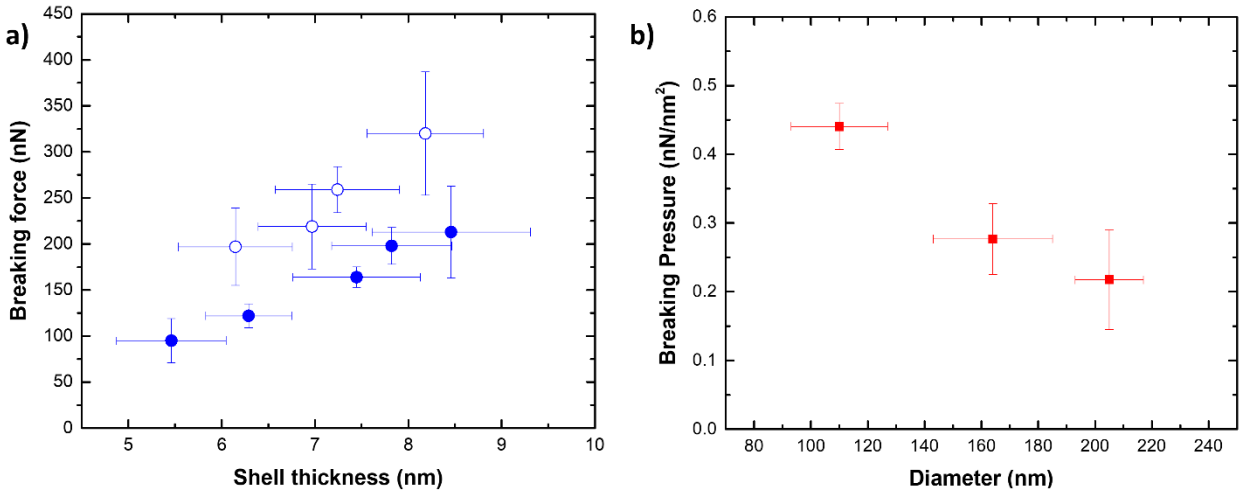

Figure 4.1.5: Mechanical properties of silica nanocapsules. a) Breaking force of SiNCs with different shell thickness for SiNCs of 110 nm diameter containing a liquid core (solid circle) or an empty core (empty circles). b) Breaking force of SiNCs with 8.5 nm shell as a function of the reduced deformation (Δc/D).

Interestingly, SiNCs filled with an incompressible liquid core broke after the application of a lower force when compared to the empty SiNCs. The SiNCs filled with a hexadecane core represent the case of a liquid core encapsulated by an impermeable shell. In comparison, the hollow SiNCs filled with air, prepared by the evaporation of a hexane core, which has a low boiling point solvent and high vapor pressure, had a compressible inner core (Figure 4.1.6).

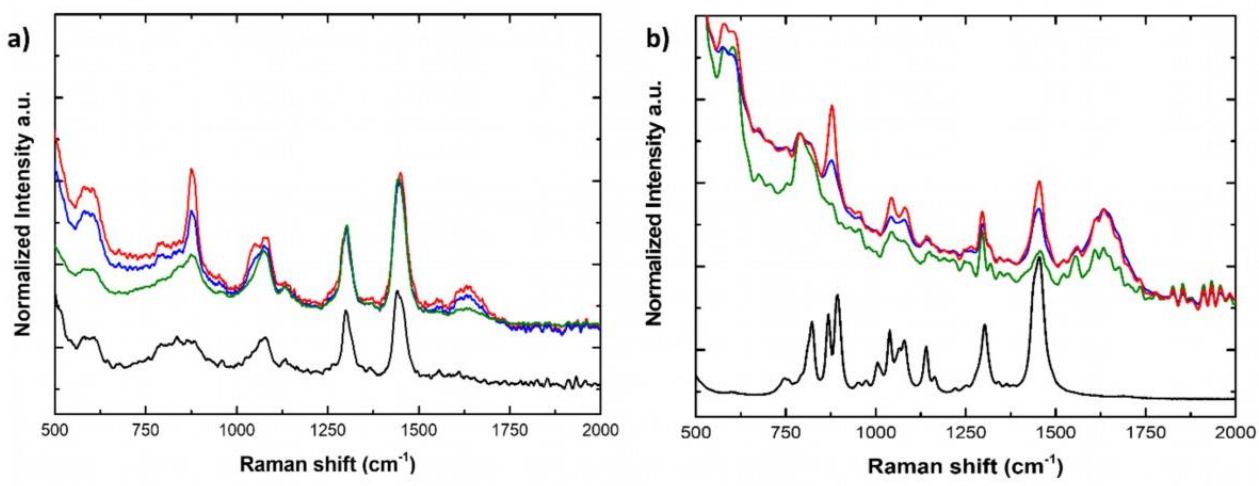

Figure 4.1.6: Raman spectra of SiNCs drying from an aqueous suspension. a) Raman spectrum of pure HD (black) and HD core SiNCs at different times during drying (red: 0 min; blue: 60 min; green: 120 min). b) Raman spectrum of pure hexane (black) and hexane core SiNCs at different times during drying (red: 0 min; blue: 60 min; green: 120 min).

Figure 4.1.5a shows that the force needed to break hollow SiNCs was 30-40% higher than for liquid core SiNCs. This difference in the breaking force originated from the presence of the incompressible liquid. In the case of filled SiNCs, the volume of the core must remain constant during the deformation experiment as the liquid core material cannot be compressed. As a result, additional restoring forces emerged, causing more stress on the silica shell and consequently leading to the breaking of the shell occurring at lower forces compared to hollow SiNCs.[179]

Additionally, the variation of the breaking force with the capsule size was studied for liquid-filled SiNCs. The results show that the highest breaking force was observed for thick and large SiNCs (h = 8.5 nm, D = 205 nm), while the lowest breaking force was observed for thin and small (h = 5.7 nm, D = 75 nm) SiNCs (Figure 4.1.7a). Typically, when capsules with a given shell thickness are considered, capsules with a small diameter are more robust than capsules with a larger diameter as $p_c \propto \frac{1}{(D)^2}$.[173] The results obtained by AFM show that the force needed to break the SiNCs also induced the deformation of the capsule and we observed that larger capsules were more deformed at the

breaking point than smaller SiNCs (Figure 4.1.7b). Consequently, the breaking force needed to be converted in a breaking pressure to analyze the results further. The critical breaking pressures were calculated using the Hertz contact mechanics to determine the contact area between the cantilever tip and the nanocapsule.[180] Therefore, the deformation of the SiNCs at the breaking point was needed to calculate the contact area. The average deformation for small SiNCs of 110 nm average diameter was found to be 23.4 nm which corresponded to a deformation of 21.3% of the capsule diameter. For medium SiNCs (164 nm) a deformation of 47.8 nm (29.1%) and for large SiNCs (194 nm) a deformation of 72.7 nm (37.5%) were observed, those deformation were used to calculate the respective breaking pressure (Figure 4.1.5b). The results show that the critical breaking pressure increased as the size of the SiNCs decreased.

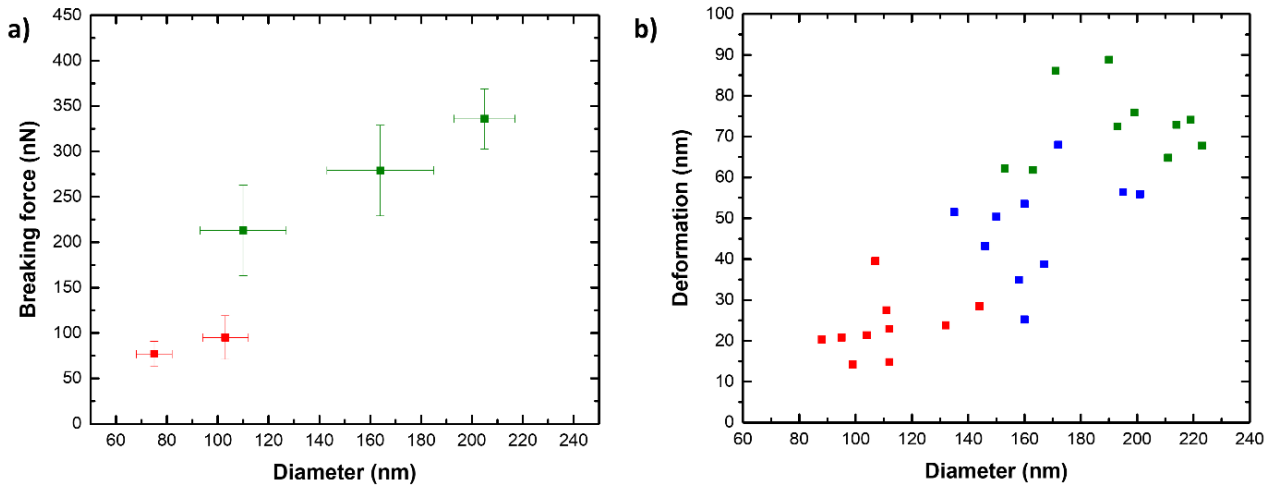

Figure 4.1.7: a) Breaking force for SiNCs with shell of 5.5 nm (red squares) and or 8.5 nm shell SiNCs (green square) and different diameter. b) Maximal deformation at the breaking point for SiNCs with different diameter (red=small diameter, blue=medium diameter, green=large diameter) and a shell thickness of 8.5 nm.

The AFM results showed the mechanical response of individual SiNCs. However, for release applications, probing a group of SiNCs simultaneously is essential. To do so, SiNCs containing a fluorescent cargo (rhodamine-labeled polyethylene glycol) were prepared. A large cargo was chosen to prevent any release occurring by mass transport through the silica shell. The rhodamine-labeled PEG used here, like other macromolecular payloads, can only be released if the shell of the SiNCs is disrupted. After drying the suspension of SiNCs containing the rhodamine-PEG, the SiNCs were compressed with controlled load and the fraction of the cargo released was measured. The mechanical properties of individual SiNCs can be correlated with the mechanoresponsive release

observed from a group of SiNCs of similar diameter and shell thickness than those used in the AFM experiments. The SiNCs were compressed with a hydraulic press using a die of 13 mm diameter loaded with 15 mg of dried SiNCs. All the compressed samples contained ca. $5 \cdot 10^{13}$ NCs. The hydraulic press allowed for the application of loads ranging from 2 to 10 t. This load equals an applied pressure of a similar magnitude as calculated in Figure 4.1.5b for the critical breaking pressure, and the application of such a load led to the breaking of the compressed SiNCs as visualized by TEM (Figure 4.1.8a inset). The analysis by microscopy clearly showed the fractured shells of SiNCs after the compression of the sample with the hydraulic press.

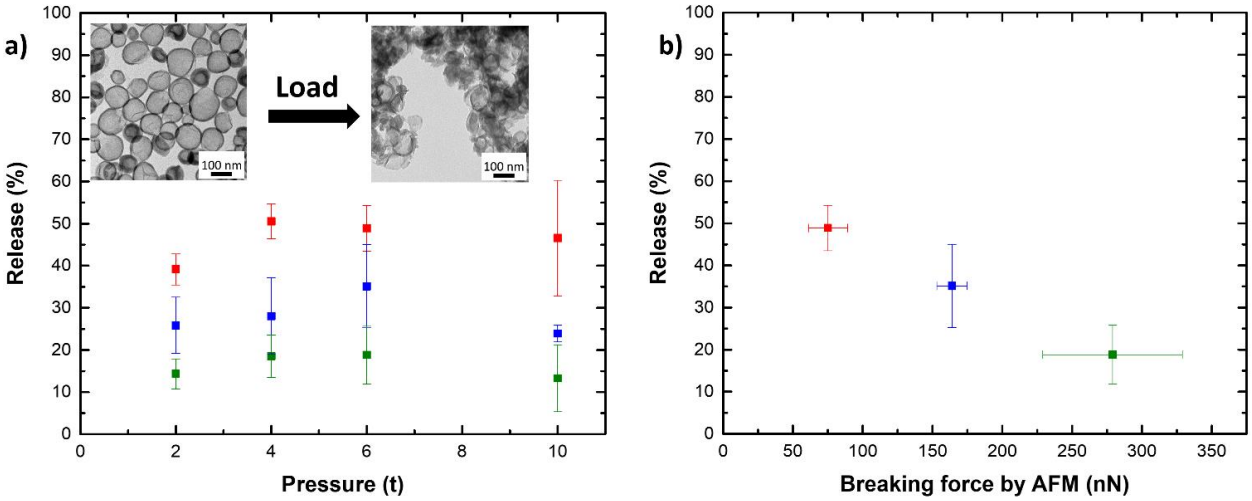

Figure 4.1.8: Mechanoresponsive release from SiNCs. a) Inset: TEM images of SiNCs before and after compression with a load of 10 t. Graph: Release profiles of 84 nm diameter SiNCs with 5.5 nm shell (red squares), 125 nm diameter SiNCs with 7.4 nm shell (blue squares) and 177 nm diameter SiNCs with 8.5 nm shell (green squares) under different applied loads. b) Release from SiNCs related to breaking forces determined by AFM measurements for SiNCs with similar shell thickness and capsule diameter

After the compression, the SiNCs were recovered and dispersed in an EtOH : H_2O mixture (1:1). During the redispersion, the dye contained in the broken SiNCs was extracted into the solvent mixture, and the quantification of the release was performed by measuring the fluorescence intensity of the rhodamine in solution. The mechanoresponsive release was studied for three different combinations of shell thickness and diameter either small SiNCs with a thin shell (h = 5.5 nm; D = 84 nm), medium SiNCs with an average shell thickness (h =7.5 nm; D = 125 nm), or large SiNCs with a thick shell (h = 8.5 nm; D = 177 nm). Every SiNCs sample was compressed for 30 s with a load ranging from 2 to 10 t (Figure 4.1.8a). The release of the cargo increased with the load applied until it reached a maximal value. Further compression led to an apparent decrease of the release, but this behavior was ascribed to the sintering of the SiNCs observed under compression with large loads,[181] [182]

reducing the redispersibility of the sample and the extraction of the payload from the broken capsules. In the case of small SiNCs with a thin shell a release of up to ca. 50% of the encapsulated cargo was observed. While lower maximal release of ca. 35 and 19% were observed for medium SiNCs with an average shell thickness and large SiNCs with a thick shell, respectively. The complete release of the payload was not observed due to the combination of the sintering of the SiNCs (Figure 4.1.9), the uneven force distribution through the compressed sample, and the distribution in size and thickness of the SiNCs leading to only a fraction of the SiNCs experiencing a force larger than the threshold pressure needed to break and release the payload. By correlating the maximum release observed for the different SiNCs with the respective breaking forces determined by AFM, the results clearly demonstrate that the tuning of the mechanoresponsive release from the SiNCs can be achieved by controlling the architecture of the SiNCs. The capsules with the lowest breaking force as measured by AFM released the largest amount of dye (Figure 4.1.8b), while the SiNCs with the highest breaking force released the lowest amount of dye, demonstrating the controlled mechanoresponsive release for SiNCs designed with different breaking resistance.

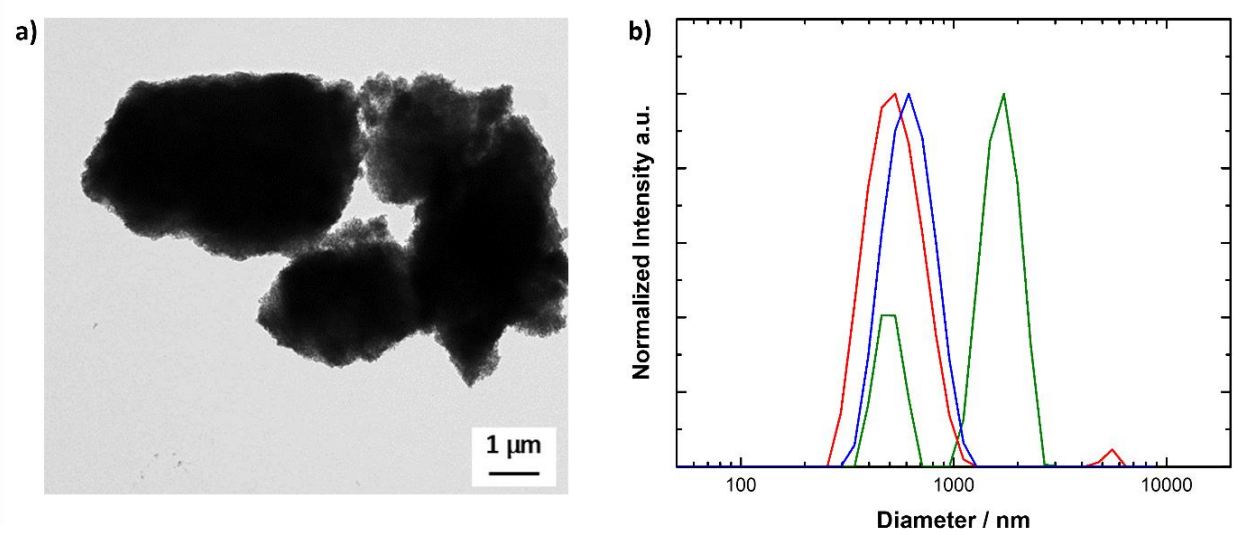

Figure 4.1.9: Redispersion of compressed SiNCs. a) TEM image of SiNCs without glucose compressed by 4 t. b) Dynamic light scattering measurement of redispersed SiNCs in EtOH:H_2O (1:1). No compression and no glucose (red), 4 t compression with glucose (blue), 4 t compression without glucose (green).

4.1.3 Conclusion

The successful preparation of silica nanocapsules (SiNCs) as a model system to study the mechanoresponsive release of molecules was shown. By controlling the architecture of the SiNCs (shell thickness and diameter), the force needed to break those nanocarriers was precisely tuned as determined using AFM force spectroscopy. The breaking force of individual capsules increased with both the shell thickness and the capsule diameter. Simultaneously, the maximal deformation of the SiNCs at the breaking point increased with increasing capsule diameter, indicating the importance of monodisperse size distribution to use such systems for the controlled release of payloads.

The resulting SiNCs were used to trigger the release of encapsulated payloads used mechanical stress. The mechanoresponsive release during the compression of dried SiNCs in a hydraulic press showed that the critical force needed to break individual SiNCs could be used to predict the release from different carriers. The SiNCs displayed excellent properties as mechanoresponsive nanocarriers since tuning the architecture of the nanocapsule, such as shell thickness or capsule diameter, led to a precisely controlled release. This approach has a vast potential for the development of smart lubricants as the release of encapsulated cargo can be tuned to control the friction in tribological contacts.

4.2 Glycerol-based polyurethane nanoparticles reduce friction and wear of lubricant formulations*

In the previous chapter, the encapsulation of hydrophobic molecules in SiNCs was discussed, demonstrating the great control over synthesis and mechanical properties of this innovative mechanoresponsive nanocarrier system. The successful mechanoresponsive release from SiNCs outlines the great potential of this nanocarrier in the field of tribology as a lubricant additive.

In this chapter, the encapsulation of hydrophilic glycerol into a nanocarrier system is presented. The addition of glycerol can improve the efficiency of the lubricant system. But the direct addition of hydrophilic molecules like glycerol to hydrophobic lubricant oils is challenging due to the poor miscibility. The encapsulation of hydrophilic additives in nanocarriers allows the design of additive systems where the nanocarriers enable the delivery such molecules to the lubricant. Here, the release of the additive from the nanocarriers dispersed in a lubricant oil, was triggered by the force applied by the surface/surface contact on the nanocarriers. The release observed was strongly dependent on the mechanical properties of the nanocarrier material, which could be controlled during the synthesis. The addition of those mechanoresponsive nanocarriers improved the long-term performance of the lubricant and represent a step toward the reduction of friction between metal-metal contacts.

4.2.1 Introduction

The energy consumption in our modern society are immense and require actions in dealing with the increasingly severe energy crisis.[2] Friction and wear between moving surface contribute to 23% of the total worldwide energy consumption.[1] The majority of this energy (20%) is consumed to overcome friction, and 3% is associated to wear-related failures. The development of new surfaces, materials or additive to reduce friction and wear would then have a major impact on the energy consumption.

Two interacting surfaces in relative motion creates a tribological pair. The friction, the force resisting the movement, of the tribological par is partially ascribed to the direct contact of the surface, which

*This chapter is based on the article: "Glycerol-based polyurethane nanoparticles reduce friction and wear of lubricant formulations" by F. Uebel, H. Thérien-Aubin and K. Landfester. To be submitted. Contributions: F.U., H.T.-A. designed the experiments. F.U. performed the experiments. F.U. and H.T.-A. analyzed the data. H.T.-A. and K.L. supervised the project.

can be enhanced by the presence of microscopic roughness. The addition of a lubricant, creates a lubricating film in the tribological system, which can separate the two interacting surfaces. This reduces the friction and makes the tribological contact more energy efficient.

Depending on the normal applied load at the contact, the sliding speed of the surfaces and the viscosity of the lubricant, different lubrication regimes can be reached (boundary, mixed, hydrodynamic).[140] While some contact between the surfaces occurs in boundary lubrication and only minute contacts between asperities in the mixed regime, the surfaces are fully separated by a lubricating film in the hydrodynamic lubrication regime. To optimize the general liquid lubricant rheology properties of the lubricant system, the minimization of hydrodynamic shear is one of the key approaches. This often means decreasing the lubricant viscosity to the lowest possible value, while still maintaining mixed or hydrodynamic lubrication to minimize direct contact of the surfaces. Another approach in reducing the friction in the tribological contact is the addition of friction modifying molecules in low concentrations such as organo-molybdenum compounds, functionalized polymers, nanoparticles or amphiphilic organic molecules.[65] The addition of friction modifiers leads to the formation of a monolayer at the metal-oil interface due to their amphiphilic character. The additional oriented and homogeneous layer of friction modifying molecules can reduce shear forces by interacting with the non-polar oil and the polar metal surface at the same time. In most lubricant systems, both strategies are used simultaneously.

One of the Achille's heel of lubricant systems is their deterioration over time during their service. This leads to important economic and environmental costs by creating the need to replace the lubricant system frequently. In addition to friction modifiers, other additives are used to extend the life of the lubricant system and additives such as antioxidants, corrosion inhibitors, anti-wear and anti-foam agents or viscosity index improvers, are widely used. The addition of new component to the lubricant oils is often limited by miscibility. For example, glycerol adheres to surface and creates a new interface of solid surface/glycerol film/lubricant oil, which allows for the reduction of shear forces by generating this low-shear-strength glycerol film.[12] [13] However, the addition of glycerol to non-polar hydrophobic lubricant oils is not possible due its poor miscibility. Therefore, glycerol is either used in aqueous lubricants[183] or in derivative forms, such as glycerol monooleate, in hydrophobic lubricant oils. However, the friction reducing effect of glycerol derivatives is limited, compared to pure glycerol.[12] [184] Consequently, the delivery of glycerol, and other hydrophilic friction modifying agents

to a hydrophobic oil could significantly reduce the friction in lubricated system by the formation of a film at the surface of the metal contact. However, in order to introduce enough glycerol in hydrophobic based oil, new delivery mechanisms need to be developed, like its encapsulation in responsive nanocapsules, to circumvent its poor miscibility.

Nanoparticles are an emerging class of lubricant additives.[5] [185] Their size allows them to enter into the contact region between the lubricated surfaces. At the contact, nanoparticles can influence the lubrication either through rolling, sliding or exfoliation, depending on the contact pressure at the tribological contact and the nanoparticle morphology.[186] In comparison with organic additives, many nanoparticle additives are thermally more stable and can operate at elevated temperatures, extending the lubricant systems temperature range of operation.[4] The combination of the intrinsic friction reducing properties of nanoparticles with the ability to encapsulate and release an additional friction modifying molecule inside nanocarriers will lead to the development of a novel class of lubricant additives able to control and extend the life cycle of the lubricant.

Mechanoresponsive release is an ideal approach to design smart-additives for lubrication. Mechanoresponsively triggered release from nanocarriers occurs under the influence of external forces and can be harnessed to release friction modifiers when the forces present in a tribological contact exceed a predetermined threshold. This approach will lead to the design of self-regulating systems, where increasing forces, e.g. due to the lubricant depletion, induces the release of fresh lubricating molecules from the nanocarriers, restoring the original low-friction properties.

Here, we establish the synthesis and characterization of mechanoresponsive nanocarrier additives able to release glycerol. First, the partial polyaddition of glycerol with a crosslinking agent yielded glycerol-based nanocarriers composed of a solid polyurethane network surrounding unreacted free glycerol. These nanocarriers were compatible with traditional hydrophobic lubricant system based on poly(α-olefin) and displayed a strong friction modifying effect in steel-steel contacts. This represents an elegant approach to deliver hydrophilic additives, like glycerol, in hydrophobic lubricant systems to control the tribological properties at a metal-metal contact.

4.2.2 Results and discussion

Figure 4.2.2 shows the synthesis of the glycerol nanocarriers (GlyNCs). The miniemulsion of nanometer-size glycerol nanodroplets in toluene, was prepared by microfluidization (Figure 4.2.1).[35] Then, a toluene soluble crosslinking agent, toluene diisocyanate (TDI) was added to the continuous phase. At the interface of the glycerol droplets and the continuous toluene phase, a polyaddition reaction between the alcohol groups of the glycerol and the isocyanate groups of the TDI resulted in the formation of a polyurethane network which trapped unreacted glycerol, as observed with other alcohol containing systems.[187] [188]

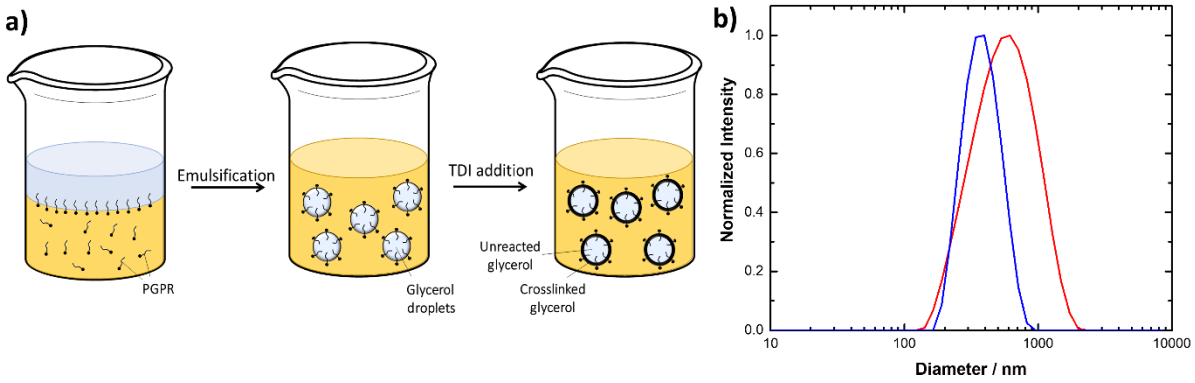

Figure 4.2.1: a) Miniemulsion procedure to obtain GlyNCs via inverse water-in-oil miniemulsion. b) DLS measurement of GlyNCs dispersed in toluene (red) and in PAO2 (blue).

The reaction led to the formation of spherical nanoparticles (Figure 4.2.2) and even though a large fraction of the glycerol remained unreacted (Figure 4.2.3, Figure 4.2.4), the formation of a core-shell structure, observed in other systems, was not observed here. The interfacial polymerization of precursor nanodroplets can yield different conformation of nanocarriers. Here, the morphology of the GlyNCs was studied by transmission electron microscopy (TEM). Figure 4.2.2c shows, that the as prepared GlyNCs appeared as spherical nanoparticles. However, due to the lack of contrast between glycerol and the glycerol-based polyurethane network the efficient differentiation between the carrier material (polyurethane network) and the payload (unreacted glycerol) was challenging. The transfer of the GlyNCs to water allowed to remove the unreacted glycerol, leaving only the polyurethane network. The TEM of the washed GlyNCs showed that the polyurethane network had a sponge-like morphology (Figure 4.2.2d). This morphology was likely obtained, because of the existence of no or little phase separation between the polyurethane network and the unreacted glycerol during the interfacial polymerization, and the partial miscibility of TDI in glycerol.

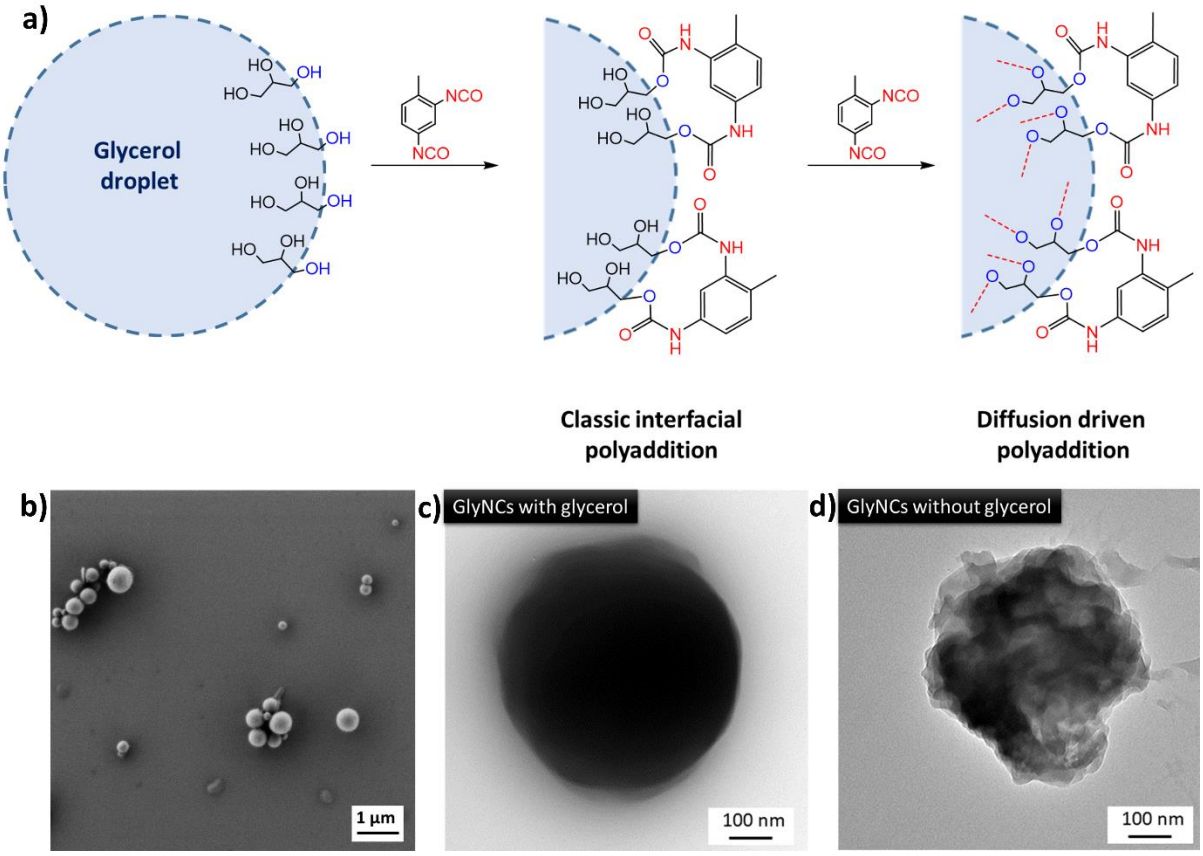

Figure 4.2.2: Synthesis of GlyNCs. a) Polyaddition reaction of glycerol droplets and 2,4-toluene diisocyanate. b) SEM images of GlyNCs. TEM image of GlyNC c) before the removal of the encapsulated free glycerol and d) after removal of the unreacted glycerol.

Controlling the amount of crosslinker, more specifically the ratio of isocyanate groups (NCO) to hydroxyl groups (OH), yielded GlyNCs with different compositions. The variation of the NCO:OH ratio from 0.625 to 1.25 resulted in an increase in the formation of the polyurethane network as determined by TGA analysis (Figure 4.2.3a), FTIR spectroscopy (Figure 4.2.3c), and NMR spectroscopy (Figure 4.2.4). The TGA curve showed a two-step degradation process for the GlyNCs containing free glycerol. The first degradation at ca. 225 °C corresponded to the degradation of free glycerol, and the second degradation starting at ca. 375 °C to the degradation of the polyurethane network. The relative weight loss of each degradation steps was used to determine the composition of GlyNCs with different NCO:OH ratios (Figure 4.2.3b). The GlyNCs were further analyzed by FTIR (Figure 4.2.3c). The formation of the urethane linkages during the polymerization lead to the apparition of new vibration mode at 1702 (C=O), 1532 (C-N) and 1228 cm^{-1} (O-C=O) (Figure 4.2.3b, inset). As the NCO:OH ratio increased, the number of urethane linkages increased, leading to an increase in the intensity of

the peaks associated with the urethane. Simultaneously, the peak associated with the vibration of the alcohol groups decreased (ca. 3300 cm^{-1}).

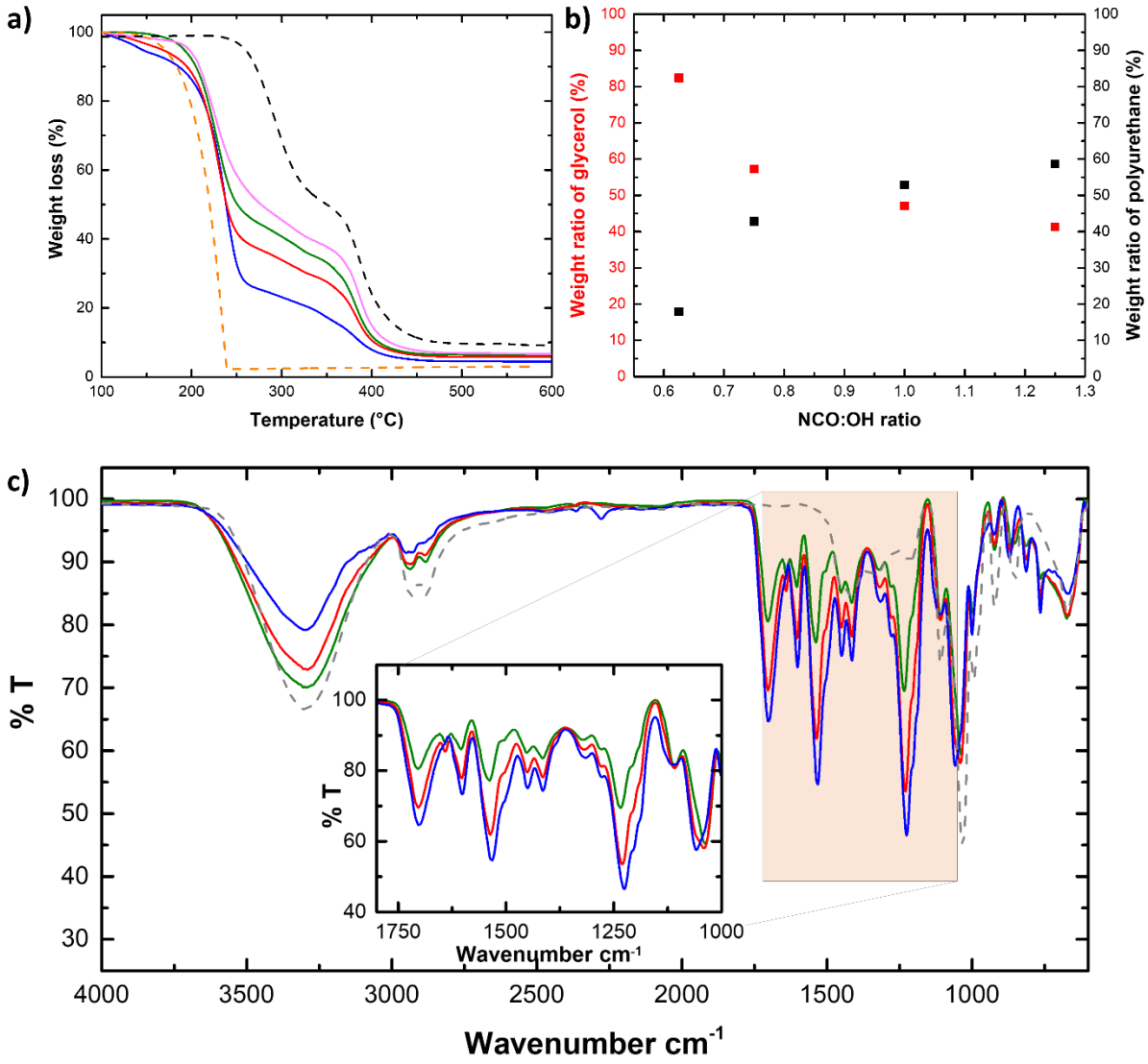

Figure 4.2.3: a) TGA decomposition analysis of GlyNCs with different NCO:OH (blue: 0.625; red: 0.75; green: 1.0; magenta: 1.25), pure glycerol (orange dots) and glycerol-free GlyNCs (black dots). b) Weight ratio of unreacted glycerol and formed polyurethane network of GlyNCs with different crosslinking ratios. c) FTIR spectra of GlyNCs with different NCO:OH ratio (blue: 0.64; red: 0.32; green: 0.16; grey dots: pure glycerol). Inset showing the formed polyurethane linkages from 1150 to 1750 cm^{-1}.

The GlyNCs were also analyzed by ^{13}C-NMR spectroscopy (Figure 4.2.4), revealing the presence of free unreacted glycerol and crosslinked glycerol which is part of the formed polyurethane network.

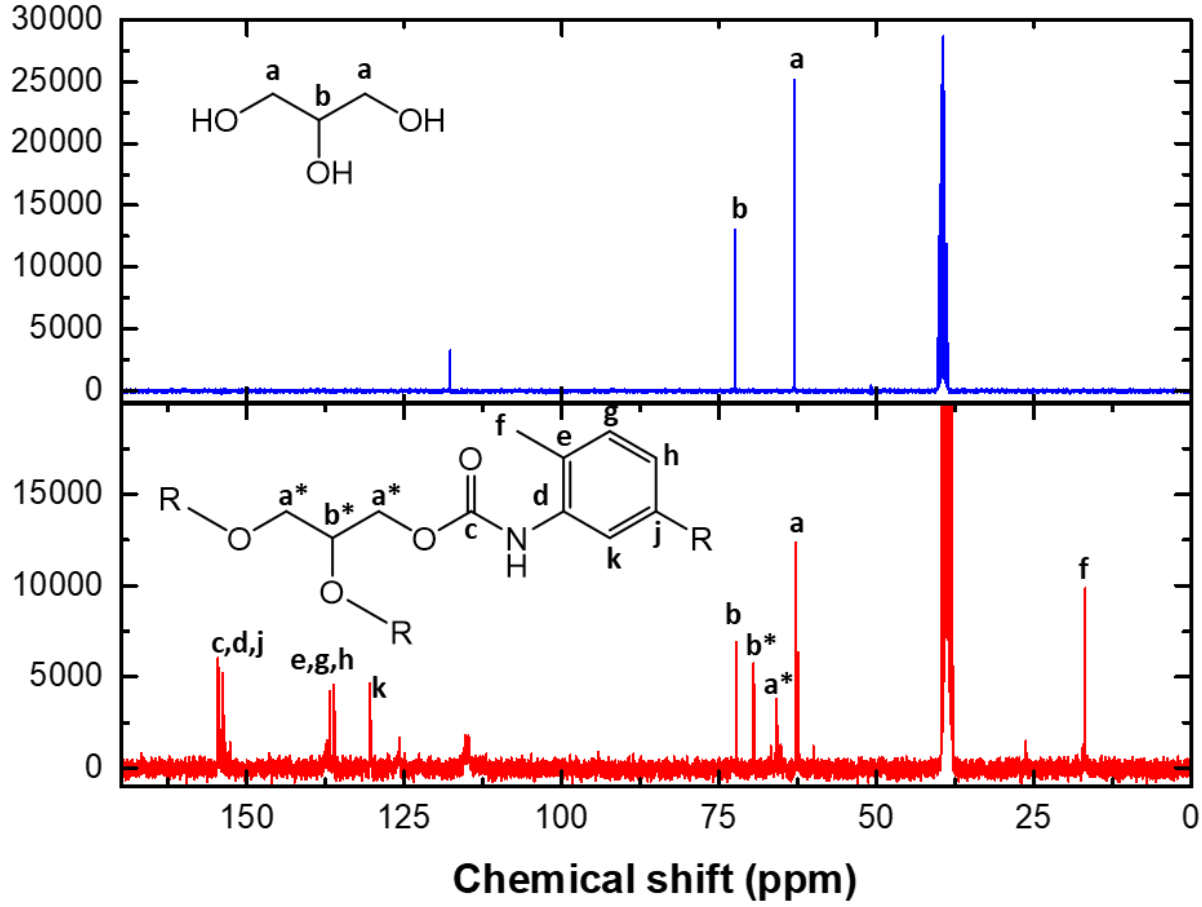

Figure 4.2.4: ^{13}C-NMR spectra of pure glycerol (blue) and glycerol nanocarriers (red) with a NCO:OH ratio of 1.25.

In turns, the composition of the GlyNCs influenced the mechanical properties of the nanocapsule. Atomic force microscopy (AFM) was used to measure the Young's modulus of GlyNCs with varying NCO:OH ratio (Figure 4.2.5). After casting a dilute suspension of GlyNCs on a glass slide, individual and isolated GlyNCs were imaged by AFM (Figure 4.2.5a) in quantitative imaging (QI) mode. QI mode allowed to record a force-displacement curve at each pixel of the image, which was used to calculate the Young's modulus of the GlyNCs by imaging a defined section of the GlyNC. Each GlyNCs displayed a narrow Gaussian distribution of Young's modulus (Figure 4.2.5b). The modulus of the GlyNCs increased from 231 to 851 MPa, when the ratio of NCO:OH increased from 0.625 to 1.25. Therefore, controlling the amount of crosslinker used during the synthesis allowed to modulate the Young's modulus of the resulting polyurethane network, thus regulating the mechanical properties of the GlyNCs.

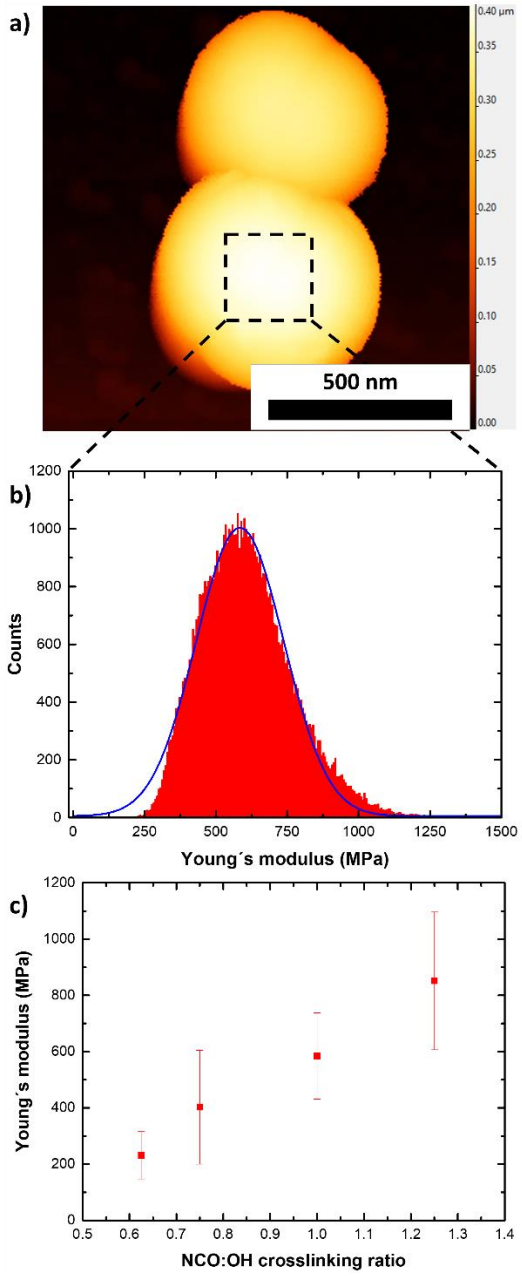

Figure 4.2.5: AFM studies of GlyNCs. a) AFM image of individual GlyNCs on a glass slide. b) Young's modulus of a GlyNC recorded on the marked area close the pole of the nanocarrier. c) Young's modulus of GlyNCs with different NCO:OH crosslinking ratios.

After the synthesis, the GlyNCs dispersed in toluene were redispersed the lubricant oil poly(α-olefin) (PAO2), and the GlyNCs fully preserved their colloidal stability and remained fully dispersed (Figure 4.2.1b). We studied the influence of the addition of GlyNCs to PAO2 on the tribological properties of a steel-steel contact in a ball-on-three-plates geometry (Figure 4.2.6a). During the tribological experiment the friction coefficient was recorded at different sliding speed over a specific number of cycles. The wear scars on the steel plate surfaces were analyzed after the experiment (Figure 4.2.6b and c).

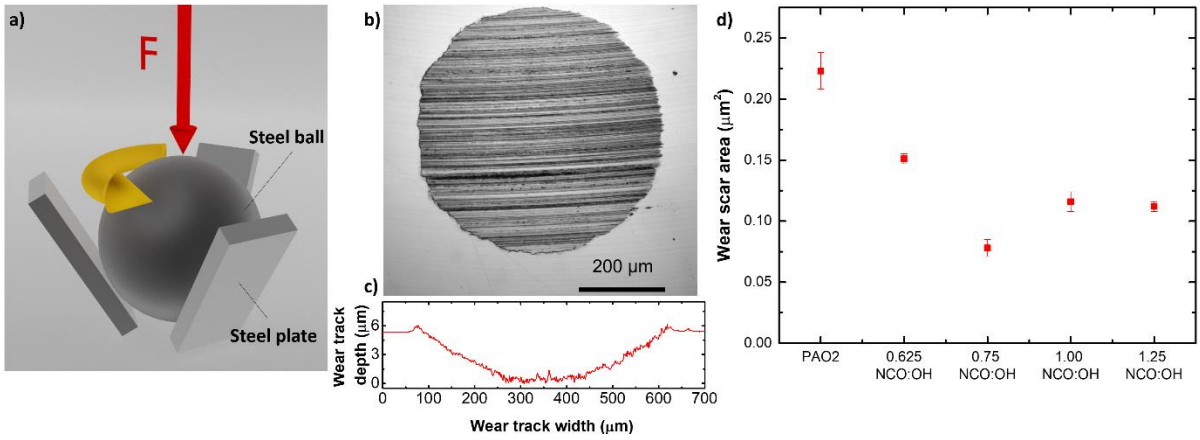

Figure 4.2.6: Tribological testing. a) Ball-on-three-plates geometry used for tribological measurements. b) Wear scar on a stainless steel plate as the result of a tribological measurement of pure PAO2 at 5 N over 25 cycles. c) Wear track profile of the wear scar from b. d) Wear scar areas obtained after 25 cycles at 5 N axial force for mixtures of just PAO2 and GlyNCs of different NCO:OH ratios in PAO at 5 wt% loading.

To ensure the acquisition of reproducible results, the steel plates used in the experiment were first polished to remove any preexisting irregularities (Figure 4.2.7).

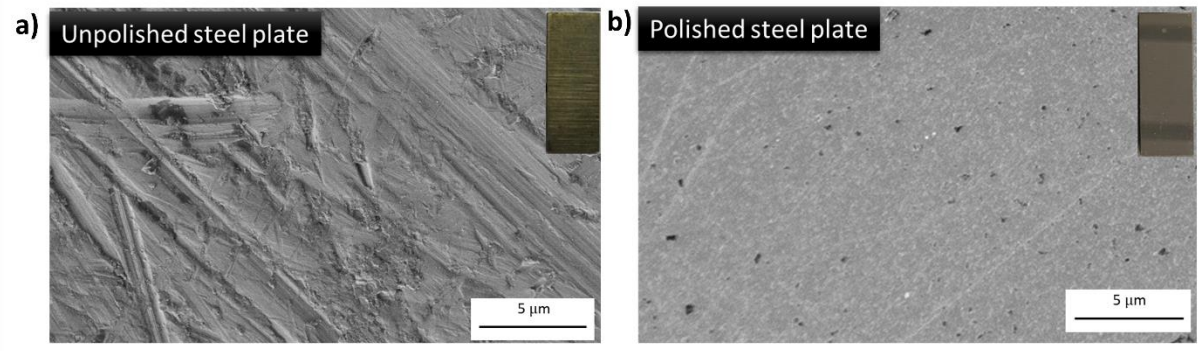

Figure 4.2.7: SEM images of stainless steel plates a) as received and b) after manual polishing.

During the tribological measurement, the steel ball was pressed on three steel plates with a known axial force *F*. At the same time, the steel ball was rotated at a known sliding speed. When ramping up the sliding speed from 0 to 135 mm/s, the coefficient of friction was recorded across different lubrication regimes (boundary-, mixed- and hydrodynamic lubrication), as defined by Stribeck (Figure 4.2.8a).[140] Figure 4.2.6d shows how the wear scars observed after the tribological experiments were influenced by the composition of the GlyNCs used as additive in PAO2. The observed wear scar areas reduced significantly in size by the addition of the GlyNCs to PAO2. Further, the effect of the GlyNCs was influenced by the chemical composition. The maximal reduction in wear occurred for the suspension of GlyNCs in PAO2 with the GlyNCs prepared at a NCO:OH ratio of 0.75, indicating a dual effect of the lubrication caused by the presence of spherical nanoobject in suspensions and the release of glycerol in the tribological contact. Typically, the wear track depth, measured by optical topography, varied between 1 and 6 µm depending on the lubricant system used.

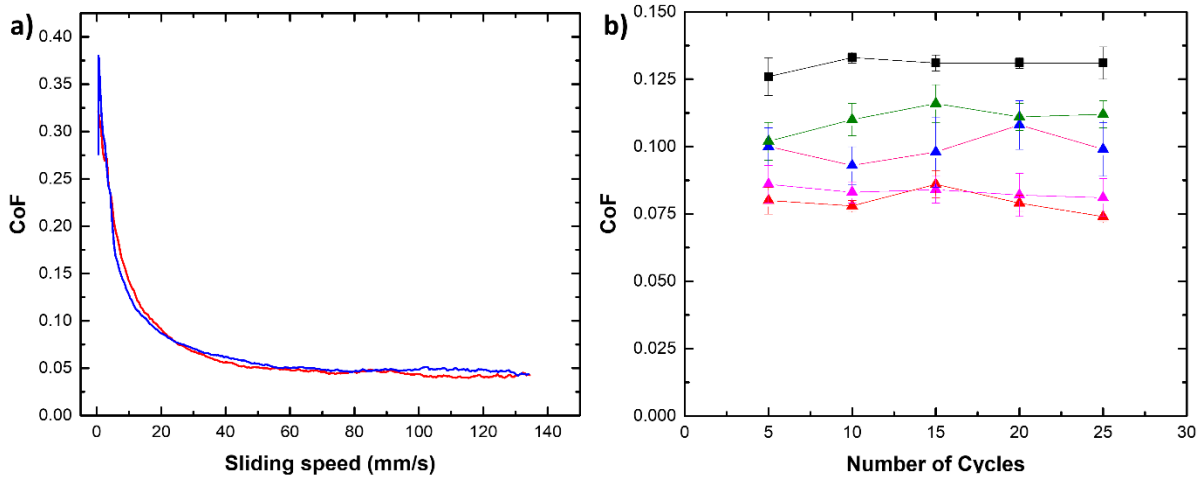

Figure 4.2.8: a) Coefficient of friction for one measurement cycle of increasing sliding speed (red) and decreasing sliding speed (blue). b) Coefficient of friction measured over 25 cycles for pure PAO2 (black squares) and 5 wt% of GlyNCs in PAO2 with different NCO:OH crosslinking ratios (blue: 0.625; red: 0.75; magenta: 1.00; green: 1.25).

In addition to reducing wear at the tribological contact, the GlyNCs also influenced the coefficient of friction in the system. Therefore, we studied the friction reducing properties of GlyNCs in PAO2 at different axial forces from 1 to 15 N, to see the effect of load on the lubrication (Figure 4.2.9a). The lowest coefficient of friction (CoF) was observed for the highest applied load of 15 N, while a significant reduction of the CoF was already observed for 5 N. In comparison, the results obtained for pure PAO2 at the same axial loads and cycle number, showed remarkably higher friction.

Additionally, the effect of the concentration of GlyNC on the tribological properties of the lubricant system was analyzed (Figure 4.2.9b). As the concentration of nanoparticles in suspension increase, the viscosity of the oil increases,[189] which could have a negative effect of the lubrication of the tribological contact. While the CoF decreased minimally with the addition of 1 wt% of GlyNCs in PAO2, the CoF drastically decreased with the addition of 5wt% of GlyNCs, and was the moderately lower for the PAO2 containing 15 wt% of GlyNCs. This reduction in friction clearly shows the outstanding ability of GlyNCs as friction reducing additives in lubricant oils.

The effect of the GlyNCs on the lubrication of the metal/metal contact was also influenced by the crosslinking degree of the GlyNCs. GlyNCs prepared with varying NCO:OH ratio were redispersed in PAO2 at a concentration of 5wt% and the effect of those lubricating systems was analyzed at different axial forces (Figure 4.2.9c). Independently from the crosslinking ratio, higher axial loads always showed lower CoF, with the 0.75 NCO:OH ratio giving the lowest overall values. Already, this crosslinking ratio showed the strongest wear-reducing effect as demonstrated in Figure 4.2.6d. Interestingly, the 1.0 NCO:OH ratio resulted in very similar friction for all measured forces, with an especially low CoF for 1 N axial force compared to all other crosslinking ratios.

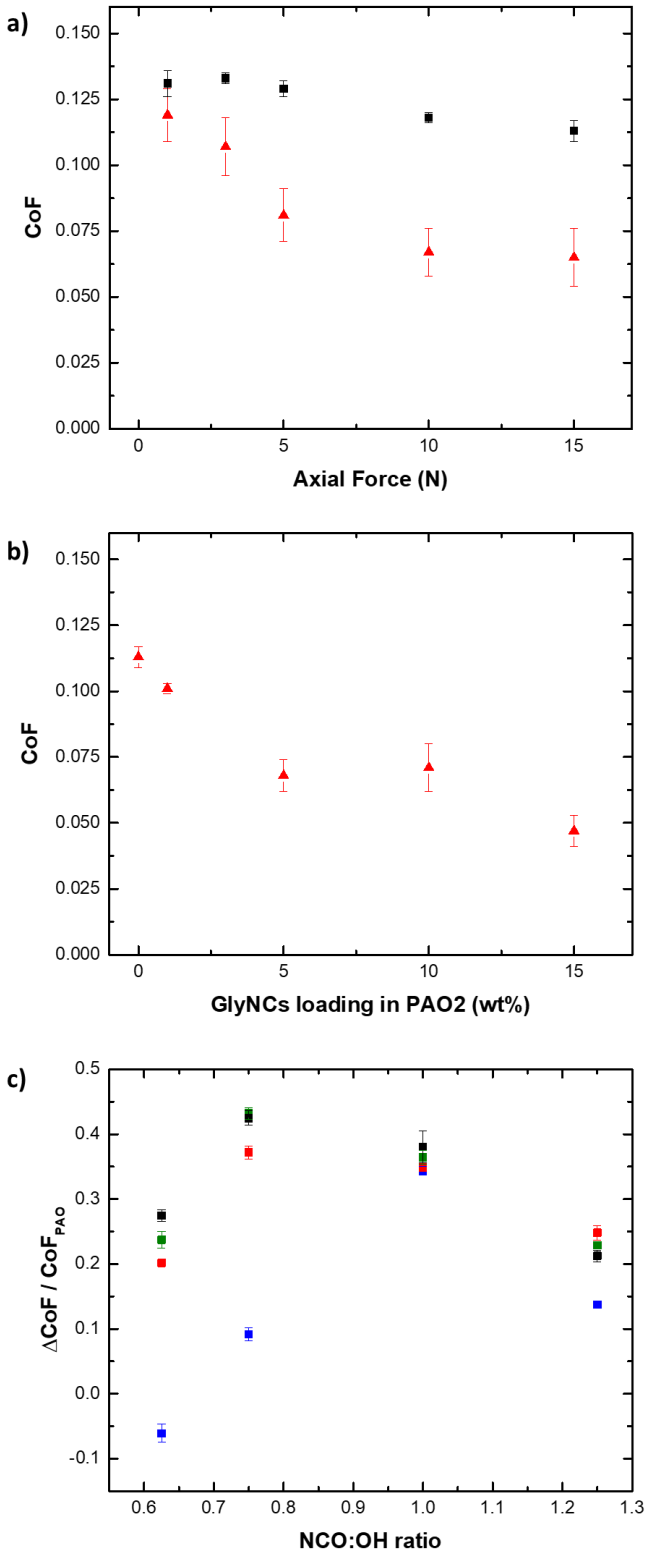

Figure 4.2.9: Tribological measurements. a) Coefficient of friction for pure PAO (black squares) and 5 wt% GlyNCs of 0.75=NCO:OH (red triangles) measured at different axial forces. b) Coefficient of friction of GlyNCs (0.75=NCO:OH) with different concentration in PAO2 measured at 15 N axial force. c) Relative coefficient of friction of GlyNCs with different NCO:OH crosslinking ratio in PAO2 at 5 wt% loading and at different axial forces (blue: 1 N; red: 5 N; green: 10 N; black: 15 N).

XPS measurements were performed on the surface of the steel plates after tribological measurements. The XPS spectrum recorded outside the wear scar area (Figure 4.2.10a, blue) showed the presence of non-aromatic C-C bonds (285.3 eV) and salt-based impurities (291.9 eV). Inside the wear scar area additional signals of aromatic C-C (284.5 eV), C-O-C (286.3 eV) and O-C-N (289.5 eV) were found, clearly indicating that the GlyNCs, crosslinked with aromatic TDI, have entered the tribological contact during the tribological measurement (Figure 4.2.10a, red).

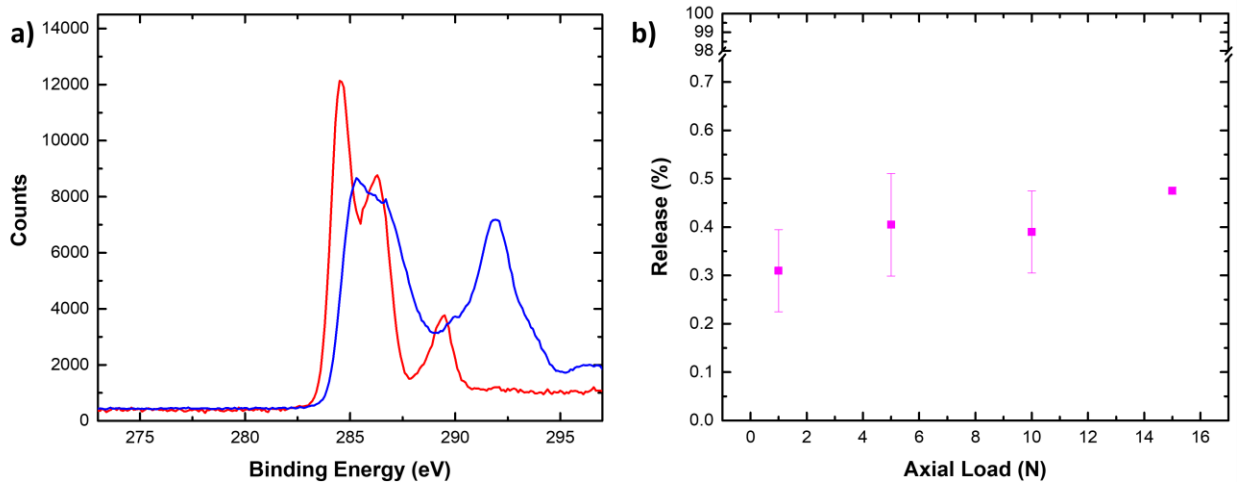

Figure 4.2.10: a) EDX measurement of metal surface after tribological measurement: At the wear scar area (red) outside the wear scar area (blue). b) Release of glycerol from GlyNCs of 1.0 NCO:OH ratio into the surrounding PAO after 25 cycles at different axial loads.

The release of free glycerol from GlyNCs was quantified using HPLC (Figure 4.2.10b). After the tribological measurement, the entire suspension of GlyNCs in PAO2 was collected. The samples analyzed here, were collected for experiments where 25 cycles of measurements were performed. After separating the GlyNCs from PAO2 by filtration, the released glycerol was extracted from PAO2 with an acetonitrile-water mixture. This mixture was sent through a suitable HPLC column to quantify the amount of released glycerol from the GlyNCs. By previously dissolving known amounts of glycerol in the acetonitrile-water mixture a calibration curve was obtained (Figure 4.2.11).

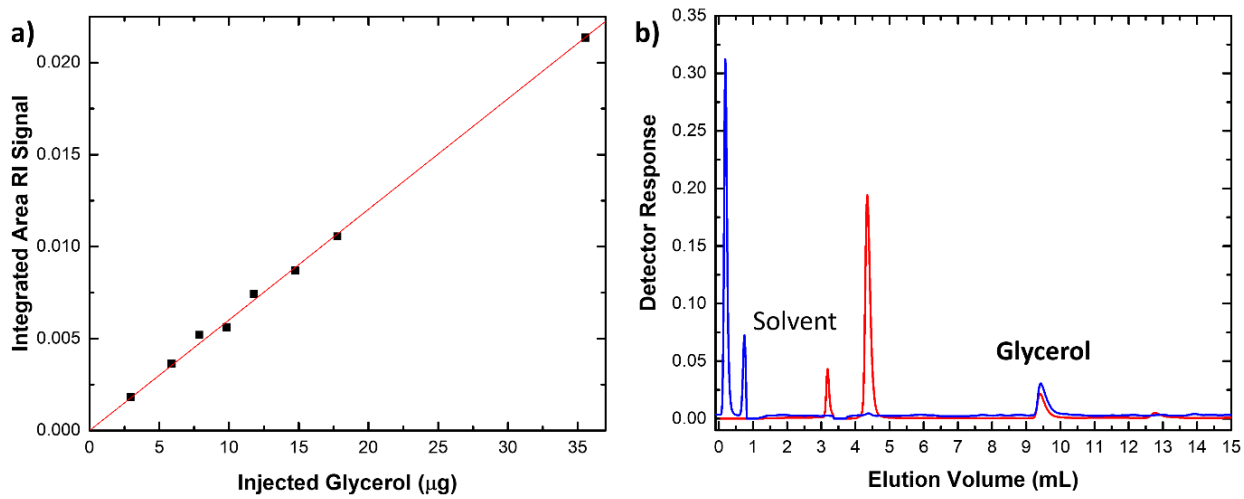

Figure 4.2.11: Standard calibration curve of pure glycerol dissolved in an acetonitrile-water (95:5) mixture.

GlyNCs applied as additive can affect the friction in a tribological contact in two manners: By the friction reducing properties of the nanocarrier itself and by the release of encapsulated glycerol, which adheres to the polar metal surface. The application of external loads in the tribological contact can promote the mechanoresponsive release from the GlyNCs and thus a reduction of friction is expected. As Figure 4.2.10b shows, the amount of released glycerol increased with increasing axial loads applied in the tribological contact. Therefore, the lower friction observed for higher loads compared to smaller loads (Figure 4.2.9a, c) originates from the presence of more glycerol released from the GlyNCs. At the same time, the percentage of released glycerol is of comparable order for all tested axial loads, but at higher loads a significantly lower friction coefficient was measured. Therefore, the observed lubricating effect at higher forces can also be ascribed to the presence of the GlyNCs themselves. In any case, it could be shown that glycerol was released in larger quantities when higher loads were applied. With regard to the GlyNCs being able to control the tribological properties long term, the slow and limited release observed after 25 cycles underlines their potential as supportive lubricant additive.

4.2.3 Conclusion

We demonstrated the synthesis of glycerol-based nanocarriers by the reaction between glycerol nanodroplets and a crosslinking agent, the partial polymerization of the glycerol led to the formation of sponge-like nanocarriers swollen with unreacted glycerol. The control over the composition of the nanocarriers also allowed for the control of the mechanical properties of the nanocarriers. The Young's modulus of the nanocarriers was measured for different chemical compositions and the stiffness of the nanocarriers increased with increased amount of crosslinker used during the synthesis. Those nanocarriers were redispersed in poly(α-olefin) to create smart lubricant systems. The tribological studies of these lubricant systems in a ball-on-plates geometry showed a strong influence of the glycerol nanocarriers on the behavior of the system. Systematically, the addition of the glycerol nanocarrier to the lubricant system resulted in a decrease in wear and friction in the tribological contact. In the presence of this innovative lubricant additive, we observed as reduction in friction up to 58% and in wear by 65% compared to pure lubricant. Ultimately, we showed the combined effect of the release of glycerol and the presence of nanoobjects in the tribological contact led to the control of the tribological properties of the system.

4.3 Polysulfur nanoparticles by miniemulsion polymerization*

In the previous chapter, the synthesis of glycerol nanocarriers which can be applied as lubricant additive was presented. The encapsulation and release of the hydrophilic glycerol allowed to reduce friction significantly compared to pure lubricant oil. Besides glycerol, also sulfur and sulfur components are widely used in various lubricant formulations. One of the most common application of sulfur-based materials is their use as antioxidants. Numerous types of organosulfur compounds as dialkyl sulfides, diaryl sulfides, polysulfides, modified thiols, thiophene derivatives, thioglycols and many others are used as peroxide decomposers, converting hydroperoxides into non-radical products in order to prevent chain propagation reactions.[3] Besides, the group of ashless dithiophosphoric acid derivatives shows great antiwear properties.[156]

Also elemental sulfur is added to mineral oils to improve the extreme pressure (EP) properties by reducing wear associated with welding of moving parts. Oil-soluble sulfur carriers of the general formula (R-S_x-R) offer better control over the reactivity of sulfur. The mechanism of polar sulfur carriers adsorbing to metal surfaces under EP conditions, which was discussed in 2.3.2.2, is the main protection against welding by controlled wear through the removal of slideable sulfur layers.

By developing sulfur nanoparticles with high sulfur content, a new class of sulfur additives can be developed. The known friction reducing properties of nanoparticles can thereby be combined with the wear protective properties of sulfur itself. In this chapter, the synthesis of sulfur nanoparticles via inverse vulcanization under miniemulsion conditions at elevated temperature is presented. Detailed analysis of the polymerization mechanism characterizes nicely the high molecular weight poly sulfur nanoparticles. Further, the poly sulfur NPs exhibit facile processability as they are obtained in an aqueous suspension, allowing e.g. simple film formation by drop casting.

*This chapter is based on the article: "Polysulfur nanoparticles by miniemulsion polymerization" by F. Uebel, M. Remmers and H. Thérien-Aubin, To be submitted. Contributions: H.T.-A. and F.U. designed the experiments. F.U. and M.R. performed the experiments. F.U. and H.T.-A. analyzed the data. H.T.-A. supervised the project.

4.3.1 Introduction

Elemental sulfur is a versatile material with interesting intrinsic properties, making sulfur components attractive for electrochemical, optical and agricultural applications. Sulfur is produced as a side-product of oil refining,[14] but few transformation route exist for this raw material, resulting in the production of millions of ton excess of sulfur annually.[15] Consequently, developing new valorization routes, by developing new sulfur-rich composite materials, for this underused feedstock is essential. However, due to the limited processability and solubility of elemental sulfur,[190] this remains a challenge. The inclusion of elemental sulfur in polymer materials could be an avenue to process and utilize this resource in the design of new functional materials. Here we leverage the benefits of a polymerization in dispersed media to produce sulfur rich polymer nanoparticles and show the properties of the resulting polymers.

Elemental sulfur is an interesting material, in addition to its temperature-dependent phases,[191] it possesses a complex electrochemistry,[192] [193] interesting optical properties and superior mercury capture ability.[194] The electrochemistry of elemental sulfur exhibits an intrinsically low electrical conductivity[195] and thus limited cyclability, however the high specific capacity value and outstanding energy density of sulfur in combination with for example lithium in Li-S batteries underlines the great potential of this novel battery type.[193] The optical applications of sulfur-rich materials rely on their high refractive index,[196] which enables their use in the design of IR optical materials.[197] Furthermore, sulfur is known as one of the most active sites for mercury adsorption,[198] making sulfur-rich materials attractive for mercury filtration and water reclamation.[199] Additionally, fertilizers containing fine powders of elemental sulfur, sulfates or a combination of elemental sulfur and sulfates are used as nontoxic green pesticides in agriculture, trying to replace more toxic conventional pesticides.[200] [201] Finally, the low activation energy required to form and break the S-S bond yield the potential to design self-healing and reconfigurable materials through the reshuffling of those dynamic covalent bonds.[202] [203] [204] [205]

The polymerization of sulfur is a potential strategy to improve the processability of underused sulfur feedstock.[15] [206] Elemental sulfur is usually found as a cyclic molecule (S_8) composed of 8 atoms and when heated above to ca. 159 °C the homolytic ring-opening of the S_8 form a diradical which can self-initiated radical polymerization of sulfur into polysulfur.[206] [207] [208] Yet, pure polysulfur has a limited stability resulting in its rapid depolymerization. Copolymerization has been a successful approach to

stabilize sulfur-rich polymers.[15] [209] [210] However, the resulting copolymers are often heavily crosslinked, have a low molecular weight or a limited loading of sulfur. Inverse vulcanization, a technique where the sulfur chains are stabilized by the addition of -ene containing monomers, has been particularly successful to produce a variety of sulfur-rich copolymers.[15] While the polymerization usually occur in bulk at elevated temperature where S_8 forms diradicals, the use different additives during the reaction can promote the polymerization at lower temperature, enabling the use of a broader range of comonomers.[211] [212] The resulting polymers have shown attractive properties enabling a wealth of applications from IR lens to cathodic material for Li-S batteries.[213] [214] [215] However, those copolymers, especially at high sulfur loading, remain poorly soluble,[216] [217] and difficult to process, although the dynamic nature of the S-S covalent bound can be harnessed for their processing.[218]

Here, to address the limited processability of such sulfur-rich polymer materials, polysulfur latexes were prepared from elemental sulfur in miniemulsion. The resulting polysulfur nanoparticles (polySNPs) were obtained in a colloidally stable suspension in glycerol, allowing for their transfer to water-based formulations and enabling their processing for film casting or as moldable powder. The polySNPs were easily processable and displayed attractive physicochemical properties, and will accelerate and promote the use of such sulfur-rich polymers in the design of functional materials.

4.3.2 Results and discussion

The synthesis of the polySNPs was carried out in dispersed media under different conditions. In every case, the elemental sulfur was first molten at 130 °C and subsequently combined with the appropriate mixture of comonomer, initiator or polymerization activator. Then, the liquid sulfur phase was combined with glycerol containing surfactants acting as an immiscible continuous phase. The biphasic mixture was emulsified by ultrasonication to obtain a miniemulsion of sulfur and comonomer nanodroplets dispersed in glycerol. The droplets were the locus of the polymerization reaction, and every nanodroplet was converted into solid polysulfur nanoparticles (Figure 4.3.1). The polymerization of the nanodroplets was carried either at 180°C in absence of initiator or activator or at 130 °C in the presence of traditional polymerization initiator or in the presence of *N*-methylimidazole (NMI). The size of the resulting polySNPs was influenced mostly by the choice of surfactant used to stabilize the nanodroplets and the comonomers used in the polymerization reaction. The effect of the surfactant was also influenced by the temperature, since the polymerization in the nanodroplet was carried out in absence of an osmotic pressure agent traditionally used to prevent the Ostwald ripening of the monomer droplets,[219] and can be held responsible for the size dispersity observed in those samples (Figure 4.3.2a).

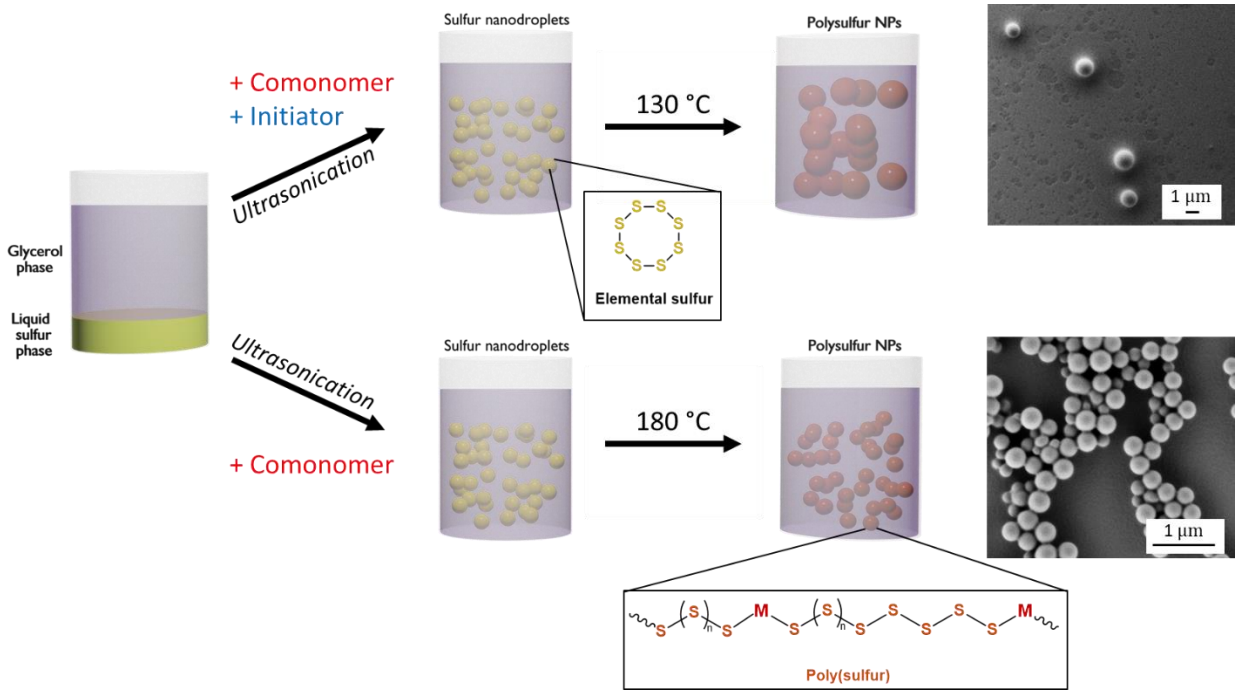

Figure 4.3.1: Synthesis of polysulfur nanoparticles. a) Synthesis of polysulfur NPs by miniemulsion approach at elevated temperature. b) Reaction mechanism for the inverse vulcanization of S_8 at 180 °C without initiation and at 130 °C with nucleophilic activation or radical initiation. c) Detailed mechanism for the nucleophilic activation of S_8 by *N*-methylimidazole (NMI).

In the cases where the polymerization reaction was carried out at 180 °C, the homolytic scission of the S_8 molecules led to the formation a diradical able to self-initiate the reaction. The reaction was performed in presence of different comonomer and the degree of conversion of sulfur was quantified by differential scanning calorimetry (DSC) from the fusion enthalpy of S_8 measured (Figure 4.3.2b). The conversion of sulfur was measured ex-situ as it was not possible to distinguish between unreacted S_8 and S_8 formed by the depolymerization of the sulfur-rich polymer after the reaction. However, in every case where the S_8 was copolymerized, high degrees of conversion were observed in the polymer obtained by miniemulsion (Figure 4.3.2b, Table 4.3.1).

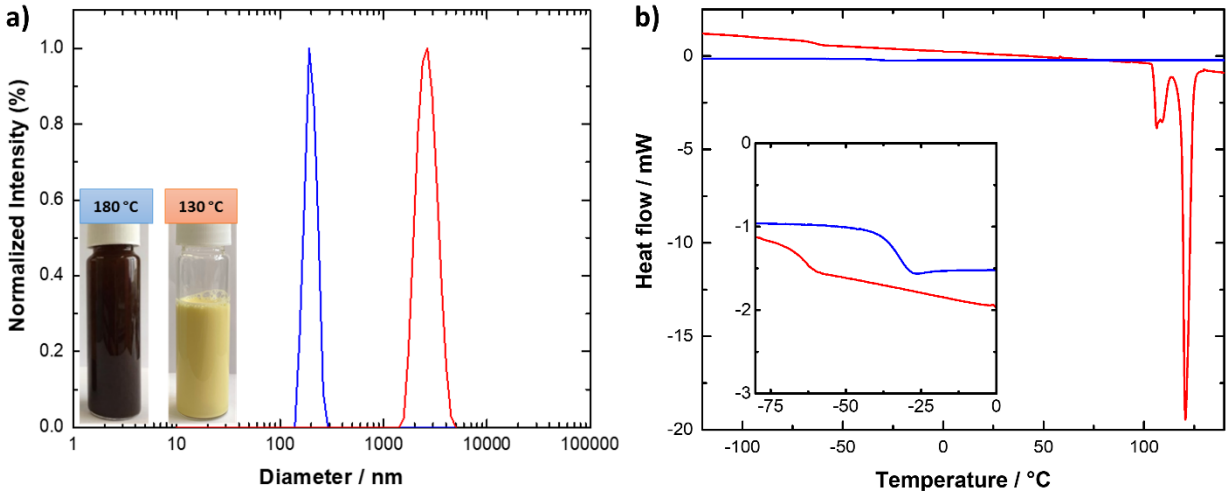

Figure 4.3.2: a) DLS size distribution of polysulfur NPs prepared at 180 °C (blue) and 130 °C (red). Inset showing a representative emulsion of polysulfur NPs prepared at 180 °C and 130 °C. b) DSC of sulfur NPs with full conversion of sulfur to polysulfur (blue) and no conversion (red). Inlet showing T_g of polysulfur NPs.

Table 4.3.1: Effect of the reaction conditions on the conversion of sulfur to polysulfur

Mode	Comonomer	Temperature (°C)	Initiator	Conversion (%)	Yield (%)	Diameter (nm)
Bulk	BMA	180	--			--
Bulk	MeSty	130	NMI	54		--
Miniemulsion	BMA	180	--	99	10	202
Miniemulsion	MeSty	130	NMI	84	53	1087
Miniemulsion	BMA	130	NMI	78	28	482

When the polymerization is carried out at lower temperature (130 °C) a wider range of comonomers can be used to form polymers with higher solubility. However, S_8 no longer spontaneously forms diradicals at 130 °C and required external strategies of initiation indispensable. For example, radical copolymerization of S_8 with styrene was carried out. It was demonstrated that S_8 can initially inhibit the radical polymerization of styrene but as the length of the polysulfide chains grow, the inhibiting effect decreased, resulting in an enhancement of the polymerization rate of styrene over time and the formation inhomogenous copolymers.[220] Such effect was likely caused by the polysulfides acting as a chain transfer agent enhancing the radical polymerization rate. Alternatively, the polymerization of S_8 can be initiated by an anionic mechanism. This strategy was first reported for the copolymerization of S_8 with 1,2-propylene sulfide through a ring-opening mechanism.[209] More recently, the nucleophilic activation of elemental sulfur for inverse vulcanization polymerization was described by the addition amine-based activators, as *N*-methylimidazole (NMI), known to catalyze traditional vulcanization reactions.[211] NMI has the dual effect to promote the S_8 ring-opening leading to the formation of two sulfur radicals due to the lower binding energy and the dynamic covalent character of S-S linkages. To test those different strategies, S_8 was copolymerized with different comonomers (α-methylstyrene (MeSty), butylmethacrylate (BMA) and ε-caprolactone (CL)), in presence of either NMI, di-*tert*-butylperoxide (DTBP) or tin(II) 2-ethylhexanoate (SnEH). The successful incorporation of the comonomers MeSty, BMA and CL into the polysulfur chain could be observed by ^{1}H-NMR spectroscopy (Figure 4.3.3, Figure 4.3.4, Figure 4.3.5).

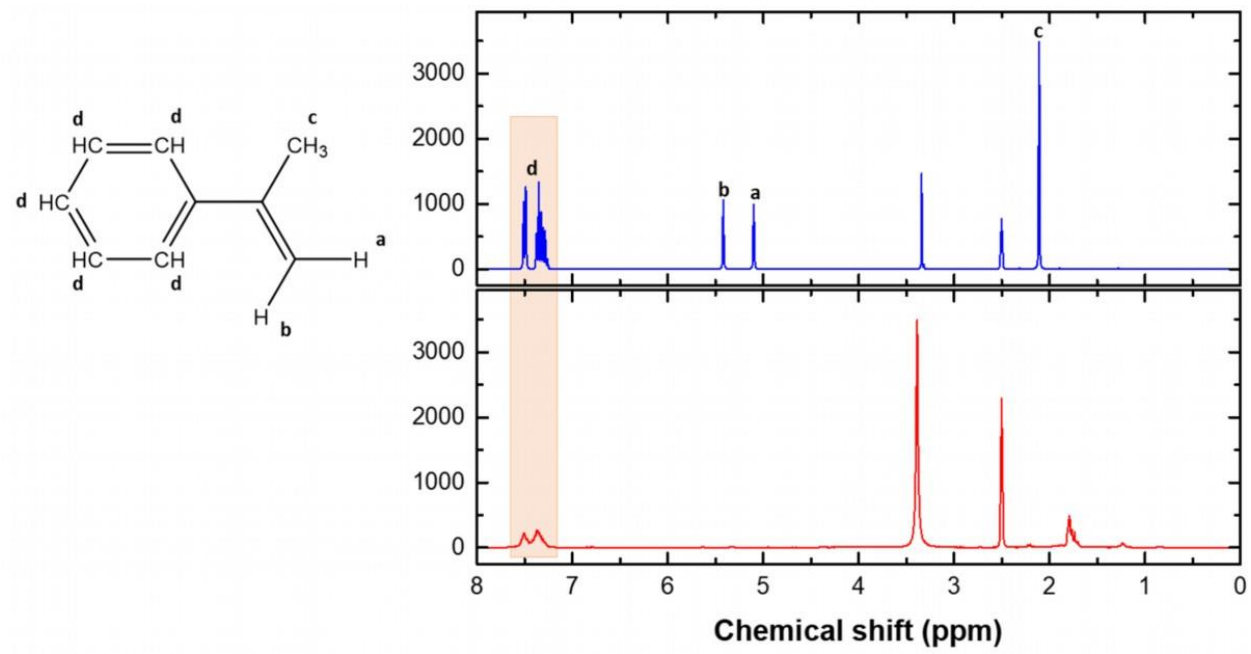

Figure 4.3.3: ^{1}H-NMR spectra of pure MeSty (top) and MeSty containing polySNPs (bottom). MeSty polySNPs were spiked with DCM (5.41 ppm).

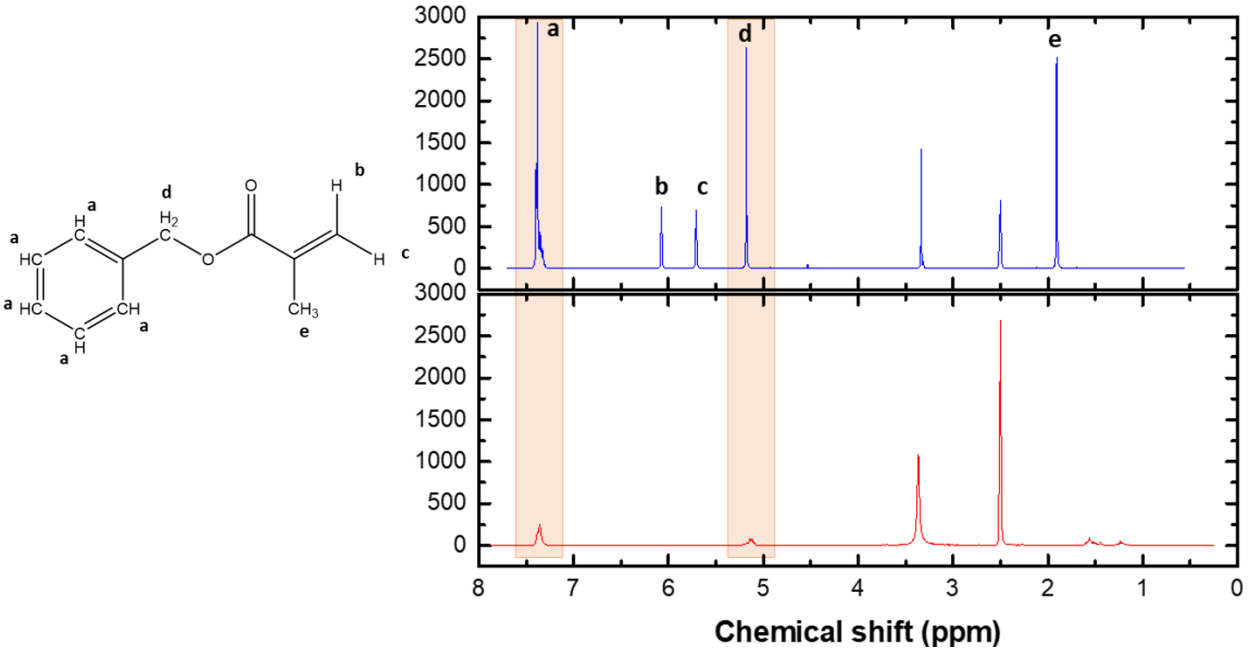

Figure 4.3.4: ^{1}H-NMR spectra of pure BMA (top) and BMA containing polySNPs (bottom).

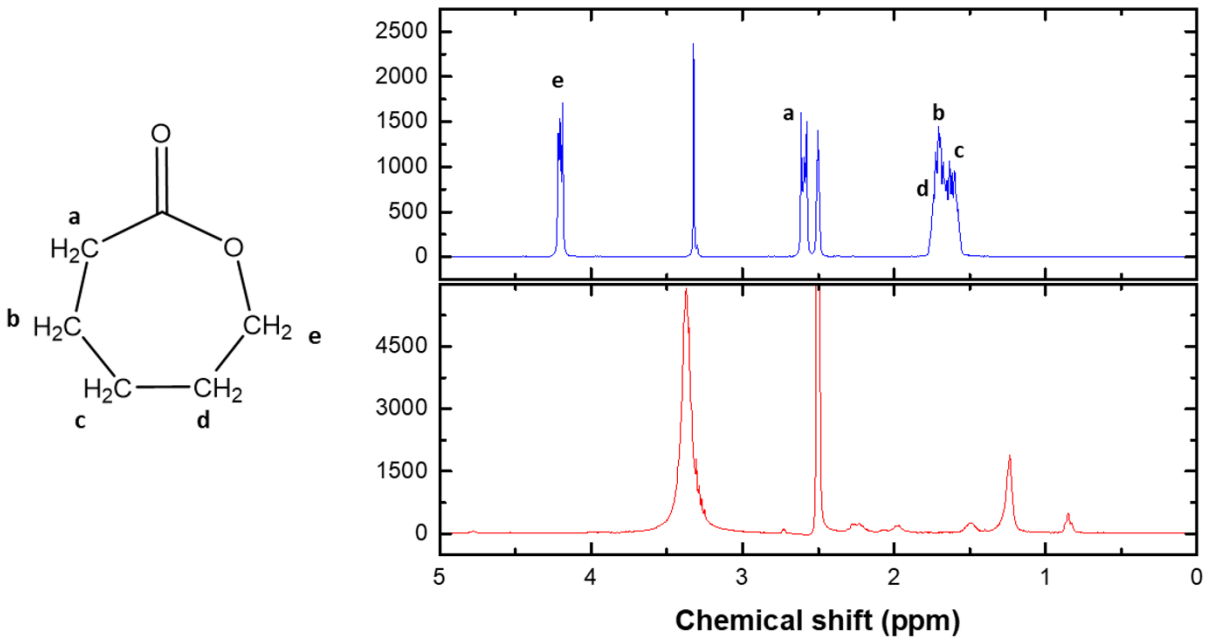

Figure 4.3.5: ^{1}H-NMR spectra of pure ε-caprolactone (top) and ε-caprolactone polySNPs (bottom).

When the temperature of polymerization was decreased from 180 to 130 °C, a moderate decrease in the conversion of S_8 was observed (Table 4.3.1, Figure 4.3.6a). However, systematically, miniemulsion polymerization performed at 180 °C resulted in low yield even though the conversion of the sulfur was high. At 180 °C the S_8 was converted in polySNPs but side reactions leading to the formation of glycerol-soluble products was also observed which considerably reduced the yield of the recovered NPs. However, at 130 °C those side reactions were not observed and the yield of the polymerization reaction increased significantly. The yield of the reaction remained limited by the aggregation and precipitation of some formulation either during the polymerization through Ostwald ripening or during purification due to the loss of surfactant.

The conversion of the S_8 was monitored, in the course of the reaction, the unreacted S_8 in the sample decreased (Figure 4.3.6a). When the polymerization reaction was performed in absence of any comonomer, large remaining amounts of S_8 were observed, likely due to the importance of the inclusion of carbon atom in the polymer backbone to prevent depolymerization upon cooling. Furthermore, in every case, the polymerization rate observed in miniemulsion was higher than in bulk (Figure 4.3.8a). Furthermore, the maximal conversion of S_8 measured was much higher in miniemulsion when compared to bulk (Figure 4.3.6b). Interestingly, when the copolymerization was

performed at 130 °C in absence of any initiator, almost no conversion was observed in bulk, but a significant conversion was observed in miniemulsion. This phenomenon can be ascribe to the local heating (up to 4300 K), which can occur during ultrasonication due to the implosion of the cavitation bubbles.[221] This local and transient region of high temperature could lead to the homolytic opening of the S_8 rings to form diradical sulfur molecules able to initiate the polymerization.

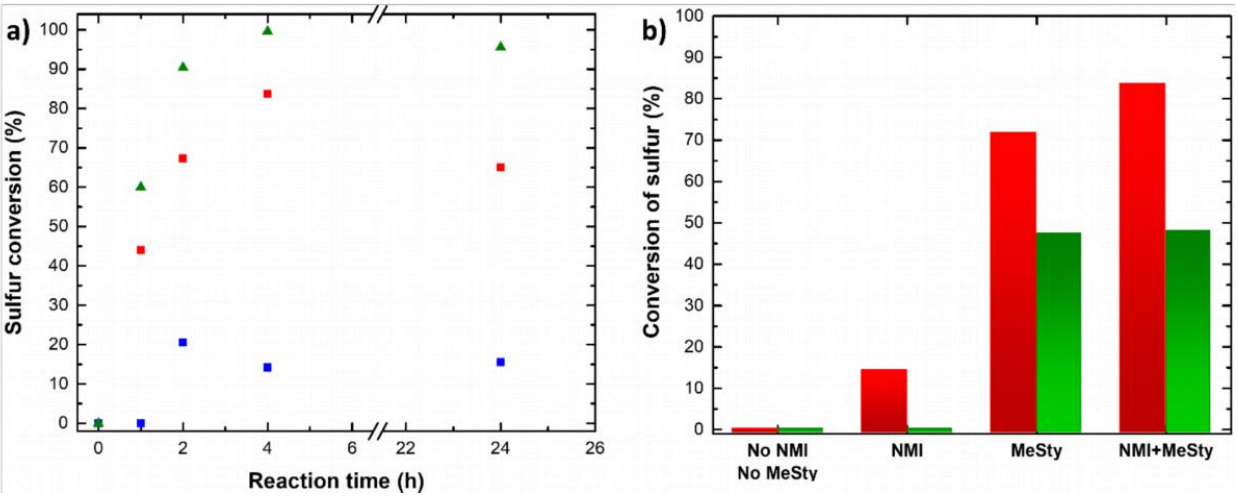

Figure 4.3.6: Analysis of polysulfur NPs. a) Influence of reaction time on conversion of sulfur to polysulfur with and without MeSty as comonomer and NMI as initiator at 180 °C and 130 °C. (Green triangles: Reaction at 180 °C; red squares: Reaction at 130 °C; Blue squares: Reaction at 130 °C without comonomer) b) Sulfur conversion for polySNPs prepared by miniemulsion (red bars) or in bulk (green bars) with and without initiator NMI and comonomer MeSty.

The increased conversion observed in the miniemulsion was a consequence of the nanoconfinement of the monomer within the nanodroplets. Typically, a radical polymerization occurring within nanodroplets leads to a reduction in the termination rate.[222] As a consequence of the segregation effect and the effect of the confined space, the polymerization occurs faster and yields polymer with higher molecular weight in miniemulsion in comparison to bulk. Indeed, the copolymerization of S_8 with MeSty in bulk led to the formation of short polymers with M_n of 1.3 kDa (Figure 4.3.7a), which is typical of inverse vulcanization polymerization performed in bulk.[211] The low molecular weights are usually ascribed to the large difference in reactivity between S_8 and carbon-based monomer.[209] However, when the same monomers mixture was polymerized in the miniemulsion nanodroplets, a M_n of 8.0 kDa was obtained (Figure 4.3.7b), clearly demonstrating the benefits of the nanoconfinement of the miniemulsion on the polymerization reaction.

The chemical and thermal properties of the resulting polymer were analyzed for a series of copolymer prepared at 130 °C with MeSty as a comonomer (Figure 4.3.7b). The ratio of S_8 in the feed was varied from 85.7 to 98.2 mol%, corresponding to a sulfur content of 65 to 94 wt%. The glass transition temperature (T_g) of pure polysulfur has been reported to be 75 °C, while the T_g of polysulfur plasticized with S_8 is ca. -30 °C,[223] and the T_g of poly(α-methyl styrene) is 167 °C.[224] The T_g of the copolymer increases with increasing content of MeSty. However, the relatively low T_g observed in comparison to the T_g of the pure polymers, even when taking into account the plastization by unreacted S_8 suggests that the copolymerization of S_8 with NMI likely yield branched polymers. For all the composition analyzed, the molecular weight of the polymer recovered remained constant at ca. 8 kDa for all comonomer concentrations. However, the conversion of S_8 increased with increasing comonomer concentration.

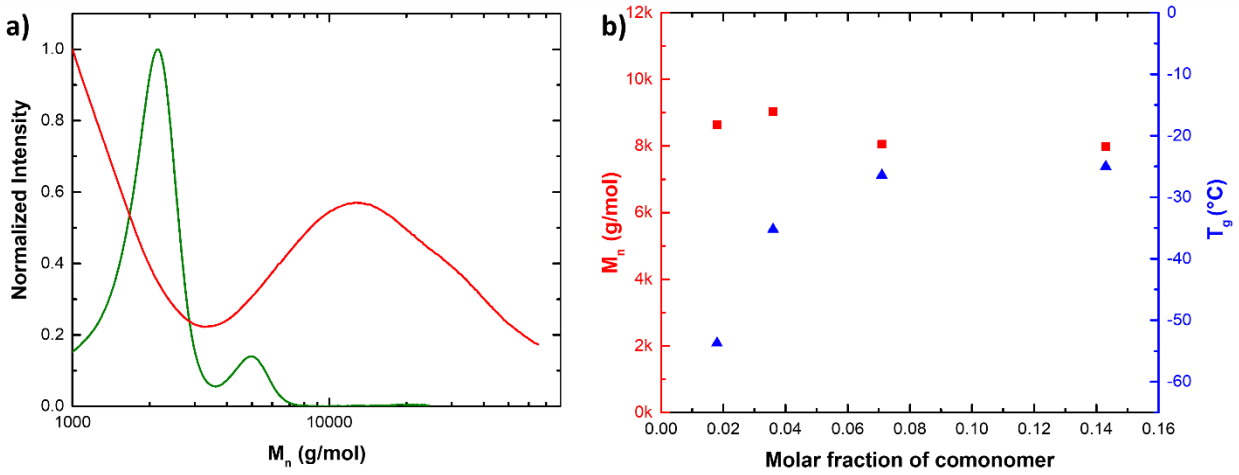

Figure 4.3.7: a) GPC measurements of polysulfur prepared with MeSty/NMI in miniemulsion (red) and in bulk (green) against a polystyrene (PS) standard. b) Influence of comonomer fraction on molecular weight M_n (red squares) and the glass transition temperature T_g (blue triangles).

When the comonomer MeSty was substituted with BMA, the highest conversion was again observed for NMI initiation (78%) (Figure 4.3.8b). However, the sulfur conversion both in bulk and in the miniemulsion was lower than what had been observed with MeSty, likely because BMA is prone to homopolymerization in presence of radicals, while the homopolymerization of MeSty is inhibited. The decrease in sulfur conversion was more important for the polymers prepared in bulk in comparison to the miniemulsion.

The comonomer ε-caprolactone, which undergoes ionic ring-opening polymerization, showed a generally low conversion for all tested initiators (Figure 4.3.8b). Highest conversion of 38% was achieved for the polymerization initiated with tin(II) ethylhexanoate which promote ring-opening copolymerization of the caprolactone with sulfur.

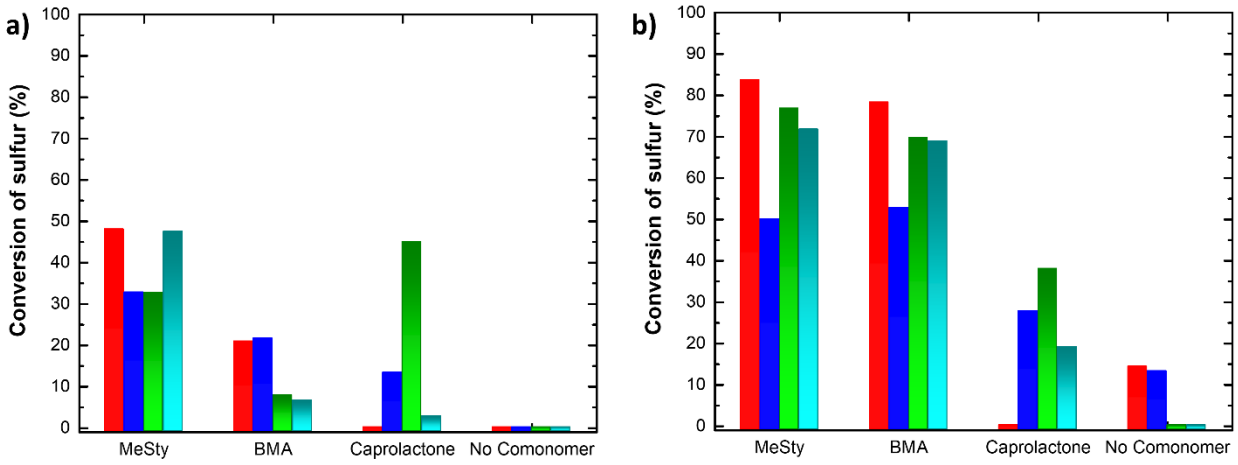

Figure 4.3.8: a) Conversion of sulfur prepared in bulk for comonomers MeSty, BMA, CL, no comonomer and respective initiation by NMI (red), DTBP (blue), SnEH (green), no initiator (turquoise). b) Conversion of sulfur prepared via miniemulsion for comonomers MeSty, BMA, caprolactone, no comonomer and respective initiation by NMI (red), DTBP (blue), tin(II) ethylhexanoate (green), no initiator (turquoise).

The most prominent advantage of polySNPs prepared by miniemulsion is the facile processability. The nanoparticles, which were prepared in glycerol, can be readily resuspended in water. The aqueous suspension of polySNPs can easily be processed by drop casting (Figure 4.3.9a, inset) or spin coating. When shining UV light for 2 h on the polysulfur film, a visible change in the appearance of the film occurs (Figure 4.3.9a, inlet). UV/Vis measurements of the film before and after UV radiation reveals that the absorbance maxima λ_{max} at 430 nm disappeared after the treatment with UV light (Figure 4.3.9a). This phenomenon can be linked to the dynamic covalent nature of S-S bonds which are responsive to UV light.[204] [225]GPC analysis of the polySNPs recovered from the film on the glass slide showed a molecular weight M_n of 2.15 $\frac{kg}{mol}$, which is significantly lower than the 8 $\frac{kg}{mol}$ measured before UV treatment for the identical composition of polySNPs. Therefore, we could show that depolymerization of polySNPs can be induced by UV light.

The exiting potential of sulfurs electrochemistry has previously been described. Therefore, preservation of these beneficial properties within the polySNPs prepared by miniemulsion polymerization is key. The cyclic voltammetry (CV) of the polySNPs showed that the electrochemical behavior inherent to sulfur was preserved (Figure 4.3.9b). The CV measurement showed an oxidation potential E_{ox} of +2.03 V and a reduction potential E_{red} of -0.59 V vs. SCE for the polySNPs. These potentials show great conformation with the redox potentials measured for sulfur-rich materials used in LiS batteries. LiS batteries generally work by conversion reactions on the sulfur cathode and on the metal plating of the lithium anode, following the general equation:

$$S_8 + 16\ Li \rightleftharpoons 8\ Li_2S \tag{4.3.1}$$

The actual redox reaction are much more complex, however, LiS batteries typically show oxidation potentials between 2.2 and 2.6 V, corresponding to the oxidation of lithium sulfide to lithium poly(sulfide)/sulfur.[226] [227] In the fabrication of LiS batteries, a homogeneous sulfur layer on the cathode is key to fully unleash the electrochemical properties of sulfur. Therefore, the possibility to cast films from aqueous suspension of polySNPs directly onto the electrode, enables facile sulfur cathode fabrication.

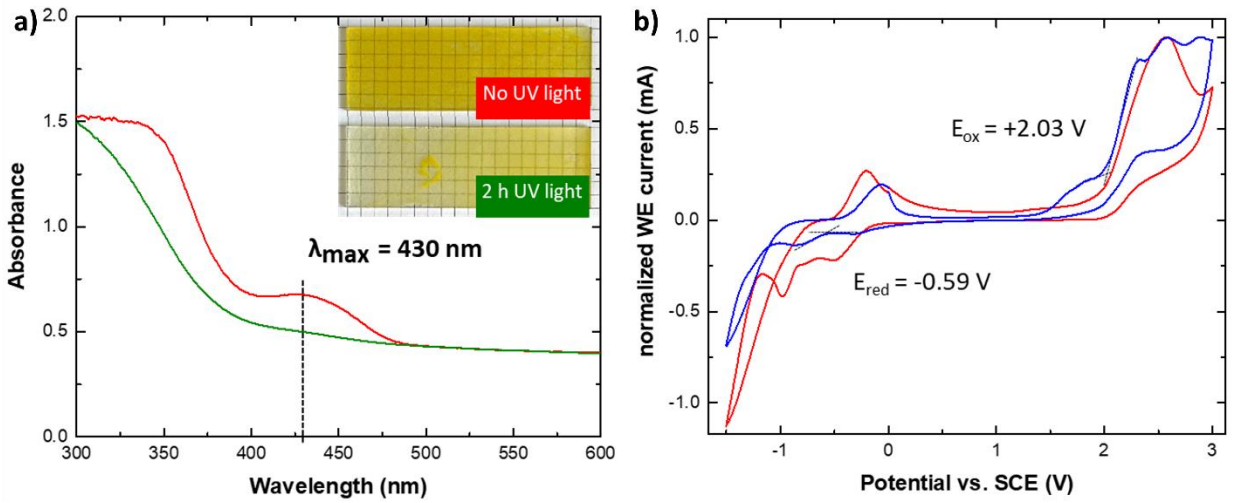

Figure 4.3.9: Polysulfur nanoparticle applications. a) UV-Vis spectra of polysulfur NPs films on a glass slide before (red) and after (green) 6 h UV radiation. Inset showing appearance of films before and after UV irradiation b) Cyclic voltammetry measurements of a film of polysulfur NPs on a glassy carbon electrode (blue) and S_8 (red).

4.3.3 Conclusion

We could show, that the inverse vulcanization of polysulfur nanoparticles via the miniemulsion route, leads to the formation of high sulfur content and high molecular weight particles. In comparison to bulk, the conversion of elemental sulfur to polysulfur improved significantly, which was achieved through the nanoconfinement in the miniemulsion setup. By testing multiple combinations of comonomers and initiating molecules, the polymerization mechanisms were studied in detail. As the polysulfur NPs are obtained in form of an aqueous suspension, processability is facile and allows the formation of thin films on e.g. a glass slide. The prepared films were tested on the behavior under UV light and their electrochemical properties by CV measurements.

5 Summary and outlook

5.1 Summary

This doctoral dissertation was aiming to develop new nanoparticle systems to be used as lubricant additives. The mechanical properties together with the architecture of the nanoparticle dictate their behavior in the tribological contact, and their influence on the lubrication. The different approaches developed here can be used to control and influence the friction between moving surfaces through different mechanisms.

In chapter 4.1, the development of a lubricant additive based on nanocapsules able to encapsulate and release friction modifying molecules was presented. This additive can expand the lubricant lifetime by a self-regulatory mechanoresponsive release induced by the degradation of the lubricant oil and the associated increase of friction in the contact. Mechanoresponsive silica nanocapsules with the ability to precisely tailor shell thickness and nanocapsule diameter were synthesized via direct miniemulsion. A library of SiNCs with different shell thickness and diameter were studied by AFM nanoindentation to reveal the breaking force of individual capsules. The combined results showed, that the breaking force increased with shell thickness and at the same time the breaking pressure decreased with increasing capsule diameter. Furthermore, nanocapsule with an empty core showed superior resistance to the applied load via AFM compared to capsules with a liquid core. The gathered results for the breaking of individual nanocapsules was transferred to the applied mechanoresponsive release of a high number of capsules. By encapsulating a model dye and the subsequent application of an external force by a hydraulic press, the mechanoresponsive release was quantified. It was shown, that more robust SiNCs due to a thicker shell and a smaller diameter release less of their cargo compared to capsules with a more fragile architecture.

In chapter 4.2, a strategy to deliver hydrophilic lubricant molecules to hydrophobic oils by the encapsulation in a suitable nanocarrier system was demonstrated. Hydrophilic glycerol, which is not simply miscible with lubricant oils, was encapsulated in mechanoresponsive polyurethane nanocarriers via inverse miniemulsion. The polyurethane network was formed by the polyaddition reaction between glycerol and the crosslinking agent 2,4-toluene-diisocyanate and provided a sponge-like architecture, surrounding unreacted glycerol. By controlling the concentration of crosslinker, different compositions of glycerol to polyurethane in the final GlyNCs were obtained.

With varied crosslinking ratios, also the mechanical properties changed, as a higher crosslinking increased the Young's modulus. The GlyNCs were transferred to the lubricant oil PAO and then studied on their friction reducing properties by applying the suspension to a ball-on-three plates geometry. Tribological testing revealed, that the GlyNCs not only reduce wear, but also lower the coefficient of friction significantly compared to pure PAO. The amount of mechanoresponsively released glycerol during a tribological measurement was quantified by HPLC, revealing that higher external loads release more glycerol.

In chapter 4.3, the fabrication of polysulfur nanoparticles with high sulfur content was described, outlining a promising approach to deliver larger quantities of sulfur to tribological contacts compared to existing conventional hydrocarbon based sulfur carriers. The polysulfur NPs were prepared via direct miniemulsion at elevated temperature. Through the inverse vulcanization copolymerization of sulfur with low amounts of comonomer, polysulfur nanoparticles of high sulfur content and high molecular weight were obtained. Furthermore, the addition of initiating molecules allowed to reduce the reaction temperature significantly. At low polymerization temperature, a large variety of comonomers can be used with elemental sulfur to yield the polymers. The comparison of identical comonomer/initiator combinations prepared in bulk and in miniemulsion, demonstrated the advantages of nanoconfinement in miniemulsion as it led to much higher conversions of elemental sulfur to polymerized sulfur. The polysulfur nanoparticles were obtained as an aqueous suspension, which allowed facile processing to form e.g. a thin film on a glass substrate.

In summary, different strategies to improve the performance and lifetime of lubricant oils were presented. The encapsulation of hydrophobic molecules in silica nanocarriers with tunable mechanical properties enables controlled mechanoresponsive release and therefore a promising strategy to control friction in tribological contacts long term. Further, glycerol based nanocarriers allow the delivery and release of hydrophilic glycerol to hydrophobic lubricant oils, circumventing the miscibility issues occurring by direct mixing of glycerol and the oil. Finally, high sulfur content nanoparticles represent a promising new lubricant additive, which enables the introduction of sulfur in high concentrations to tribological contacts.

5.2 Outlook

This thesis showed the synthesis and characterization of three different types of nanoparticles which can all be applied as lubricant additives. Each system is composed of a different material, allowing to introduce a broad range of chemistry to the tribological contact. Furthermore, the ability to encapsulate additional molecules inside the nanocarriers, enables the delivery of even more friction modifying components to the lubricant system.

Three potential lubricant nanoadditives were developed here, but those systems need to be tested in conditions close to their potential applications. For example, silica nanocapsules could be used for the encapsulation and the mechanoresponsive release of typical friction modifying molecules like glycerol trioleate and oleic acid esters and used in suspension in lubricant oil. Similarly, hydrophilic friction modifier, like glycerol, are known to be especially efficient to lubricate metal surface coated with a film of amorphous carbon (taC). The use of the GlyNCs-PAO nanocapsules in taC/metal contact has the potential to reach the regime of superlubricity. Polysulfur nanoparticles with high sulfur content, obtained in form of an aqueous suspension, enables their application in aqueous lubricant systems as for example metal working fluids or coatings. Further, the implementation of functional groups could be realized by using appropriate comonomers with initial functionalities. This allows to perform post-functionalization reactions on the particle surface in order to attach e.g. long aliphatic chains which would grant colloidal stability in hydrophobic lubricants. Finally, the effect of temperature on the tribological properties of nanomaterial-containing lubricant system should be studied. The nanomaterials developed here are stabilized by steric repulsion which can be affected by the temperature and change the colloidal stability of the system. Furthermore, the viscosity generally shows a temperature dependence, the effect of higher temperature on the interplay of the nanomaterials in a less viscous lubricant should be monitored.

The overall potential of nanoparticles as lubricant additives is immense and has by far not been fully exploited. For example, the choice of materials used in the design of the nanocapsules could bring additional properties, moving from silica to shell with higher thermal conductivity such as Al_2O_3 or TiO_2 can be used for enhanced heat dissipation and wear reduction. Additionally, nanoparticles offer the possibility to perform surface modifications, which can be used to attach molecules to the particle surface. Such molecules can fulfill simple tasks as granting colloidal stability by steric stabilization

through the attachment of long aliphatic chains when dispersing the NPs in hydrophobic oils. But also functional groups can be attached to the NPs surface to improve e.g. adhesion to contact surfaces or introduce even more new chemistry as antioxidant components or viscosity index improving polymers.

Besides solid nanoparticles, also hollow nanocapsules with the ability to encapsulate and deliver a cargo offer a broad spectrum of future applications as lubricant additives. By controlling the mechanical properties of nanocapsules, the same intrinsic friction reducing mechanism observed for solid nanoparticles can be transferred to nanocapsules. By combining these properties with the encapsulation of other additive molecules, new nanocapsule system can be developed. For example the encapsulation of inorganic additives as the friction modifying MoS_2 or anticorrosion, antioxidant and antiwear agents can be realized by nanocapsules. This approach allows for the combination of multiple additives in one simple nanocapsule system, which is capable of releasing the encapsulated additives in a controlled manner. As a benefit, the interplay of the numerous additives which can be found in modern lubricants would be facilitated by combining certain functions of additives in one system.

Furthermore, the introduction of new release triggers can result in exiting and innovative nanocapsule additives. For example, release can be trigger by a change in pH of the lubricant oil, allowing for the design of a nanocapsule additive, able to respond to pH and potentially even reset the pH by subsequent release of pH lowering or raising molecules. Release can also be triggered by temperature, which enables the design of a thermo responsive nanocarrier system that releases its cargo once a certain temperature threshold is exceeded. Additionally, bacteria-responsive nanocarriers can be developed as lubricant additives. As the degradation of lubricants and furthermore the contamination of lubricant oils is a contemporary challenge, the ability to develop nanocarriers which can respond to bacteria or enzymes present in nature, exhibits a great opportunity to address this challenge.

Finally, because of new environmental regulations, the fate of polymer nanomaterials used in end-user product need to be carefully considered. With regard to the biodegradability of nanoparticle additives, various approaches to modify the chemistry of the additive in order to improve its biodegradability are existing. The implementation of hydrolysis-labile components in the polymer

network of e.g. polyurethane nanocarriers can improve their degradation significantly.[228] Also the addition of poly(lactide) sections to the nanocarrier shell leads to biodegradable nanocarriers.[229]

6 Acknowledgements

7 Publications

8 References

[1] K. Holmberg, A. Erdemir, *Friction* **2017**, *5*, 263-284.

[2] K. Holmberg, P. Andersson, N.-O. Nylund, K. Mäkelä, A. Erdemir, *Tribology International* **2014**, *78*, 94-114.

[3] T. Mang, W. Dresel, *Lubricants and Lubrication*, Wiley-VCH, **2017**.

[4] W. Dai, B. Kheireddin, H. Gao, H. Liang, *Tribology International* **2016**, *102*, 88-98.

[5] J. Padgurskas, R. Rukuiza, I. Prosyčevas, R. Kreivaitis, *Tribology International* **2013**, *60*, 224-232.

[6] R. A. Wright, K. Wang, J. Qu, B. Zhao, *Angewandte Chemie International Edition* **2016**, *55*, 8656-8660.

[7] J. Zhao, Y. He, Y. Wang, W. Wang, L. Yan, J. Luo, *Tribology International* **2016**, *97*, 14-20.

[8] K. Sathickbasha, A. Selvakumar, M. S. Balaji, B. S. Rajan, *Materials Research Express* **2019**, *6*, 045315.

[9] S. Tan, S. J. R.L., W. T. Ford, *Langmuir* **2004**, *20*, 7015-7020.

[10] J. Yin, M. Retsch, J. H. Lee, E. L. Thomas, M. C. Boyce, *Langmuir* **2011**, *27*, 10492-10500.

[11] L. Joly-Pottuz, F. Dassenoy, M. Belin, B. Vacher, J. M. Martin, N. Fleischer, *Tribology Letters* **2005**, *18*, 477-485.

[12] Y. Long, M.-I. D. B. Bouchet, T. Lubrecht, T. Onodera, J. M. Martin, *Scientific Reports* **2019**, *9*, 6286.

[13] L. Joly-Pottuz, J. M. Martin, M. I. De Barros Bouchet, M. Belin, *Tribology Letters* **2008**, *34*, 21-29.

[14] J. J. Griebel, R. S. Glass, K. Char, J. Pyun, *Progress in Polymer Science* **2016**, *58*, 90-125.

[15] W. J. Chung, J. J. Griebel, E. T. Kim, H. Yoon, A. G. Simmonds, H. J. Ji, P. T. Dirlam, R. S. Glass, J. J. Wie, N. A. Nguyen, B. W. Guralnick, J. Park, A. Somogyi, P. Theato, M. E. Mackay, Y. E. Sung, K. Char, J. Pyun, *Nature Chemistry* **2013**, *5*, 518-524.

[16] A. Musyanovych, K. Landfester, *Macromolecular Bioscience* **2014**, *14*, 458-477.

[17] F. U. Din, J. Y. Choi, D. W. Kim, O. Mustapha, D. S. Kim, R. K. Thapa, S. K. Ku, Y. S. Youn, K. T. Oh, C. S. Yong, J. O. Kim, H. G. Choi, *Drug Delivery* **2017**, *24*, 502-510.

[18] A. Bordat, T. Boissenot, J. Nicolas, N. Tsapis, *Advanced Drug Delivery Reviews* **2019**, *138*, 167-192.

[19] V. Marturano, P. Cerruti, C. Carfagna, M. Giamberini, B. Tylkowski, V. Ambrogi, *Polymer* **2015**, *70*, 222-230.

[20] Y. Lv, L. Hao, W. Hu, Y. Ran, Y. Bai, L. Zhang, *Scientific Reports* **2016**, *6*, 29321.

[21] H. Zhang, J. Fei, X. Yan, A. Wang, J. Li, *Advanced Functional Materials* **2015**, *25*, 1193-1204.

[22] R. Liu, X. Zhao, T. Wu, P. Feng, *Journal of the American Chemical Society* **2008**, *130*, 14418-14419.

[23] J. Wang, J. A. Kaplan, Y. L. Colson, M. W. Grinstaff, *Advanced Drug Delivery Reviews* **2017**, *108*, 68-82.

[24] T. J. Merkel, S. W. Jones, K. P. Herlihy, F. R. Kersey, A. R. Shields, M. Napier, J. C. Luft, H. Wu, W. C. Zamboni, A. Z. Wang, J. E. Bear, J. M. DeSimone, *Proceedings of the National Academic Society of the USA.* **2011**, *108*, 586-591.

[25] M. Hu, S. Peil, Y. Xing, D. Döhler, L. Caire da Silva, W. H. Binder, M. Kappl, M. B. Bannwarth, *Materials Horizons* **2018**, *5*, 51-58.
[26] J. Fickert, P. Rupper, R. Graf, K. Landfester, D. Crespy, *Journal of Materials Chemistry* **2012**, *22*, 2286-2291.
[27] C. J. Thrasher, Z. J. Farrell, N. J. Morris, C. L. Willey, C. E. Tabor, *Advanced Materials* **2019**, *31*, 1903864.
[28] K. Landfester, *Angewandte Chemie International Edition* **2009**, *48*, 4488-4507.
[29] F. J. Schork, Y. Luo, W. Smulders, J. P. Russum, A. Butté, K. Fontenot, in *Polymer Particles, Vol. 175*, **2005**, pp. 129-255.
[30] S. Slomkowski, J. V. Alemán, R. G. Gilbert, M. Hess, K. Horie, R. G. Jones, P. Kubisa, I. Meisel, W. Mormann, S. Penczek, R. F. T. Stepto, *Pure and Applied Chemistry* **2011**, *83*, 2229-2259.
[31] J. Ugelstad, F. K. Hansen, *Journal of Polymer Science* **1978**, *16*, 1953-1979.
[32] T. Delmas, H. Piraux, A. C. Couffin, I. Texier, F. Vinet, P. Poulin, M. E. Cates, J. Bibette, *Langmuir* **2011**, *27*, 1683-1692.
[33] F. Villalobos-Castillejos, V. G. Granillo-Guerrero, D. E. Leyva-Daniel, L. Alamilla-Beltrán, G. F. Gutiérrez-López, A. Monroy-Villagrana, S. M. Jafari, in *Nanoemulsions*, Academic Press, **2018**, pp. 207-232.
[34] I. O. Ocampo, D. I. Ellez, C. Jimenez, G. Davila, *International Journal of Environment, Agriculture and Biotechnology* **2016**, *1*.
[35] M. S. Alkanawati, F. R. Wurm, H. Thérien-Aubin, K. Landfester, *Macromolecular Materials and Engineering* **2018**, *303*.
[36] K. Landfester, *Advanced Materials* **2001**, *13*, 765-768.
[37] Y. Song, J.-B. Fan, S. Wang, *Materials Chemistry Frontiers* **2017**, *1*, 1028-1040.
[38] D. Crespy, M. Stark, C. Hoffman-Richter, U. Ziener, K. Landfester, *Macromolecules* **2007**, *40*, 3122-3135.
[39] M. Machtakova, S. Han, Y. Yangazoglu, I. Lieberwirth, H. Therien-Aubin, K. Landfester, *Nanoscale* **2021**, *13*, 4051-4059.
[40] J. Fickert, D. Schaeffel, K. Koynov, K. Landfester, D. Crespy, *Colloid and Polymer Science* **2013**, *292*, 251-255.
[41] S. Jiang, M. Mottola, S. Han, R. Thiramanas, R. Graf, I. Lieberwirth, V. Mailänder, D. Crespy, K. Landfester, *Particle & Particle Systems Characterization* **2020**, *37*.
[42] G. B. Sukhorukov, E. Donath, H. Lichtenfeld, E. Knippel, M. Knippel, A. Budde, H. Möhwald, *Colloids and Surfaces A: Physicochemical and Engineering Aspects* **1998**, *137*, 253-266.
[43] F. Caruso, *Chemistry - A European Journal* **2000**, *6*, 413-419.
[44] F. Caruso, R. A. Caruso, H. Möhwald, *Science* **1998**, *282*, 1111-1114.
[45] T. G. Shutava, P. P. Pattekari, K. A. Arapov, V. P. Torchilin, Y. M. Lvov, *Soft Matter* **2012**, *8*, 9418-9427.
[46] Z. Ferjaoui, S. Nahle, C. S. Chang, J. Ghanbaja, O. Joubert, R. Schneider, L. Ferrari, E. Gaffet, H. Alem, *ACS Omega* **2020**, *5*, 4770-4777.
[47] A. Agarwal, Y. Lvov, R. Sawant, V. Torchilin, *Journal of Controlled Release* **2008**, *128*, 255-260.
[48] Y. Chen, X. Lin, H. Park, R. Greever, *Nanomedicine* **2009**, *5*, 316-322.

[49] A. Jafari, H. Sun, B. Sun, M. A. Mohamed, H. Cui, C. Cheng, *Chemical Communications* **2019**, *55*, 1267-1270.
[50] J. Campbell, A. S. Vikulina, *Polymer* **2020**, *12*.
[51] S. Torza, S. G. Mason, *Journal of Colloid and Interface Science* **1970**, *33*, 67-83.
[52] C. Bohlender, K. Landfester, D. Crespy, A. Schiller, *Particle & Particle Systems Characterization* **2013**, *30*, 138-142.
[53] A. D. Dinsmore, M. F. Hsu, M. G. Nikolaides, M. Marquez, A. R. Bausch, D. A. Weitz, *Science* **2002**, *298*, 1006-1009.
[54] D. Crespy, K. Landfester, *Beilstein Journal of Organic Chemistry* **2010**, *6*, 1132-1148.
[55] J. Zhang, H. Chen, L. Xu, Y. Gu, *Journal of Controlled Release* **2008**, *131*, 34-40.
[56] Y. Cheng, J. Hao, L. A. Lee, M. C. Biewer, Q. Wang, M. C. Stefan, *Biomacromolecules* **2012**, *13*, 2163-2173.
[57] J. Fischer, S. J. Beckers, D. Yiamsawas, E. Thines, K. Landfester, F. R. Wurm, *Advanced Science* **2019**, *6*, 1802315.
[58] S. Behzadi, J. Stadler, S. Hosseinpour, D. Crespy, K. Landfester, *Colloids and Surfaces A: Physicochemical and Engineering Aspects* **2017**, *532*, 2-7.
[59] D. Klinger, K. Landfester, *Macromolecules* **2011**, *44*, 9758-9772.
[60] K. Ariga, T. Mori, J. P. Hill, *Advanced Materials* **2012**, *24*, 158-176.
[61] R. Rajamanickam, S. Baek, K. Gwon, Y. Hwang, K. Shin, G. Tae, *Journal of Materials Chemistry B* **2016**, *4*, 4278-4286.
[62] K. Landfester, A. Musyanovych, V. Mailänder, *Journal of Polymer Science Part A: Polymer Chemistry* **2010**, *48*, 493-515.
[63] H. Izawa, K. Kawakami, M. Sumita, Y. Tateyama, J. P. Hill, K. Ariga, *Journal of Materials Chemistry B* **2013**, *1*, 2155-2161.
[64] J. Di, S. Yao, Y. Ye, Z. Cui, J. Yu, T. K. Ghosh, Y. Zhu, Z. Gu, *ACS Nano* **2015**, *9*, 9407-9515.
[65] H. Spikes, *Tribology Letters* **2015**, *60*, 5.
[66] J. V. Alemán, A. V. Chadwick, J. He, M. Hess, K. Horie, R. G. Jones, P. Kratochvíl, I. Meisel, I. Mita, G. Moad, S. Penczek, R. F. T. Stepto, *Pure and Applied Chemistry* **2007**, *79*, 1801-1829.
[67] K. Schwirn, I. Beer, *Environmental Sciences Europe* **2014**, *26*, 4.
[68] J. Zeng, H. Yu, *Journal of Nanomaterials* **2012**, *2012*, 147169.
[69] L. Rapoport, V. Leshchinsky, I. Lapsker, Y. Volovik, O. Nepomnyashchy, M. Lvovsky, R. Popovitz-Biro, Y. Feldman, R. Tenne, *Wear* **2003**, *255*, 785-793.
[70] L. Si, D. Guo, J. Luo, X. Lu, G. Xie, *Journal of Applied Physics* **2011**, *109*.
[71] F. Ilie, *Journal of Nanoparticle Research* **2012**, *14*, 752.
[72] Y. Chen, W. Mu, J. Lu, *Journal of Nanoparticle Research* **2012**, *14*, 696.
[73] H.-J. Butt, B. Cappella, M. Kappl, *Surface Science Reports* **2005**, *59*, 1-152.
[74] M. Kappl, H. J. Butt, *Particle & Particle Systems Characterization* **2002**, *19*, 129-143.
[75] C. E. Carlton, P. J. Ferreira, *Micron* **2012**, *43*, 1134-1139.
[76] H. C. Hamaker, *Physica* **1937**, *4*, 1058-1072.
[77] B. Derjaguin, *Kolloid-Zeitschrift* **1934**, *69*, 155-164.
[78] I. E. Dzyaloshinskii, E. M. Lifshitz, L. P. Pitaevskii, *Soviet Physics Uspekhi* **1961**, *4*, 153.
[79] S.-W. Bian, I. A. Mudunkotuwa, T. Rupasinghe, V. H. Grassian, *Langmuir* **2011**, *27*, 6059-6068.

[80] T. Laaksonen, P. Ahonen, C. Johans, K. Kontturi, *ChemPhysChem* **2006**, *7*, 2143-2149.
[81] C.-H. Lee, G.-H. Lee, A. M. van der Zande, W. Chen, Y. Li, M. Han, X. Cui, G. Arefe, C. Nuckolls, T. F. Heinz, J. Guo, J. Hone, P. Kim, *Nature Nanotechnology* **2014**, *9*, 676-681.
[82] A. K. Geim, I. V. Grigorieva, *Nature* **2013**, *499*, 419-425.
[83] J. Cumings, A. Zettl, *Science* **2000**, *289*, 602-604.
[84] R. O. James, G. A. Parks, in *Surface and Colloid Science, Vol. 12*, Springer, **1982**, pp. 119-216.
[85] H. J. Butt, M. Kappl, *Advances in Colloid and Interface Science* **2009**, *146*, 48-60.
[86] P. A. Kralchevsky, K. Nagayama, *Advances in Colloid and Interface Science* **2000**, *85*, 145-192.
[87] J. Diao, K. Gall, M. L. Dunn, J. A. Zimmerman, *Acta Materialia* **2006**, *54*, 643-653.
[88] J. Diao, K. Gall, M. L. Dunn, *Nano Letters* **2004**, *4*, 1863-1867.
[89] W. Zhang, T. Wang, X. Chen, *Journal of Applied Physics* **2008**, *103*, 123527.
[90] D. Farkas, A. Caro, E. Bringa, D. Crowson, *Acta Materialia* **2013**, *61*, 3249-3256.
[91] B.-N. D. Ngô, A. Stukowski, N. Mameka, J. Markmann, K. Albe, J. Weissmüller, *Acta Materialia* **2015**, *93*, 144-155.
[92] L. Lührs, B. Zandersons, N. Huber, J. Weissmüller, *Nano Letters* **2017**, *17*, 6258-6266.
[93] N. Mameka, J. Markmann, J. Weissmüller, *Nature Communications* **2017**, *8*, 1976.
[94] K. L. Johnson, K. Kendall, A. D. Roberts, D. Tabor, *Proceedings of the Royal Society of London. A. Mathematical and Physical Sciences* **1971**, *324*, 301-313.
[95] D. Guo, J. Li, G. Xie, Y. Wang, J. Luo, *Langmuir* **2014**, *30*, 7206-7212.
[96] J.-M. Y. Carrillo, E. Raphael, A. V. Dobrynin, *Langmuir* **2010**, *26*, 12973-12979.
[97] B. Derjaguin, V. M. Muller, Y. P. Toporov, *Journal of Colloid and Interface Science* **1975**, *53*, 314-326.
[98] K. Miyake, N. Satomi, S. Sasaki, *Applied Physics Letters* **2006**, *89*.
[99] M. Zou, D. Yang, *Tribology Letters* **2006**, *22*, 189-196.
[100] S. Cuenot, C. Frétigny, S. Demoustier-Champagne, B. Nysten, *Physical Review B* **2004**, *69*.
[101] A. E. Pelling, S. Sehati, E. B. Gralla, J. S. Valentine, J. K. Gimzewski, *Science* **2004**, *305*, 1147-1150.
[102] W. C. Oliver, G. M. Pharr, *Journal of Materials Research* **2011**, *7*, 1564-1583.
[103] R. B. King, *International Journal of Solids and Structures* **1987**, *23*, 1657-1664.
[104] R. Saha, W. D. Nix, *Acta Materialia* **2002**, *50*, 22-38.
[105] H. Hertz, *Angewandte Mathematik* **1881**, *92*, 156-171.
[106] S. A. Chizhik, Z. Huang, V. V. Gurbunov, N. K. Myshkin, V. V. Tsukruk, *Langmuir* **1998**, *14*, 2606-2609.
[107] E. Reissner, *Journal of Mathematics and Physics* **1946**, *25*, 80-85.
[108] J. D. Berry, S. Mettu, R. R. Dagastine, *Soft Matter* **2017**, *13*, 1943-1947.
[109] L. Calabri, N. Pugno, C. Menozzi, S. Valeri, *Journal of Physics: Condensed Matter* **2008**, *20*.
[110] G. M. Pharr, W. C. Oliver, *Journal of Materials Research* **2011**, *4*, 94-101.
[111] D. Maharaj, B. Bhushan, *Beilstein Journal of Nanotechnology* **2014**, *5*, 822-836.
[112] W. D. Nix, H. Gao, *Journal of the Mechanics and Physics of Solids* **1998**, *46*, 411-425.
[113] M. S. Chavali, M. P. Nikolova, *SN Applied Sciences* **2019**, *1*, 607.
[114] G. M. Pharr, *Materials Science & Engineering R-reports* **1998**, *253*, 151-159.
[115] L. An, D. Zhang, L. Zhang, G. Feng, *Nanoscale* **2019**, *11*, 9563-9573.

[116] R. Y. Hong, Q. Chen, *Dispersion of Inorganic Nanoparticles in Polymer Matrices: Challenges and Solutions*, Springer, **2015**.
[117] L. Mishnaevsky, E. Levashov, R. Z. Valiev, J. Segurado, I. Sabirov, N. Enikeev, S. Prokoshkin, A. V. Solov'yov, A. Korotitskiy, E. Gutmanas, I. Gotman, E. Rabkin, S. Psakh'e, L. Dluhoš, M. Seefeldt, A. Smolin, *Materials Science and Engineering: R: Reports* **2014**, *81*, 1-19.
[118] Z. Cai, X. Zhao, J. Duan, D. Zhao, Z. Dang, Z. Lin, *Frontiers of Environmental Science & Engineering* **2020**, *14*, 84.
[119] P. Pino, F. Yang, B. Pelaz, Q. Zhang, K. Kantner, R. Hartmann, N. Martinez de Baroja, M. Gallego, M. Möller, B. B. Manshian, S. J. Soenen, R. Riedel, N. Hampp, W. J. Parak, *Angewandte Chemie International Edition* **2016**, *55*, 5483-5487.
[120] J. Di, S. Yao, Y. Ye, Z. Cui, J. Yu, T. K. Ghosh, Y. Zhu, Z. Gu, *ACS Nano* **2015**, *9*, 9407-9415.
[121] N. Korin, M. Kanapathipallai, B. D. Matthews, M. Crescente, A. Brill, T. Mammoto, K. Ghosh, S. Jurek, S. A. Bencherif, D. Bhatta, A. U. Coskun, C. L. Feldman, D. Wagner, D. E. Ingber, *Scientific Reports* **2012**, *337*, 738-742.
[122] T. Saxer, A. Zumbuehl, B. Müller, *Cardiovascular Research* **2013**, *99*, 328-333.
[123] N. Korin, M. J. Gounis, A. K. Wakhloo, D. E. Ingber, *JAMA Neurology* **2015**, *72*, 119-122.
[124] J. F. Patrick, M. J. Robb, N. R. Sottos, J. S. Moore, S. R. White, *Nature* **2016**, *540*, 363-370.
[125] C. Calvino, E. Henriet, L. F. Muff, S. Schrettl, C. Weder, *Macromolecular Rapid Communications* **2020**, *41*, 1900654.
[126] H. S. Lee, H. D. Jeong, D. A. Dornfeld, *Precision Engineering* **2013**, *37*, 483-490.
[127] H. Chen, D. Guo, G. Xie, G. Pan, *Friction* **2016**, *4*, 153-164.
[128] J. Ryu, W. Kim, J. Yun, K. Lee, J. Lee, H. Yu, J. H. Kim, J. J. Kim, J. Jang, *ACS Applied Materials & Interfaces* **2018**, *10*, 11843-11851.
[129] J. Cheng, S. Huang, X. Lu, *ECS Journal of Solid State Science and Technology* **2020**, *9*, 024015.
[130] D.-X. Peng, *Industrial Lubrication and Tribology* **2014**, *66*, 124-130.
[131] Z. Zhang, J. Liu, W. Hu, L. Zhang, W. Xie, L. Liao, *Journal of Manufacturing Processes* **2021**, *62*, 762-771.
[132] M. J. Kao, F. C. Hsu, D. X. Peng, *Advances in Materials Science and Engineering* **2014**, *2014*, 691967.
[133] F. Ilie, C. Covaliu, *Lubricants* **2016**, *4*.
[134] T. D. Lopez, A. F. Gonzalez, A. Del Reguero, M. Matos, M. E. Diaz-Garcia, R. Badia-Laino, *Science and Technology of Advanced Materials* **2015**, *16*, 055005.
[135] M.-J. Kao, C.-R. Lin, *Journal of Alloys and Compounds* **2009**, *483*, 456-459.
[136] I. Minami, *Applied Sciences* **2017**, *7*, 445.
[137] H. Olsson, K. J. Åström, C. Canudas de Wit, M. Gäfvert, P. Lischinsky, *European Journal of Control* **1998**, *4*, 176-195.
[138] B. N. J. Persson, *Sliding Friction-Physical Principles and Applications*, Springer, **2000**.
[139] A. Doménech, T. Doménech, J. Cebrián, *American Journal of Physics* **1987**, *55*, 231-235.
[140] R. Stribeck, *Die Wesentlichen Eigenschaften der Gleit- und Rollenlager*, Springer, **1903**.
[141] M. D. Hersey, *Journal of the Washington Academy of Sciences* **1914**, *4*, 542-552.
[142] R. Fogel'Son, E. Likhachev, *Technical Physics* **2001**, *46*, 1056-1059.
[143] J. W. Schmelzer, E. D. Zanotto, V. M. Fokin, *The Journal of Chemical Physics* **2005**, *122*, 074511.

[144] M. Sánchez-Rubio, F. Chinas-Castillo, F. Ruiz-Aquino, J. Lara-Romero, *Lubrication Science* **2006**, *18*, 95-108.
[145] K. Kato, K. Adachi, in *Modern Tribology Handbook: Volume One: Principles of Tribology*, CRC press, **2000**, pp. 273-300.
[146] A. A. Torrance, *Wear* **2005**, *258*, 281-293.
[147] J. T. Burwell, *Wear* **1957**, *1*, 119-141.
[148] R. Aghababaei, D. H. Warner, J.-F. Molinari, *Nature Communications* **2016**, *7*, 11816.
[149] W. Maw, F. Stevens, S. Langford, J. Dickinson, *Journal of Applied Physics* **2002**, *92*, 5103-5109.
[150] A. Abdelbary, in *Wear of Polymers and Composites*, Woodhead Publishing, **2014**, pp. 1-36.
[151] A. E. Jiménez, M. D. Bermúdez, in *Tribology for Engineers*, Woodhead Publishing, **2011**, pp. 33-63.
[152] D. Arnell, in *Tribology and Dynamics of Engine and Powertrain*, Woodhead Publishing, **2010**, pp. 41-72.
[153] G. W. Stachowiak, A. W. Batchelor, in *Tribology Series, Vol. 24*, Elsevier, **1993**, pp. 557-612.
[154] X. Escaler, E. Egusquiza, M. Farhat, F. Avellan, M. Coussirat, *Mechanical Systems and Signal Processing* **2006**, *20*, 983-1007.
[155] D. Berman, A. Erdemir, A. V. Zinovev, A. V. Sumant, *Diamond and Related Materials* **2015**, *54*, 91-96.
[156] M. Rasberger, in *Chemistry and Technology of Lubricants*, Springer Netherlands, **1997**, pp. 98-143.
[157] L. R. Rudnick, *Lubricant Additives: Chemistry and Applications*, CRC press, **2017**.
[158] M. J. Covitch, K. J. Trickett, *Advances in Chemical Engineering and Science* **2015**, *5*, 18.
[159] Q. Sunqing, D. Junxiu, C. Guoxu, *Lubrication Science* **1999**, *11*, 217-226.
[160] I. Lahouij, B. Vacher, J.-M. Martin, F. Dassenoy, *Wear* **2012**, *296*, 558-567.
[161] O. Tevet, P. Von-Huth, R. Popovitz-Biro, R. Rosentsveig, H. D. Wagner, R. Tenne, *Proceedings of the National Academy of Sciences of the USA* **2011**, *108*, 19901-19906.
[162] B. A. Kheireddin, W. Lu, I. C. Chen, M. Akbulut, *Wear* **2013**, *303*, 185-190.
[163] Y. Lv, L. Hao, W. Hu, Y. Ran, Y. Bai, L. Zhang, *Scientific Reports* **2016**, *6*.
[164] V. C. Shunmugasamy, S. E. Zeltmann, N. Gupta, O. M. Strbik, *The Journal of The Minerals, Metals & Materials Society* **2014**, *66*, 892-897.
[165] C. I. Zoldesi, I. L. Ivanovska, C. Quilliet, G. J. Wuite, A. Imhof, *Physical Review E* **2008**, *78*, 051401.
[166] B. Sarrazin, N. Tsapis, L. Mousnier, N. Taulier, W. Urbach, P. Guenoun, *Langmuir* **2016**, *32*, 4610-4618.
[167] A. R. Sulkanen, J. Sung, M. J. Robb, J. S. Moore, N. R. Sottos, G. Y. Liu, *Journal of the American Chemical Society* **2019**, *141*, 4080-4085.
[168] S. M. Jo, F. R. Wurm, K. Landfester, *Angewandte Chemie International Edition* **2021**, *60*, 7728-7734.
[169] S. Jiang, A. Kaltbeitzel, M. Hu, O. Suraeva, D. Crespy, K. Landfester, *ACS Nano* **2020**, *14*, 498-508.
[170] Q. Yin, S. Tu, M. Chen, L. Wu, *Langmuir* **2019**, *35*, 11524-11532.

[171] L. D. Landau, E. M. Lifshitz, A. M. Kosevich, L. P. Pitaevskii, *Theory Of Elasticity, Vol. 7*, **1986**.
[172] A. Fery, F. Dubreuil, H. Möhwald, *New Journal of Physics* **2004**, *6*, 18.
[173] A. Fery, R. Weinkamer, *Polymer* **2007**, *48*, 7221-7235.
[174] A. V. Progorelov, *Bending of Surfaces and Stability of Shells, Vol. 72*, American Mathematical Society, **1988**.
[175] C. I. Zoldesi, A. Imhof, *Advanced Materials* **2005**, *17*, 924-928.
[176] C. I. Zoldesi, C. A. van Walree, A. Imhof, *Langmuir* **2006**, *22*, 4343-4352.
[177] W. Yang, J. Yang, Y. Dong, S. Mao, Z. Gao, Z. Yue, S. J. Dillon, H. Xu, B. Xu, *Carbon* **2018**, *137*, 411-418.
[178] L. Zhang, M. Kappl, G. K. Auernhammer, D. Vollmer, *Langmuir* **2009**, *25*, 2711-2717.
[179] L. A. Taber, *Journal of Applied Mechanics* **1982**, *49*, 490-491.
[180] H. Hertz, *Journal für die reine und angewandte Mathematik* **1881**, *92*, 156-171.
[181] M. R. Gallas, A. R. Rosa, T. H. Costa, J. A. H. d. Jornada, *Journal of Materials Research* **1996**, *12*, 764-768.
[182] A. Jiang, D. Ke, L. Xu, Q. Xu, J. Li, J. Wei, C. Hu, S. Grasso, *Journal of Materiomics* **2019**, *5*, 496-501.
[183] Y. Shi, I. Minami, M. Grahn, M. Björling, R. Larsson, *Tribology International* **2014**, *69*, 39-45.
[184] W. Wang, B. Shen, Y. Li, Q. Ni, L. Zhou, F. Du, *Science Progress* **2021**, *104*, 3685.
[185] J. Padgurskas, R. Rukuiža, R. Kreivaitis, S. J. Asadauskas, D. Bražinskienė, *Tribology - Materials, Surfaces & Interfaces* **2009**, *3*, 97-102.
[186] I. Lahouij, E. W. Bucholz, B. Vacher, S. B. Sinnott, J. M. Martin, F. Dassenoy, *Nanotechnology* **2012**, *23*, 375701.
[187] N. Jagielski, S. Sharma, V. Hombach, V. Mailänder, V. Rasche, K. Landfester, *Macromolecular Chemistry and Physics* **2007**, *208*, 2229-2241.
[188] C. Herrmann, D. Crespy, K. Landfester, *Colloid and Polymer Science* **2011**, *289*, 1111-1117.
[189] P. C. Mishra, S. Mukherjee, S. K. Nayak, A. Panda, *International Nano Letters* **2014**, *4*, 109-120.
[190] J. Lim, J. Pyun, K. Char, *Angewandte Chemie International Edition* **2015**, *54*, 3249-3258.
[191] L. Crapanzano, W. A. Crichton, G. Monaco, R. Bellissent, M. Mezouar, *Nature Materials* **2005**, *4*, 550-552.
[192] Y.-X. Yin, S. Xin, Y.-G. Guo, L.-J. Wan, *Angewandte Chemie* **2013**, *125*, 13426-13441.
[193] Y. S. Su, A. Manthiram, *Nature Communications* **2012**, *3*, 1166.
[194] D. J. Parker, H. A. Jones, S. Petcher, L. Cervini, J. M. Griffin, R. Akhtar, T. Hasell, *Journal of Materials Chemistry A* **2017**, *5*, 11682-11692.
[195] M. K. Rybarczyk, H.-J. Peng, C. Tang, M. Lieder, Q. Zhang, M.-M. Titirici, *Green Chemistry* **2016**, *18*, 5169-5179.
[196] J.-g. Liu, M. Ueda, *Journal of Materials Chemistry* **2009**, *19*, 8907.
[197] J. J. Griebel, S. Namnabat, E. T. Kim, R. Himmelhuber, D. H. Moronta, W. J. Chung, A. G. Simmonds, K. J. Kim, J. van der Laan, N. A. Nguyen, E. L. Dereniak, M. E. Mackay, K. Char, R. S. Glass, R. A. Norwood, J. Pyun, *Advanced Materials* **2014**, *26*, 3014-3018.
[198] W. Feng, E. Borguet, R. D. Vidic, *Carbon* **2006**, *44*, 2998-3004.

[199] M. P. Crockett, A. M. Evans, M. J. Worthington, I. S. Albuquerque, A. D. Slattery, C. T. Gibson, J. A. Campbell, D. A. Lewis, G. J. Bernardes, J. M. Chalker, *Angewandte Chemie International Edition* **2016**, *55*, 1714-1718.
[200] K. J. Rao, S. Paria, *RSC Advances* **2013**, *3*, 10471.
[201] J. G. Wagenfeld, K. Al-Ali, S. Almheiri, A. F. Slavens, N. Calvet, *Waste Management* **2019**, *95*, 78-89.
[202] Y. Jin, C. Yu, R. J. Denman, W. Zhang, *Chemical Society Reviews* **2013**, *42*, 6634-6654.
[203] S. J. Rowan, S. J. Cantrill, G. R. L. Cousins, J. K. M. Sanders, J. Stoddart, F., *Angewandte Chemie International Edition* **2002**, *41*, 898-952.
[204] F. Klepel, B. J. Ravoo, *Organic & Biomolecular Chemistry* **2017**, *15*, 3840-3842.
[205] U. F. Fritze, M. von Delius, *Chemical Communications* **2016**, *52*, 6363-6366.
[206] A. V. Tobolsky, A. Eisenberg, *Journal of the American Chemical Society* **1959**, *4*, 780-782.
[207] A. V. Tobolsky, A. Eisenberg, *Journal of Colloid Science* **1962**, *17*, 717-725.
[208] A. V. Toboslky, A. Eisenberg, *Journal of Colloid Science* **1962**, *17*, 49-65.
[209] S. Penczek, R. Slazak, A. Duda, *Nature* **1978**, *273*, 738-739.
[210] L. B. Blight, B. R. Curell, B. J. Nash, T. Scott, C. Stillo, *The British Polymer Journal* **1980**, *12*, 5-11.
[211] Y. Zhang, N. G. Pavlopoulos, T. S. Kleine, M. Karayilan, R. S. Glass, K. Char, J. Pyun, *Journal of Polymer Science Part A: Polymer Chemistry* **2018**, *57*, 7-12.
[212] X. Wu, J. A. Smith, S. Petcher, B. Zhang, D. J. Parker, J. M. Griffin, T. Hasell, *Nature Communications* **2019**, *10*, 647.
[213] K. W. Park, E. M. Leitao, *Chemical Communications* **2021**, *57*, 3190-3202.
[214] J. Ma, J. Fan, S. Chen, X. Yang, K. N. Hui, H. Zhang, C. W. Bielawski, J. Geng, *ACS Applied Materials & Interfaces* **2019**, *11*, 13234-13243.
[215] F. Zhang, Y. Luo, X. Gao, R. Wang, *ACS Sustainable Chemistry & Engineering* **2020**, *8*, 12100-12109.
[216] C. Herrera, K. J. Ysinga, C. L. Jenkins, *ACS Applied Materials & Interfaces* **2019**, *11*, 35312-35318.
[217] K. Orme, A. H. Fistrovich, C. L. Jenkins, *Macromolecules* **2020**, *53*, 9353-9361.
[218] P. Yan, W. Zhao, B. Zhang, L. Jiang, S. Petcher, J. A. Smith, D. J. Parker, A. I. Cooper, J. Lei, T. Hasell, *Angewandte Chemie International Edition* **2020**, *59*, 13371-13378.
[219] P. W. Voorhees, *Journal of Statistical Physics* **1985**, *38*, 231-252.
[220] P. D. Bartlett, D. S. Trifan, *Journal of Polymer Science* **1956**, *XX*, 457-476.
[221] Y. T. Didenko, W. B. McNamara III, K. S. Suslick, *Journal of the American Chemical Society* **1999**, *121*, 5817-5818.
[222] S. C. Thickett, R. G. Gilbert, *Polymer* **2007**, *48*, 6965-6991.
[223] A. V. Tobolsky, W. MacKnight, R. B. Beevers, V. D. Gupta, *Polymer* **1963**, *4*, 423-427.
[224] S. Ichihara, A. Komatsu, T. Hata, *Polymer Journal* **1971**, *2*, 650-655.
[225] D. Gupta, A. R. Knight, *Canadian Journal of Chemistry* **1980**, *58*, 1350-1354.
[226] X. Huang, Z. Wang, R. Knibbe, B. Luo, S. A. Ahad, D. Sun, L. Wang, *Energy Technology* **2019**.
[227] L. Kong, H.-J. Peng, J.-Q. Huang, W. Zhu, G. Zhang, Z.-W. Zhang, P.-Y. Zhai, P. Sun, J. Xie, Q. Zhang, *Energy Storage Materials* **2017**, *8*, 153-160.
[228] C.-W. Ou, C.-H. Su, U.-S. Jeng, S.-h. Hsu, *ACS Applied Materials & Interfaces* **2014**, *6*, 5685-5694.

[229] A. Musyanovych, J. Schmitz-Wienke, V. Mailänder, P. Walther, K. Landfester, *Macromolecular Bioscience* **2008**, *8*, 127-139.